

© Copyright 2017

Je-Yuan Hsu

Estimates of Drag Coefficients and Surface Waves under Tropical Cyclones
using Subsurface EM-APEX floats

Je-Yuan Hsu

A dissertation submitted in partial fulfillment of the
requirements for the degree of

Doctor of Philosophy

University of Washington

2017

Reading Committee:

Ren-Chieh Lien, Chair

Eric A. D'Asaro, Co-Chair

Thomas B. Sanford

Program Authorized to Offer Degree:

School of Oceanography

University of Washington

Abstract

Estimates of Drag Coefficients and Surface Waves under Tropical Cyclones
using Subsurface EM-APEX floats

Je-Yuan Hsu

Chairs of the Supervisory Committee:

Senior Scientist Ren-Chieh Lien

Senior Scientist Eric A. D'Asaro

Applied Physics Laboratory

Nineteen autonomous EM-APEX floats were air-launched from aircraft to measure the profiles of ocean current velocity, temperature, salinity, and high-frequency velocity variance $\overline{\sigma_u^2}$ under five different tropical cyclones. In the first part of this work, the surface wind stress τ is estimated by integrating the float velocity measurements in the vertical, assuming a linear momentum budget balance. The biases and uncertainties of estimated τ are studied carefully, using the simulations of tropical cyclone-induced ocean response in the Price–Pinkel–Weller (PWP3D) model. The results are reliable only before passage of the storms' eyes. At wind speeds $|\mathbf{U}_{10}| = 25\text{--}40 \text{ m s}^{-1}$ the downwind drag coefficient C_{\parallel} is $1.1\text{--}3.1 \times 10^{-3}$ in the front-right sector of tropical cyclones and $0.8\text{--}1.7 \times 10^{-3}$ in the front-left sector. At wind speeds $|\mathbf{U}_{10}| > 40 \text{ m s}^{-1}$, the C_{\parallel} is $\sim 1.6 \times 10^{-3}$. The angle ϕ of drag τ is mostly clockwise from the wind \mathbf{U}_{10} in the front-right sector of storms. A new parameter, the nondimensional effective wind duration ζ^* , is proposed as a function of wind forcing, storm translation, and fetch length. The value of ζ^* is shown to predict the values of C_{\parallel} and ϕ . C_{\parallel} increases with decreasing ζ^* . We propose that surface waves with larger amplitude are forced more efficiently by the wind under faster storms,

resulting in stronger surface wave breaking and thus higher C_{\parallel} . In the second part of this work, the peak frequency f_p and significant wave height H_s of surface waves are estimated under Typhoon Fanapi using a nonlinear least-squared fit of the modeled profiles to the profiles of $\widetilde{\sigma_u}^2$ measured by the floats, assuming the Joint North Sea Wave Project (JONSWAP) surface wave spectrum. The f_p is 0.08–0.10 Hz, with the maximum f_p (0.10 Hz) in the rear-left quadrant of Fanapi. The H_s is 6–12 m with the maximum in the rear sector of Fanapi. The results are then assessed and compared to the simulations in the WAVEWATCH III surface wave model. The contributions of this work, including the improvements to previous methods for estimating τ and surface waves using subsurface EM-APEX floats, the estimates of drag coefficients and ϕ under five tropical cyclones, and the data-based parameterization of drag coefficients in terms of surface waves' effects, are all important to future studies of tropical cyclone–wave–ocean interactions.

TABLE OF CONTENTS

List of Figures	iii
List of Tables	viii
Chapter 1. Introduction	1
Chapter 2. Estimates of Drag Coefficients under Typhoon Megi 2010	6
2.1 Introduction of Drag Coefficients	6
2.2 ITOP Experiment and Measurements	11
2.3 Method of Estimating Surface Wind Stress and Drag Coefficients	14
2.4 Storm-induced Current Velocity under Typhoon Megi	16
2.5 Estimates of Apparent Drag Coefficients	18
2.6 PWP3D Model	19
2.7 Estimates of Adjusted Drag Coefficients	22
2.8 Discussion	24
2.9 Summary	25
Chapter 3. Scaling of Drag Coefficients under Five Tropical Cyclones	41
3.1 Introduction	41
3.2 Experiments	43
3.3 EM-APEX Float Measurements	44
3.4 Estimating Adjusted Drag Coefficients	45
3.5 Adjusted Drag Coefficients by Tropical Cyclone Sector	46
3.6 Scaling Drag Coefficients using Surface Waves	47

3.7	Discussion: Parameter ζ^*	50
3.8	Summary	52
Chapter 4. Estimates of Surface Waves Using Subsurface EM-APEX floats under Typhoon Fanapi 2010..... 63		
4.1	Introduction of Surface Wave Measurements.....	64
4.2	EM-APEX Float Measurements of Velocity Variance.....	66
4.3	Theory of Seawater Motion-induced Electric Current.....	67
4.4	Method to Estimate Surface Waves Using EM-APEX Float Measurements	69
4.5	Surface Waves under Typhoon Fanapi 2010	73
4.6	Surface Waves Simulations under Typhoon Fanapi in WAVEWATCH III (ww3).....	75
4.7	Simulations of Float Estimated Surface Waves using WAVEWATCH III (ww3)	79
4.8	Summary	84
Chapter 5. Conclusion..... 104		
Appendix A. Tropical Cyclone Wind Maps Processing..... 106		
Appendix B. Estimations of Wind-Driven Current Velocity on EM-APEX floats..... 118		
Appendix C. Surface Wave Velocity Variance Measured by EM-APEX Floats		
Appendix D. Surface Wave Velocity Variance Modeled by Wave Spectrum		
Appendix E. Correlation Between Parameter T and Surface Wave Estimates..... 145		
Bibliography		
148		

List of Figures

Figure Number

1.1. Revised concept of Maximum Potential Intensity (MPI) based on the original reported by Emanuel (1995).....	5
2.1. (a) The drag coefficient C_d as a function of wind speed at 10 m above the sea surface $ \mathbf{U}_{10} $ from our analysis (heavy red lines) and as proposed by previous investigators (other colors). (b) Angle between the surface wind and stress vectors from our analysis (heavy red) and from Drennan et al. (1999, Fig. 6), Zhang et al. (2009, Figs. 1 and 3) and Potter et al. (2015, Figs. 1 and 4).....	29
2.2. (a) Typhoon Megi's track (black curve with dots), deployment positions of EM-APEX floats (blue and magenta dots), and position of mooring SA1 (red dot), and (b) the wind map of wind speed at 10 m above the sea surface (color shading) at 20:30 UTC 16 October at the arrival time of Typhoon Megi at the float array, AVISO surface geostrophic current velocity (black arrows) on 17 October, EM-APEX float positions and trajectories (blue and magenta dots and curves), and mooring SA1 position (red dot)	31
2.3. Zonal velocity (left column a, d, g), meridional velocity (middle column b, e, h), and temperature (right column c, f, i) measured by three EM-APEX floats (rows).....	32
2.4. Apparent downwind drag coefficient $C_{ }$ (a), apparent crosswind drag coefficient C_{\perp} (b), and angle ϕ between surface wind stress vector and wind vector (c) for $ \mathbf{U}_{10} > 22 \text{ m s}^{-1}$. This intermediate product is further corrected to give the final results	33
2.5. PWP3D model simulations of zonal current velocity (left column a–c), meridional current velocity (middle column d–f), estimated surface wind stress via momentum budget and linear momentum budget (right column g–i) at the three floats' (em3763c, em4913a and em3766c) positions (rows).....	34
2.6. Correction to the apparent drag coefficients due to nonlinear and pressure gradient terms in the momentum budget. Left column, the results from the PWP3D model employing the apparent downwind drag coefficient obtained in this analysis: (a) the sum of the nonlinear	

and pressure gradient terms on the downwind (green curve) and crosswind (purple curve) directions, (b) the apparent downwind drag coefficient (black curve) and the drag coefficient derived assuming a linear momentum balance (green dots), (c) the zero crosswind drag coefficient used in the PWP3D model (horizontal black line) and the crosswind drag coefficient derived assuming a linear momentum balance..... 36

2.7. Comparisons of float observations (dots with vertical error bars \pm one standard deviation) and PWP3D model simulations of the depth-integrated (0–150m) storm-induced zonal linear momentum terms (a–c), and meridional linear momentum terms (d–f). Simulation B is performed using adjusted drag coefficients derived in the present analysis (red and blue curves in a–f). Simulation C is performed using the C_d reported by Holthuijsen et al. (2012) (green and purple curves in a–f) 38

2.8. Comparisons of float observations and model results of the depth-integrated (0–150 m) storm-induced linear momentum terms (circle: $\partial u/\partial t$, cross: $\partial v/\partial t$, square: $f \times u$ and triangle: $f \times v$) in Simulation B (red) and Simulation C (blue) before the passage of Typhoon Megi and at $|\mathbf{U}_{10}| > 25 \text{ m s}^{-1}$ 40

3.1. The tracks of hurricanes in the North Atlantic (a), Frances: green; Gustav: purple; Ike: gold. The tracks of typhoons in the western Pacific (b), Fanapi: blue; Megi: red. Tropical cyclone wind maps at the time eyes pass near EM-APEX float positions (c–g) and trajectories of float positions (blue dots connected with lines in c–g)..... 57

3.2. Estimates of adjusted downwind drag coefficient \tilde{C}_{\parallel} (a and d) and the angle ϕ (b and e) between the surface wind stress $\tilde{\boldsymbol{\tau}}$ and wind \mathbf{U}_{10} in five different tropical cyclones (colored lines as in Fig. 3.1), using the float measurements in the front-right (a and b) and front-left (d and e) sectors of tropical cyclones (c) 58

3.3. Fetch length χ at the float positions (color shading) relative to tropical cyclone eye positions computed using the parametric model of $\chi(r,\theta)$ of fetch-limited surface waves (black contour lines) in Hwang et al. (2016) 60

3.4. Dependence of adjusted downwind drag coefficient \tilde{C}_{\parallel} (a–c) and the angle ϕ between the surface wind stress $\tilde{\boldsymbol{\tau}}$ and wind \mathbf{U}_{10} (d–f) under five tropical cyclones (colored lines as in Fig. 3.1) at $|\mathbf{U}_{10}| = 25\text{--}40 \text{ m s}^{-1}$ (front-right sector: dots; front-left sector: triangles) on

nondimensional wind duration ζ_c assuming the constant fetch (a and d), ζ_χ assuming the parametric model $\chi(r,\theta)$ in Hwang et al. (2016) (b and e), and nondimensional effective wind duration ζ^* (c and f), respectively	61
3.5. An illustration of surface wave energy $S_\eta(f_r)$ at the motion-forced frequency f_r . The black line is the empirical JONSWAP spectrum with the peak frequency $f_p = 0.08$ Hz....	62
4.1. (a) Typhoon Fanapi's track in the western Pacific (black curve with dots), deployment positions of EM-APEX floats (blue and magenta dots), and (b) the map of wind speed at 10-m height above the sea surface (color shading) and EM-APEX float positions (blue and magenta dots) at 01:30 UTC 18 September 2010	89
4.2. Photo of EM-APEX floats (left), the top view of EM-APEX floats (middle), and an illustration of electric field around floats (right), $-\nabla\Phi_{EM}$ (blue arrows). The voltage measured by two orthogonal pairs of electrodes, E_1 and E_2	90
4.3. Vertical positions of four EM-APEX floats near Fanapi's track descending (blue dots in a–d) and ascending (red dots a–d), and the profiles of measured velocity variance $\overline{\sigma_u^2}$ taken by one pair of the electrodes E_1 on the floats ascending (dots in e–h) at the time relative to the arrival time of Typhoon Fanapi's eye at the float array (different colors in e–h).....	91
4.4. EM-APEX float estimates of peak frequency (a, c, e, and g) and significant wave height (b, d, f, and h) under Typhoon Fanapi assuming the JONSWAP spectrum (\tilde{f}_p and \tilde{H}_s , dots with error bars as one standard deviation) or assuming a single dominant surface wave (\check{f}_p and \check{H}_s , dots connected with lines) on electrodes E_1 (blue) and E_2 (red).....	93
4.5. WAVEWATCH III (ww3) model outputs of significant wave height (color shading in a), surface wave mean wavelength (color shading in b), and surface wave propagating direction (white arrows in b) at 01:30 UTC 18 September 2010 forced by the modeled Typhoon Fanapi winds $ U_{10} $ ($m s^{-1}$) (black contour lines and black arrows in a)	95
4.6. WAVEWATCH III model outputs (ww3) of frequency spectrum of ocean surface displacement S_η^{ww3} (solid lines in b–e) at four locations (a) under Typhoon Fanapi: Front-Left (represented by black A), Right (represented by purple B), and Rear (represented by green C), and within the eyewall (represented by blue D within the red circle)	96

4.7. Maps of EM-APEX float estimated peak frequency \tilde{f}_p (a) and significant wave height \tilde{H}_s (d) using results in Fig. 4.4, and the actual ww3 model outputs	97
4.8. Peak frequency \tilde{f}_p^{ww3} (a, c, e, and g) and significant wave height \tilde{H}_s^{ww3} (b, d, f, and h) estimated using the ww3 simulated $\widetilde{\sigma_{ww3}^2}$ (red dots) and the actual ww3 model outputs of f_p^{ww3} and H_s^{ww3} (black lines) at different float positions under Typhoon Fanapi	98
4.9. Maps of ww3 estimated peak frequency \tilde{f}_p^{ww3} (a) and significant wave height \tilde{H}_s^{ww3} (d) using results in Fig. 4.8, and the actual ww3 model outputs	99
4.10. Peak frequency \tilde{f}_p^{ww3} (a) and significant wave height \tilde{H}_s^{ww3} (b) estimated using the ww3 simulated $\widetilde{\sigma_{ww3}^2}$ at float em4907a, assuming the JONSWAP spectrum (blue dots) and the empirical spectrum in Donelan et al. (1985) (red dots), respectively	100
4.11. Peak frequency \tilde{f}_p^{ww3} (a, b, and c) and significant wave height \tilde{H}_s^{ww3} (d, e, and f) estimated using the ww3 simulated $\widetilde{\sigma_{ww3}^2}$ at float em4907a, assuming different values for the shape parameters	101
4.12. Ratio of the ww3 estimated \tilde{f}_p^{ww3} (a) and \tilde{H}_s^{ww3} (b) to the actual ww3 model outputs of f_p^{ww3} and H_s^{ww3} at float em4907a.....	102
4.13. Comparisons between the ratio of ww3 estimated \tilde{H}_s^{ww3} to actual ww3 model output of H_s^{ww3} and $\sqrt{1 + \beta^2}$. The \tilde{H}_s has already been corrected for the rotational demodulation effect α in Fig. 4.12b. The β_p and β_m are parameterized using the ww3 model outputs of surface wave direction at f_p (blue dots) and mean surface wave direction (red dots), respectively	103
A.1. Fit of radial model (black line) to all 10-m wind speed measurements from WC-130 (630W) and DOTSTAR flights centered on 00UTC 17 October 2010.....	113
A.2. Ratio of wind speed data (colored dots) to the radial model in Fig. A.1 as a function of radius from the eye and azimuth from north.....	114

A.3. Map of wind speed at 10-m height above the sea surface $ \mathbf{U}_{10} $ (m s^{-1}) for 17 October 2010 aircraft surveys (630W) shown by background color with contours	115
A.4. Wind speed at three EM-APEX floats. Black bars show the times of the three storm surveys interpolated to the locations of each float	116
A.5. The mean and standard deviation of storm-relative inflow angle averaged between 10 and 50 m above the sea surface α at the front-right quadrant of Typhoon Megi (blue dots and vertical lines) measured from dropsondes	117
B.1. Estimates of amplitudes (top row) and phases (bottom row) of K1 (left column) and M2 (right column) tidal zonal velocity at mooring SA1	125
B.2. Estimates of the vertical phase propagation and the error on the extrapolation of K1 and M2 amplitude from the deeper layer (layer C) on mooring SA1 to the upper layer using ADCP velocity from April to October 2010	126
B.3. Average of tidal zonal current velocity U (left column a–c), tidal meridional current velocity V (middle column d–f), and low-frequency zonal (blue lines in right column g–i) and meridional current (red lines in right column g–i) velocity in the stochastic simulation at three float positions (rows)	127
B.4. Average of estimated zonal current velocity u induced by tropical cyclone wind. Distances of floats from storm tracks, y , are labeled following the floats' identification	128
B.5. Average of estimated meridional current velocity v induced by tropical cyclone wind, as in Fig. B.4.....	129
C.1. An illustration of data processing on the voltage measurements $\Delta\Phi_1$ (black line with dots) taken by the pair of electrodes E_1 on the EM-APEX floats	141
E.1. Estimates of peak frequency f_p (a–c) at the positions of EM-APEX floats (color shading), and the ratio of motion-forced frequency f_r to f_p (d–f), under Gustav (a and d), Ike (b and e), and Fanapi (c and f)	146
E.2. Comparison between the T parameterized by the $\chi(r,\theta)$ in Hwang et al. (2016), and the ratio of motion-forced frequency f_r to estimated peak frequency f_p in the front-right (triangles) and front-left (circles) sectors of Gustav, Ike, and Fanapi.....	147

List of Tables

Table Number

1.1. Previous studies estimating surface wind stress τ and explanations of τ variability in laboratory and field experiments.....	4
2.1. EM-APEX float deployment locations in Megi at the time they began profiling during the ITOP experiment.....	27
2.2. The mean and standard errors of adjusted downwind and crosswind drag coefficients at different wind speed intervals during Typhoon Megi.....	28
3.1. The oceanic properties measured by twelve EM-APEX floats at $ \mathbf{U}_{10} > 25 \text{ m s}^{-1}$, and tropical cyclone properties as storm eyes passed float positions. The distance of floats' positions to the tracks Y (km) is positive to the right side. The mixed layer depth (MLD) is computed using the temperature and salinity profiles measured by the CTD mounted on the floats. The ocean current speed $ \mathbf{v} $ in the MLD (m s^{-1}) is averaged using the profiles of velocity measured by the floats	54
3.2. The mean and standard deviation of adjusted and apparent downwind drag coefficients, and the angle ϕ of drag $\tilde{\tau}$ clockwise from \mathbf{U}_{10} , in the front-right and front-left sectors of five tropical cyclones.	55
3.3. The mean and standard deviation of drag coefficient estimates at the distance of floats to tropical cyclones' eyes r , azimuth θ of float positions clockwise from the motion of tropical cyclones (see Fig. 3.2c), the fetch length $\chi(r,\theta)$ using the parametric model in Hwang et al. (2016), and the orientation of wind θ_w	56
4.1. Notations in Chapter 4.	88
B.1. The estimates of amplitude and phase of K1 and M2 tides from EM-APEX float and mooring SA1 (bold) observations.....	124

ACKNOWLEDGMENTS

My journey of more than six years in the School of Oceanography at the University of Washington (UW) has been long, and will be memorable throughout my life. I thank many people at the University of Washington and Applied Physics Laboratory (APL). All are smart, friendly, and willing to share their research advice and innovative ideas.

I first give special thanks to my two advisers, Dr. Ren-Chieh Lien and Dr. Eric D'Asaro. Their wisdom, intuition, support, and encouragement have been critical in guiding my own research interests. I also thank my adviser Dr. I-I Lin at National Taiwan University for her encouragement to pursue higher education aboard.

I also thank Dr. Tom Sanford, for allowing me and teaching me how to use his EM-APEX floats to make observations under tropical cyclones. I also thank my committee members Dr. Luc Rainville, Dr. Mark Warner, and Dr. Jim Thompson for their advice at every step to quantify the uncertainties of research results. These lessons learned will be my important assets in my future academic career.

I thank all the crew members and scientists on the CBLAST and ITOP experiments, and the funding support from Office of Naval Research (ONR). The data taken by EM-APEX floats under tropical cyclones has been critical to my research. I thank John Dunlap at APL-UW, who builds EM-APEX floats, for his careful explanations on data processing.

Finally, I thank my parents, my friends, and all the warm caring from the church, for all their support to obtain a Ph.D. degree.

DEDICATION

For the Lord and those who always accompany me.

Chapter 1. Introduction

Tropical cyclones with strong winds, heavy rain, and storm surges produce severe damage to coastal and inland regions annually. To improve the prediction of tropical cyclone intensity, and the associated storm surges and precipitation, extensive studies have been devoted to typhoon–ocean interactions. One such theory — the maximum potential intensity (MPI) of tropical cyclones (Emanuel 1986) — reasons that tropical cyclone intensification can be maintained by the heat supply from the ocean, even in the absence of unstable meteorological conditions. The MPI theory was revised (Emanuel 1995) to consider the transfer of momentum from storms to the ocean. The MPI of storms is proportional to the air–sea net heat flux (Lin et al. 2013), which provides energy for tropical cyclone intensification, and is inversely proportional to the surface wind stress τ , which extracts tropical cyclone momentum by forcing upper ocean motions, such as near-inertial currents (Fig. 1.1). Note that the shear instability of near-inertial currents then induces strong vertical turbulence mixing and cooling (Price et al. 1994); i.e., the prediction of MPI will be indirectly modified by the τ due to the change of upper ocean heat content.

The generation of τ over the aerodynamically rough ocean is associated with turbulent Reynolds stresses, pressure transport, and viscous transfers (Jones and Toba 2001), often parameterized by a drag coefficient C_d as $|\tau| = \rho_{\text{air}} C_d |\mathbf{U}_{10}|^2$, where ρ_{air} is the air density, and \mathbf{U}_{10} is the wind velocity at 10-m above the sea surface. Various factors to the C_d have been studied in laboratory and field experiments (Table 1.1). The strong dependence of C_d on the wind speed $|\mathbf{U}_{10}|$ has been reported in many previous studies. Unfortunately, field observations of C_d as the function of $|\mathbf{U}_{10}|$ at $|\mathbf{U}_{10}| > 25 \text{ m s}^{-1}$ under tropical cyclones are few and values are scattered by

more than a factor of 2 (section 2.1 and Fig. 2.1), presumably due to the complex storm-induced surface wave field (Chen et al. 2013; Reichl et al. 2014). This work explores the present challenges for drag coefficient studies in section 2.1.

Jarosz et al. (2007) and Sanford et al. (2011) estimate the surface wind stress using the velocity measurements taken by a moored ADCP and Electromagnetic Autonomous Profiling Explorer (EM-APEX) floats, respectively. This work follows the same approach to estimate surface wind stress and drag coefficients using float velocity measurements in Typhoon Megi 2010 (Chapter 2), assuming the linear momentum balance (Sanford et al. 2011). Uncertainties in drag coefficient estimates are analyzed using a PWP3D ocean response model (Price et al. 1994). Chapter 3 extends the analysis of drag coefficient estimates using more float measurements from Hurricane France 2004, Hurricane Gustav 2008, Hurricane Ike 2008, and Typhoon Fanapi 2010. The drag coefficients and angle between the $\boldsymbol{\tau}$ and \mathbf{U}_{10} are estimated in the front-right and front-left sectors of tropical cyclones. The variability of drag coefficients is studied and scaled using a non-dimensional effective wind duration ζ^* , associated with the time for propagating surface waves staying in the intense wind region of tropical cyclones.

Sanford et al. (2011) estimate the surface waves' peak frequency f_p and significant wave height H_s using high-frequency (> 0.02 Hz) velocity variance $\widetilde{\sigma}_u^2$ measured by EM-APEX floats, assuming a single dominant surface wave, i.e., a narrowband spectrum. The second part of this work revisits the theory of motional induction in the upper ocean, and derives the model solution of $\widetilde{\sigma}_u^2$ (Chapter 4). The f_p and H_s under Fanapi are estimated by a nonlinear least-squared fit to the $\widetilde{\sigma}_u^2$, assuming the empirical JONSWAP spectrum (Hasselmann et al. 1973), i.e., a broadband spectrum. Estimates of surface waves using two different assumptions of surface waves, narrowband vs. broadband, are compared. The float estimates are then assessed

and compared using the surface wave simulations in the WAVEWATCH III model (The WAVEWATCH III Development Group 2016). The estimates of drag coefficients and surface waves under tropical cyclones are summarized in Chapter 5.

Literature	Factors on Surface Stress	Wind Speed (m/s)
Smith et al. (1980)	$ \mathbf{U}_{10} $	6-22
Large and Pond (1981)	$ \mathbf{U}_{10} $	4-26
Byrne (1983)	c_p/u_*	5-21
Geernaert et al. (1986)	$ \mathbf{U}_{10} $ and c_p/u_*	5-22
Edson et al. (1991)	ψ	4-13
Smith et al. (1992)	c_p/u_*	8-20
Anderson (1993)	$ \mathbf{U}_{10} $	6-21
Donelan et al. (1993)	c_p/u_*	5-21
Geernaert et al. (1993)	θ_{swell}	3-12
Dobson et al. (1994)	$ \mathbf{U}_{10} $	6-18
Reider et al. (1994)	θ_{swell}	2-14
Yelland and Taylor (1996)	$ \mathbf{U}_{10} $	3-26
Donelan et al. (1997)	$ \mathbf{U}_{10} $ and θ_{swell}	4-14
Janssen (1997)	$ \mathbf{U}_{10} $	8-20
Johnson et al. (1998)	c_p/u_*	3-13
Grachev and Fairall (2001)	c_p/u_* and θ_{swell}	0.5-6
Taylor and Yelland (2001)	H_s and $\partial H_s/\partial x$	3-16
Oost et al. (2002)	$ \mathbf{U}_{10} $, c_p/u_* and $\partial H_s/\partial x$	2-12
Drennan et al. (2003)	$ \mathbf{U}_{10} $, H_s and c_p/u_*	5-19
Grachev et al. (2003)	$ \mathbf{U}_{10} $ and θ_{swell}	1-16
Powell et al. (2003)	$ \mathbf{U}_{10} $	27-50
Donelan et al. (2004)	$ \mathbf{U}_{10} $	3-53
Donelan et al. (2006)	c_p/u_*	7-12
Drennan and Shay (2006)	\mathbf{u}	5-13
García-Nava et al. (2009)	$ \mathbf{U}_{10} $ and θ_{swell}	2-20
Zhang et al. (2009)	\mathbf{u}	3-18
Sanford et al. (2011)	$ \mathbf{U}_{10} $	27-55
Holthuijsen et al. (2012)	$ \mathbf{U}_{10} $ and θ_{swell}	20-61
Grare et al. (2013)	$ \mathbf{U}_{10} $ and c_p/u_*	1-17
Potter et al. (2015)	θ_{swell}	12-26

Table. 1.1. Previous studies estimating surface wind stress τ and explanations of τ variability in laboratory and field experiments. The $|\mathbf{U}_{10}|$ is the wind speed at 10-m height above sea surface, c_p the phase speed at the maximum spectral level, u_* is the friction velocity, ψ the atmospheric stability, H_s the significant wave height, θ_{swell} the swell propagation direction, $\partial H_s/\partial x$ the steepness of dominant surface waves, and \mathbf{u} the ocean current velocity.

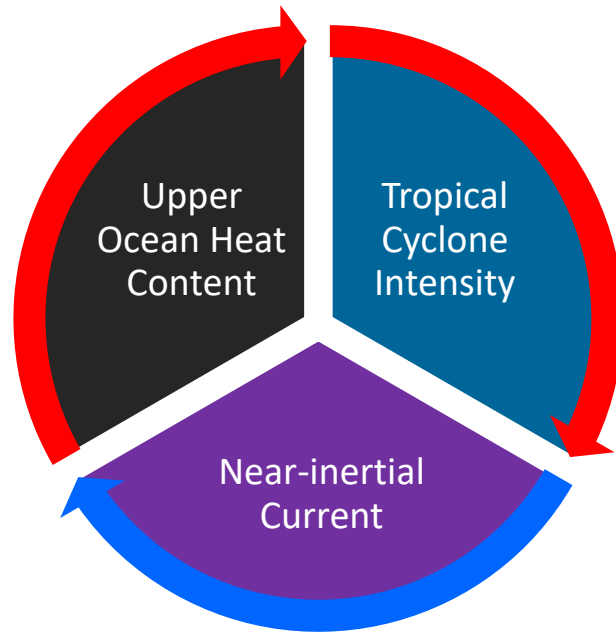


Fig. 1.1. Revised concept of Maximum Potential Intensity (MPI) based on the original reported by Emanuel (1995). The intensification of tropical cyclones is enhanced by the high upper ocean heat content (Lin et al. 2013) but is restricted by the momentum extraction from the storm to the ocean via surface wind stress. Red arrows represent enhancement. Blue arrow represents inhibition.

Chapter 2. Estimates of Drag Coefficients under Typhoon Megi 2010

Estimates of drag coefficients beneath Typhoon Megi (2010) are calculated from roughly hourly velocity profiles of three EM-APEX floats, air-launched ahead of the storm, and from air-deployed dropsondes measurements and microwave estimates of the 10-m wind field. The profiles are corrected to minimize contributions from tides and low-frequency motions and thus isolate the current induced by Typhoon Megi. Surface wind stress is computed from the linear momentum budget in the upper 150 m. Three-dimensional numerical simulations of the oceanic response to Typhoon Megi indicate that with small corrections, the linear momentum budget is accurate to 15% before the passage of the eye, but cannot be applied reliably thereafter. Monte Carlo error estimates indicate that stress estimates can be made for wind speeds greater than 25 m s^{-1} ; the error decreases with greater wind speeds. Downwind and crosswind drag coefficients are computed from the computed stress and the mapped wind data. Downwind drag coefficients increase to $3.5 \pm 0.7 \times 10^{-3}$ at 31 m s^{-1} , a value greater than most previous estimates, but decrease to $2.0 \pm 0.4 \times 10^{-3}$ for wind speeds $> 45 \text{ m s}^{-1}$, in agreement with previous estimates. The crosswind drag coefficient of $1.6 \pm 0.5 \times 10^{-3}$ at wind speeds $30\text{--}45 \text{ m s}^{-1}$ implies that the wind stress is about 20° clockwise from the 10-m wind vector and thus not directly downwind as is often assumed.

2.1 Introduction of Drag Coefficients

2.1.1 *Surface wind stress and drag coefficient*

Tropical cyclones with strong winds, heavy rain, and storm surges produce severe damage to coastal and inland regions annually. To improve the prediction of tropical cyclone

intensity, and the associated storm surges and precipitation, extensive studies have been devoted to typhoon–ocean interactions. The surface wind stress τ generated by tropical cyclone winds extracts energy and momentum from the storm, limiting its intensity, but also forces ocean currents (Emanuel 1995). It is often parameterized by a drag coefficient C_d , expressed as $|\tau| = \rho_{\text{air}} C_d |\mathbf{U}_{10}|^2$, where ρ_{air} is the air density, and \mathbf{U}_{10} is the wind velocity at 10 m above the sea surface. Previous studies suggest various empirical forms of C_d as a function of $|\mathbf{U}_{10}|$, atmospheric stability, surface roughness, surface wave height, and wave age (e.g., Charnock 1955; Dyer 1974; Johnson et al. 1998; Drennan et al. 2003). Better understanding the surface wind stress and its parameterization C_d is thus important for forecasting tropical cyclones and improving the prediction of the oceanic response to them.

2.1.2 Methods to estimate surface wind stress in tropical cyclones

Most previous studies have computed C_d under tropical cyclones from atmospheric measurements. The wind speed taken by the anemometers on buoys can be used to compute the momentum flux from tropical cyclones to the ocean (e.g., Potter et al. 2015). Powell et al. (2003) and Holthuijsen et al. (2012) estimate the surface roughness length and C_d using the profiles of tropical cyclone wind speed taken by GPS dropsondes, assuming the wind speed increases logarithmically with the height above the sea surface. Bell et al. (2012) study the C_d using the atmospheric angular momentum budget and measurements of tropical cyclone wind speed taken by a stepped-frequency microwave radiometer (SFMR) mounted on the aircraft.

Alternatively, C_d can be estimated from the momentum flux to ocean currents by measuring velocity under tropical cyclones. Jarosz et al. (2007) and Sanford et al. (2011) analyzed velocity measurements taken by a moored ADCP and three EM-APEX floats under

tropical cyclones, respectively. Using the depth-integrated linear momentum equation (hereinafter, the linear momentum budget method), they estimated the magnitude of surface wind stress and parameterized C_d as a function of wind speed. The present study uses a similar approach to compute C_d under Typhoon Megi. Note that the C_d estimated using the oceanic velocity measurements as a bottom-up approach may be inconsistent with that using the atmospheric wind speed measurements.

2.1.3 Previous drag coefficient estimation methods

The Tropical Ocean Global Atmosphere Coupled Ocean Atmosphere Response Experiment (TOGA COARE) has made observations of the air–sea flux from low to moderate wind speeds ($|\mathbf{U}_{10}| < 20 \text{ m s}^{-1}$) using ships and buoys since the 1990s (Edson et al. 2013). Employing the TOGA COARE bulk algorithm 3.5 (Edson et al. 2013), the drag coefficient depends more strongly on wind speed than atmospheric stability. It increases from 1×10^{-3} to 2.4×10^{-3} , $> 100\%$, as the wind speed $|\mathbf{U}_{10}|$ increases from 5 to 20 m s^{-1} , whereas the drag coefficient changes only about 5% when the atmospheric stability (z/L , where z is the height above the sea surface and L is the Monin–Obukhov length) varies from -1 to -0.2 . Large and Pond (1981) report that C_d is a constant for $|\mathbf{U}_{10}| = 4\text{--}11 \text{ m s}^{-1}$ and increases linearly with wind speed for $|\mathbf{U}_{10}| = 11\text{--}25 \text{ m s}^{-1}$ (Fig. 2.1a). The latest TOGA COARE bulk algorithm 3.5 also proposes that C_d increases linearly with wind speed for $|\mathbf{U}_{10}| = 6\text{--}25 \text{ m s}^{-1}$ (Edson et al. 2013), with a value slightly greater than that reported by Large and Pond (1981).

The parameterization of C_d in tropical cyclone wind conditions has been studied extensively using atmospheric and oceanic measurements, lab experiments, and model simulations (e.g., Powell et al. 2003; Donelan et al. 2004; Jarosz et al. 2007; Black et al. 2007;

Sanford et al. 2011; Holthuijsen et al. 2012; Chen et al. 2013). These studies generally support the linear increase of C_d with wind speed for $|\mathbf{U}_{10}| < 25 \text{ m s}^{-1}$. For stronger winds, $|\mathbf{U}_{10}| > 30 \text{ m s}^{-1}$, C_d is “saturated,” either remaining at a constant value or decreasing with wind speed (Fig. 2.1a). Bell et al. (2012) quantify C_d at wind speeds greater than 52 m s^{-1} in two hurricanes and report that C_d scattered for extremely high wind speeds $|\mathbf{U}_{10}| = 52\text{--}72 \text{ m s}^{-1}$, with a mean of 2.4×10^{-3} and a standard deviation of 1.1×10^{-3} .

Recent studies suggest that the parameterization of C_d by $|\mathbf{U}_{10}|$ varies in different sectors of the tropical cyclone. Holthuijsen et al. (2012) report that a maximum C_d ($\sim 4.6 \times 10^{-3}$) is located at the front-left quadrant of the tropical cyclone, and a minimum ($\sim 1.7 \times 10^{-3}$) is located on the right side for $|\mathbf{U}_{10}| = 30\text{--}40 \text{ m s}^{-1}$. Chen et al. (2013) used an atmosphere–wave–ocean coupled model to investigate C_d under Hurricane Frances. In contrast to results reported by Holthuijsen et al. (2012), they conclude that C_d is generally greater at the front-right quadrant of tropical cyclones than at the left side. They suggest that the variation in different quadrants is due to the spatial variability of surface waves forced by the rapid change of tropical cyclone wind.

Most previous studies assume that the crosswind stress is insignificant compared to the downwind stress (e.g., Large and Pond 1981). Recent field experiments investigating the effect of surface waves on surface wind stress report significant crosswind stress (Geernaert 1988; Drennan et al. 1999; Grachev et al. 2003; Zhang et al. 2009; Potter et al. 2015). Zhang et al. (2009) report that the direction difference between the surface wind and stress vectors varies from -40° to 60° for wind speeds $5\text{--}20 \text{ m s}^{-1}$ (Fig. 2.1b). Under tropical cyclones, extremely complex surface waves can be generated. The effect of surface waves on the crosswind stress has been studied using numerical models coupled with the surface wave field in tropical cyclones (Moon et al. 2004; Chen et al. 2013; Reichl et al. 2014). Chen et al. (2013) report that the

direction difference between the surface wind and the stress vectors is more than 20° within the eyewall of a tropical cyclone, again suggesting a significant crosswind stress.

Studies report a large variability in C_d at wind speeds greater than 25 m s^{-1} (Fig. 2.1a) and contradictory results for C_d distribution in different sectors of tropical cyclones (Holthuijsen et al. 2012; Chen et al. 2013). Numerical model studies show significant crosswind stress under tropical cyclones, but field observations are meager and vary greatly.

2.1.4 Drag coefficient study of Typhoon Megi 2010

In 2010, an international joint experiment, the Impact of Typhoons on the Ocean in the Pacific (ITOP), was conducted in the western Pacific to study the oceanic response to and recovery from tropical cyclones (D'Asaro et al. 2014). One of the primary scientific goals was to investigate surface wind stress under extreme wind conditions. During ITOP, seven EM-APEX floats were deployed to the right of Typhoon Megi's track, a category 5 typhoon in October 2010. Following Sanford et al. (2011), we estimate downwind and crosswind stress using velocity measurements taken by these floats via the linear momentum budget method.

Typhoon Megi and EM-APEX float measurements are described in section 2.2 and the linear momentum budget method is discussed in section 2.3. The downwind and crosswind drag coefficients are defined. The tidal and low-frequency current velocities may introduce uncertainties to wind stress estimates and are discussed in section 2.4. The apparent drag coefficients are estimated in section 2.5. The Price–Pinkel–Weller model (PWP3D) has been used to study the ocean momentum response to tropical cyclones (Price et al. 1994; Sanford et al. 2011). Here, the PWP3D is used to assess the assumed linear momentum budget to estimate surface wind stress (section 2.6). A correction to the derived wind stress estimates is made to

yield the adjusted wind stress (section 2.7), which is investigated using the PWP3D model. Our drag coefficient estimates and the direction difference between the surface wind and stress vectors are discussed and compared with previous studies (section 2.8).

2.2 ITOP Experiment and Measurements

ITOP targeted typhoons Fanapi and Megi using measurements taken from various atmospheric and oceanic platforms (D'Asaro et al. 2014). In this analysis, we focus on the drag coefficient estimated using measurements taken during Super Typhoon Megi only (Fig. 2.2a). Megi formed in the western Pacific on 12 October 2010 and intensified rapidly becoming a category 5 typhoon on 17 October (Wang and Wang 2014). Typhoon Megi moved primarily westward in the western Pacific, passed the northern Philippines on 18 October, turned northwestward into the South China Sea, and dissipated on 23 October after making landfall in China (D'Asaro et al. 2014; Wang and Wang 2014). This study focuses on measurements of Megi in the western Pacific only.

Between 12 and 18 October, 221 GPS dropsondes were deployed from C-130 aircraft to measure vertical profiles of wind speed and direction, and stepped-frequency microwave radiometers (SFMR) mounted on the bottom of the C-130 measured the microwave brightness temperature. The measurements of microwave brightness temperature were processed to estimate the wind speed at 10 m above the sea surface ($|U_{10}|$) as described in Uhlhorn and Black (2003). These were cross-calibrated and combined to construct a map of the surface winds (Fig. 2.2b) as described in Appendix A.1. During the measurement period, the radius of maximum wind speed was 15 km, smaller than the average size of tropical cyclones in the western Pacific (~40 km),

and the westward translation speed was $\sim 7.7 \text{ m s}^{-1}$, faster than typical tropical cyclones at the same latitude ($4\text{--}5 \text{ m s}^{-1}$).

Seven EM-APEX floats were deployed by a C-130 aircraft, at a horizontal separation of $\sim 25 \text{ km}$, along 128.3°E between 18.7° and 21°N on 16 October 2010, one day before the arrival of the eye of Typhoon Megi (Fig. 2.2a and Table 2.1). Floats were recovered by the R/V *Roger Revelle* on 19 October, 3 days after the deployment. Three EM-APEX floats measured the oceanic response to winds greater than 25 m s^{-1} . One float (em3763c) passed directly under the eye of Megi; the other two floats (em4913a and em3766c) passed at $\sim 42 \text{ km}$ and $\sim 73 \text{ km}$ north of Megi's eye on the right side of the storm track. Data obtained from these three floats are used to compute the surface wind stress in this study.

EM-APEX floats measure the electric and magnetic fields in the ocean (Sanford et al. 2005). The oceanic current velocity, relative to a conductivity-weighted average current \bar{V}^* , is estimated using the measured electric and magnetic fields based on the principle of motional induction (Sanford et al. 1978). Absolute current velocity can be obtained by estimating \bar{V}^* using the float's GPS positions. The uncertainty of EM velocity measurements taken during the ITOP experiment is $0.8\text{--}1.5 \text{ cm s}^{-1}$, estimated using the white spectral level of the observed velocity spectra. Temperature and salinity measurements were taken by a SeaBird Electronics SBE-41 CTD sensor mounted on the top end of the floats. The vertical resolution of velocity, temperature, and salinity was $3\text{--}4 \text{ m}$. GPS positions and data were transmitted by Iridium satellites when floats surfaced.

Before the arrival of Megi, floats profiled vertically from near the surface to 230-m depth at a profiling speed of $0.1\text{--}0.12 \text{ m s}^{-1}$. Between 10:00 UTC 16 October and 21:00 UTC 18 October when Megi passed the float array, EM-APEX floats profiled between 30 and 230-m

depth to prevent damage by storm-induced surface waves. In the following analysis, the current velocity in the upper 30 m is assumed uniform vertically and extrapolated to the surface using the shallowest velocity measurement below 30 m depth. The floats' positions during this period are estimated using the time integration of current velocity measured by the floats.

Strong near-inertial waves were generated on the right side of Megi due to the inertial resonance of the wind pattern. At 42 km to the right of the storm track (em4913a) (Fig. 2.2a), the near-inertial current was greater than 1 m s^{-1} (Fig. 2.3d and e). The surface mixed layer, defined as the shallowest depth where the density gradient is greater than 0.03 kg m^{-4} and the density is greater than the surface values by more than 0.3 kg m^{-3} , deepened by more than 20 m, from ~40 to 70 m depth, within one-half day after Megi's eye arrived at the float array, ~20:30 UTC 16 October. The base of the surface mixed layer oscillated by ~10 m near the inertial period due to the convergence and divergence of near-inertial waves, in agreement with observations reported by Gill (1984). The surface mixed layer cooled from 29.3 to 28.2°C in one day, presumably due to vertical mixing (Sanford et al. 2011).

The background oceanic current measured by the floats from the north to Megi's track varied from 0.4 m s^{-1} (em3766c) to 0.1 m s^{-1} (em3763c) at 12 h before Megi's arrival (Fig. 2.3), consistent with the surface geostrophic current estimated from AVISO (Fig. 2.2b). Tidal currents were also present, though at velocities less than inertial waves, especially in the surface mixed layer. Detailed analysis of the tides is given in Appendix B.1.

Several moorings were deployed during ITOP on the prevailing path of tropical cyclones (D'Asaro et al. 2014). One of the moorings, SA1, was located about 200 km north of Typhoon Megi's track. The mooring was equipped with a 75-kHz upward-looking ADCP to measure

current velocity between 50 and 550 m depth. In the following analysis, mooring velocity measurements will be used to quantify the tidal current during the observational period.

2.3 Method of Estimating Surface Wind Stress and Drag Coefficients

2.3.1 Linear momentum budget method

Following Sanford et al. (2011), we estimate surface wind stress using the depth-integrated linear momentum balance and the observed current velocity profiles taken by the EM-APEX floats. The momentum equation for a Boussinesq fluid is

$$\frac{\partial \mathbf{u}}{\partial t} + \mathbf{u} \cdot \nabla \mathbf{u} + f \hat{\mathbf{k}} \times \mathbf{u} = -\frac{1}{\rho_0} \nabla p + \frac{1}{\rho_0} \frac{\partial \boldsymbol{\tau}}{\partial z} - \frac{\rho}{\rho_0} g \hat{\mathbf{k}}, \quad (2.1)$$

where $\mathbf{u} = u\hat{\mathbf{i}} + v\hat{\mathbf{j}} + w\hat{\mathbf{k}}$ is the ocean current velocity vector, $\hat{\mathbf{i}}$, $\hat{\mathbf{j}}$, and $\hat{\mathbf{k}}$ are the unit vectors in east, north, and upward vertical directions, respectively, $\nabla = \frac{\partial}{\partial x} \hat{\mathbf{i}} + \frac{\partial}{\partial y} \hat{\mathbf{j}} + \frac{\partial}{\partial z} \hat{\mathbf{k}}$ the gradient operator, g the gravity, f the local Coriolis frequency of $\sim 5 \times 10^{-5} \text{ rad s}^{-1}$ at 20°N , p the pressure, ρ_0 the Boussinesq density, ρ the in-situ density, and $\boldsymbol{\tau}$ the stress vector.

Defining the horizontal current velocity and gradient operator as $\mathbf{v} = u\hat{\mathbf{i}} + v\hat{\mathbf{j}}$ and $\nabla_h = \frac{\partial}{\partial x} \hat{\mathbf{i}} + \frac{\partial}{\partial y} \hat{\mathbf{j}}$, respectively, the depth-integrated momentum equation from the sea surface to a depth $-H$ becomes

$$\int_{-H}^0 \left(\frac{\partial \mathbf{v}_h}{\partial t} + \mathbf{v} \nabla_h \cdot \mathbf{v} + \mathbf{v} \cdot \nabla_h \mathbf{v} + f \hat{\mathbf{k}} \times \mathbf{v} + \frac{1}{\rho_0} \nabla_h p \right) dz = \frac{(\boldsymbol{\tau}_0 - \boldsymbol{\tau}_{-H})}{\rho_0} + w_{-H} \mathbf{v}_{-H}, \quad (2.2)$$

where $\boldsymbol{\tau}_0$ is the surface wind stress, and $\boldsymbol{\tau}_{-H}$ and \mathbf{v}_{-H} the turbulent stress and horizontal velocity at $z = -H$, respectively. We assume that the vertical velocity vanishes at the sea surface. Following Sanford et al. (2011), we choose $H = 150 \text{ m}$ and assume that $\boldsymbol{\tau}_{-H}$ and $w_{-H} \mathbf{v}_{-H}$ are zero. These

assumptions are justified by results from PWP3D model simulations (section 2.4). The depth-integrated momentum equation is therefore simplified as

$$\int_{-H}^0 \left(\frac{\partial \mathbf{v}}{\partial t} + \hat{\mathbf{k}} \times \mathbf{v} + \mathbf{v} \nabla_h \cdot \mathbf{v} + \mathbf{v} \cdot \nabla_h \mathbf{v} + \frac{1}{\rho_0} \nabla_h p \right) dz = \frac{\boldsymbol{\tau}}{\rho_0} \quad (2.3)$$

Here, we have dropped the subscript for the surface wind stress $\boldsymbol{\tau}$, for convenience.

Sanford et al. (2011) estimate the surface wind stress $\tilde{\boldsymbol{\tau}}$ assuming the balance between the first two terms in Eq. (2.3) with the wind stress, i.e.,

$$\tilde{\boldsymbol{\tau}} = \boldsymbol{\tau} + \Delta\boldsymbol{\tau} = \rho_0 \int_{-H}^0 \left(\frac{\partial \mathbf{v}}{\partial t} + \hat{\mathbf{k}} \times \mathbf{v} \right) dz, \quad (2.4)$$

where $\Delta\boldsymbol{\tau}$ is the uncertainty of $\tilde{\boldsymbol{\tau}}$. The $\Delta\boldsymbol{\tau}$ represents the error in estimates of surface wind stress because of either the neglect of nonlinear terms and pressure gradient, i.e., the 3rd–5th terms on the left side of Eq. (2.3), or the existence of non-wind driven ocean current measured by the floats. The latter is discussed in section 2.4. To distinguish the estimates of surface wind stress using the linear momentum budget from the true wind stress $\boldsymbol{\tau}$, the $\tilde{\boldsymbol{\tau}}$ in Eq. (2.4) is termed apparent surface wind stress. Sanford et al. (2011) assume a linear momentum balance with negligible pressure gradient and nonlinear terms, i.e., $\Delta\boldsymbol{\tau} = 0$, so $\tilde{\boldsymbol{\tau}} = \boldsymbol{\tau}$. PWP3D numerical modeling is used to investigate the validity of this assumption (section 2.6). The differencing terms in the momentum budget (Eqs. 2.3 and 2.4) are computed in the second-order scheme in this study.

2.3.2 Downwind and crosswind drag coefficients

Recent studies (e.g., Reichl et al. 2014; Chen et al. 2013) report that the surface wind stress may have a significant crosswind component. In this analysis, the vector $\boldsymbol{\tau}$ on the ocean

surface can be projected to the respective directions along and perpendicular to the wind vector at 10-m height above the sea surface \mathbf{U}_{10} as

$$\boldsymbol{\tau} = \tau_{\parallel} \widehat{\mathbf{U}}_{10\parallel} + \tau_{\perp} \widehat{\mathbf{U}}_{10\perp} \quad (2.5)$$

where $\widehat{\mathbf{U}}_{10\parallel}$ and $\widehat{\mathbf{U}}_{10\perp}$ are unit vectors along and perpendicular to the \mathbf{U}_{10} , and τ_{\parallel} and τ_{\perp} are the projected stress at the downwind and crosswind directions, respectively. The angle ϕ between \mathbf{U}_{10} and the surface wind stress $\boldsymbol{\tau}$ is defined as

$$\phi = \tan^{-1} \frac{\tau_{\perp}}{\tau_{\parallel}} \quad (2.6)$$

$\tau_{\perp} > 0$ and $\phi > 0$ when the orientation of $\boldsymbol{\tau}$ is clockwise from the \mathbf{U}_{10} . Following previous studies (Smith 1980; Powell et al. 2003; Donelan et al. 2004), we parameterize τ_{\parallel} and τ_{\perp} by wind speed and define the downwind and crosswind drag coefficients as

$$C_{\parallel} = \frac{\tau_{\parallel}}{\rho_{\text{air}} |\mathbf{U}_{10}|^2}; C_{\perp} = \frac{\tau_{\perp}}{\rho_{\text{air}} |\mathbf{U}_{10}|^2}; C_d = \sqrt{C_{\parallel}^2 + C_{\perp}^2} \quad (2.7)$$

Here C_d is the magnitude of the drag coefficient. The estimates of downwind and crosswind drag coefficients computed using the linear momentum budget expressed in Eq. (2.4) are termed apparent downwind and crosswind drag coefficients in this study.

2.4 Storm-induced Current Velocity under Typhoon Megi

EM-APEX float velocity measurements \mathbf{v} taken before the arrival of Typhoon Megi's eye are used to estimate the surface wind stress and drag coefficient using the depth-integrated linear momentum budget (Eq. 2.4). The primary constituents of current velocity can be assumed as

$$\mathbf{v} = \mathbf{v}_{\text{wnd}} + \mathbf{v}_{\text{tide}} + \mathbf{v}_{\text{low}} + \delta$$

where \mathbf{v}_{wnd} is the velocity of wind-driven current, \mathbf{v}_{tide} the velocity of tides, \mathbf{v}_{low} the velocity of low-frequency currents, constant in amplitude and direction for at least a half day, such as the surface geostrophic current, and δ the instrumental noise in the velocity measurements.

Only the wind-driven ocean current velocity \mathbf{v}_{wnd} should be used to estimate surface wind stress in Eq. (2.4). The background currents, such as tides \mathbf{v}_{tide} and low-frequency currents \mathbf{v}_{low} , which are not directly forced by Megi, will cause the linear momentum budget to be unbalanced. For example, the depth-integrated linear momentum of a diurnal barotropic tide K1 with amplitude 0.1 m s^{-1} from the ocean surface to 150-m depth is $\sim 0.7 \text{ N m}^{-2}$, leading to an error of $\sim 20\%$ in surface wind stress estimates if $C_d = 4 \times 10^{-3}$ at $|\mathbf{U}_{10}| = 30 \text{ m s}^{-1}$. The magnitude of low-frequency currents can also influence the Coriolis rotation term in the linear momentum budget. The integrated momentum of randomly distributed δ in the linear momentum budget was investigated, but is negligible compared to the contributions of \mathbf{v}_{wnd} , \mathbf{v}_{tide} , and \mathbf{v}_{low} .

To estimate the apparent surface wind stress $\tilde{\boldsymbol{\tau}}$ using the wind-driven current velocity \mathbf{v}_{wnd} , the tides \mathbf{v}_{tide} and low-frequency currents \mathbf{v}_{low} are both estimated and removed from EM-APEX velocity measurements. The amplitude and phase of tides at the float locations are estimated by harmonic fitting of the velocity measurements between 200 and 220-m depth (Appendix B.1.2), and then used to extrapolate tides to the ocean surface by assuming the 1st mode baroclinic tide. The uncertainty of estimating \mathbf{v}_{tide} is primarily due to vertical phase propagation and amplitude difference in tidal extrapolation, implemented by the analysis of tides on the mooring SA1 (Appendix B.1.1). The low-frequency current is estimated by averaging the profiles of $(\mathbf{v} - \mathbf{v}_{\text{tide}})$ at different selected periods assuming the \mathbf{v}_{wnd} had not been forced by Megi (Appendix B.1.3). The uncertainty of estimating \mathbf{v}_{low} is affected by the estimates of \mathbf{v}_{tide} and the selected averaging period.

Simulations of 40,000 normally distributed ($\mathbf{v}_{\text{tide}} + \mathbf{v}_{\text{low}}$) are generated in the stochastic simulation (Appendix B.3), and removed from each of the observed EM-APEX float velocity profiles so as to generate 40,000 realizations of apparent wind-forced velocity profiles \mathbf{v}_{wnd} .

2.5 Estimates of Apparent Drag Coefficients

The $|\mathbf{U}_{10}|$ for the computation of drag coefficients is simulated in the normal distribution using the measured wind speed and root-mean-squared error (RMS); RMS is $\sim 4 \text{ m s}^{-1}$ outside Megi's eyewall, and $\sim 5 \text{ m s}^{-1}$ within the eyewall (Appendix A.1). Using the \mathbf{v}_{wnd} in the linear momentum budget (Eq. 2.4), 40,000 estimates of surface wind stress are computed and parameterized as apparent drag coefficients. The mean and standard deviation of apparent drag coefficients C_{\parallel} and C_{\perp} are computed for each EM-APEX float velocity profile (Fig. 2.4a and b).

Estimates of apparent drag coefficient are presented as the function of wind speed at 10 m above the sea surface $|\mathbf{U}_{10}|$ (small dots and thin vertical lines in Fig. 2.4). The standard deviations of estimates of apparent drag coefficients C_{\parallel} and C_{\perp} (vertical lines) are generally greater than 1.5×10^{-3} for $|\mathbf{U}_{10}| = 25\text{--}30 \text{ m s}^{-1}$. The large uncertainty in estimates of drag coefficient for $|\mathbf{U}_{10}| < 25 \text{ m s}^{-1}$ is due primarily to contamination by the tides and mean currents on estimates of wind-driven currents. We discuss drag coefficients for $|\mathbf{U}_{10}| > 25 \text{ m s}^{-1}$ exclusively in the following.

To summarize the effect of wind speed on apparent drag coefficients, we further average drag coefficients in different bins of wind speed ($\pm 2 \text{ m s}^{-1}$ at $|\mathbf{U}_{10}| = 27 \text{ m s}^{-1}$, $\pm 3 \text{ m s}^{-1}$ at $|\mathbf{U}_{10}| = 31 \text{ m s}^{-1}$, $\pm 3 \text{ m s}^{-1}$ at $|\mathbf{U}_{10}| = 37 \text{ m s}^{-1}$, and $\pm 9 \text{ m s}^{-1}$ at $|\mathbf{U}_{10}| = 56 \text{ m s}^{-1}$). We use the mean and standard deviation of apparent drag coefficients from each profile of EM-APEX floats to generate 1000 simulations assuming a normal distribution. Within each bin of wind speed, the

apparent drag coefficient averages are computed using the generated simulations from at least three different profiles, and then the mean and the standard deviation of the apparent drag coefficient averages are computed. The estimates of C_{\parallel} are more than 3×10^{-3} for $|\mathbf{U}_{10}| = 30\text{--}40$ m s^{-1} . The C_{\perp} and the angle ϕ between wind and stress are significantly different from zero, indicating the crosswind component of surface wind stress is not negligible.

2.6 PWP3D Model

The apparent drag coefficient under Typhoon Megi is estimated assuming a balance of the linear momentum budget. Simulations of oceanic response under Typhoon Megi in the PWP3D model are used to validate the assumption of linear momentum balance here, and to correct the apparent drag coefficient due to the neglect of nonlinear and pressure gradient terms (section 2.7).

2.6.1 *Model description*

Price et al. (1994) developed the PWP3D numerical model using momentum, continuity, temperature, and salinity equations, to study oceanic responses to moving tropical cyclones. The initial temperature and salinity fields are assumed horizontally homogeneous. In the following model simulations, horizontally and temporally averaged vertical profiles of EM-APEX float measurements of temperature and salinity taken within 18–19 h before the arrival of Megi’s eye are used as the initial conditions. The horizontal spatial resolution is 3 km, and the temporal resolution is 180 s. The spatial domain of the ocean is ± 375 km in the zonal direction, and ± 300

km in the meridional direction. The vertical resolution is 5 m, from the ocean surface to 300-m depth.

In the model, vertical turbulent mixing is parameterized using the bulk Richardson

number $Ri_b = -\frac{g\Delta\rho h}{\rho_0(\Delta v)^2}$ and the gradient Richardson number $Ri_g = \frac{-g\frac{\partial\rho}{\partial z}}{\rho_0\left(\frac{\partial v}{\partial z}\right)^2}$, where Δv and $\Delta\rho$ are

the difference of velocity and density, respectively, across the base of the surface mixed layer h (Price et al. 1986). In the PWP3D model, the turbulent mixing is enforced when $Ri_g < 0.25$, or $Ri_b < 0.65$, and the momentum and mass are mixed until Ri_g and Ri_b are beyond their stability criteria. For the model simulation, the spatial differencing terms are computed in the second-order scheme, and the leapfrog-trapezoidal method is used for the temporal integration (Price et al. 1994). Solar radiation is assumed as a sinusoidal function with a peak of 500 W m^{-2} at noon and zero at midnight. Longwave radiation is computed using the Boltzmann constant and sea surface temperature assuming the black body (Price et al. 1986). Constant values of dry (26°C) and wet (25°C) bulb air temperature in tropical cyclones are assumed (Sanford et al. 2011). The sensible and latent heat flux are computed using the wind speed and sea surface temperature in the model.

For Typhoon Megi's wind forcing in the model, the storm's wind speed and direction are interpolated linearly in time, moving in the real translation track, and passing the grid point at the center of the spatial domain at 20:30 UTC 18 October. The wind speed at the floats' positions in the model simulations is the same as the observations (Fig. 2.7g, h, and i). The surface wind stress for $|\mathbf{U}_{10}| < 25 \text{ m s}^{-1}$ in all simulations presented in this study is computed using the drag coefficient parameterization proposed by Large and Pond (1981) and mapped $|\mathbf{U}_{10}|$, assuming no crosswind stress.

2.6.2 *Model simulations and momentum budget*

In the first model simulation presented in this study (hereafter referred to as Simulation A), the surface wind stress τ in the model for $|\mathbf{U}_{10}| > 25 \text{ m s}^{-1}$ is computed using the mapped $|\mathbf{U}_{10}|$ advected over the ocean and our estimates of apparent downwind drag coefficient, but assuming no crosswind stress. Results of PWP3D model simulations of oceanic currents at three float positions as Megi approached the float array show the surface wind stress increasing and strong currents generated in the surface mixed layer (Fig. 2.5). At the arrival time of Megi, the simulated currents of $\sim 1.5 \text{ m s}^{-1}$ are similar to those observed by floats (Fig. 2.3), and the modeled mixed layer deepening, $\sim 30 \text{ m}$, is consistent with the observed deepening at the float on the track of Megi (em3763c).

The estimates of surface wind stress computed from Eqs. (2.3) and (2.4) are compared with the input surface wind stress (Fig. 2.5). The estimates of surface wind stress from Eq. (2.3) agree very well with the input surface wind stress, indicating that the momentum equation is implemented correctly and supporting the choice to neglect turbulent fluxes at 150-m depth in the model. Furthermore, the estimates of surface wind stress from Eq. (2.4) (the depth-integrated linear momentum budget) agree with the input surface wind stress with an uncertainty of $< 10\%$ only before the arrival of the storm's eye. The agreement within Megi's eyewall and after the passage of Megi's eye is poor, because the pressure gradient and nonlinear advection terms induced by Typhoon Megi are important, as suggested by Sanford et al. (2011). Based on PWP3D model results, drag coefficient estimates using Eq. (2.4) are reliable only before the arrival of Typhoon Megi, and some corrections near the eyewall of Megi are required. Note that variations in air temperature or solar radiation have little effect on the momentum budget balance. The estimate of surface wind stress using the linear momentum equation varies less than

1%, even with a change of $\pm 3^\circ\text{C}$ in air temperature or an insolation peak increase from 500 to 1000 W m^{-2} .

Because the nonlinear and pressure gradient terms at two floats near Megi's track (em4913a and em3763c) led to an uncertainty of $< 15\%$ before the passage of Megi's eye, another PWP3D model run at the float positions of em3763c (9 km from Megi's eye) was performed to investigate the corrections to the assumed linear momentum balance (section 2.7).

2.7 Estimates of Adjusted Drag Coefficients

In Simulation A (section 2.6), the downwind component of surface wind stress is computed using the mapped $|\mathbf{U}_{10}|$ and apparent downwind drag coefficient for $|\mathbf{U}_{10}| > 25 \text{ m s}^{-1}$, but assuming no crosswind stress. The nonlinear and pressure gradient terms, which are excluded from the estimates of apparent drag coefficients in the linear momentum budget Eq. (2.4), $\mathbf{v}\nabla_{\text{h}} \cdot \mathbf{v}$, $\mathbf{v} \cdot \nabla_{\text{h}} \mathbf{v}$ and $\frac{1}{\rho_0} \nabla_{\text{h}} p$, are significant near Megi's track even before the arrival of the storm (Fig. 2.6 a–c). Neglecting nonlinear and pressure gradient terms causes C_{\parallel} to be overestimated by $< 0.4 \times 10^{-3}$ ($\sim 10\%$ at the peak) and C_{\perp} to be overestimated by 0.5×10^{-3} at wind speeds greater than 25 m s^{-1} . We subtract the effects of nonlinear and pressure gradient terms on drag coefficients (the difference between green dots and black curve in Fig. 2.6b and between purple dots and black line in Fig. 2.6c) from our estimates of apparent downwind and crosswind drag coefficients (section 2.5) and call these the adjusted downwind \tilde{C}_{\parallel} and crosswind drag coefficients \tilde{C}_{\perp} .

Another simulation (B) computes the surface wind stress using the mapped $|\mathbf{U}_{10}|$ and adjusted downwind and crosswind drag coefficients for $|\mathbf{U}_{10}| > 25 \text{ m s}^{-1}$ (black curves in Fig.

2.6e and f). Drag coefficients computed using Eq. (2.4) (green dots and purple dots in Fig. 2.6e and f) agree well with the apparent drag coefficients discussed in section 2.5 (red dots with vertical bars in Fig. 2.6e and f), suggesting that the adjusted drag coefficients (black curves in Fig. 2.6e and f) are the better estimates of the true drag coefficients.

Table 2.2 summarizes the estimated adjusted downwind $\widetilde{C}_{\parallel}$ and crosswind drag coefficients \widetilde{C}_{\perp} in Typhoon Megi. The $\widetilde{C}_{\parallel}$ is about 3.2×10^{-3} at $|\mathbf{U}_{10}| = 27 \text{ m s}^{-1}$, reaches its peak of 3.5×10^{-3} at $|\mathbf{U}_{10}| = 31 \text{ m s}^{-1}$, and decreases to 2.0×10^{-3} for $|\mathbf{U}_{10}| > 55 \text{ m s}^{-1}$. The saturation of $\widetilde{C}_{\parallel}$ in extreme wind conditions is significant, decreasing about 50%. The \widetilde{C}_{\perp} is about zero for $|\mathbf{U}_{10}| < 27 \text{ m s}^{-1}$, reaches its peak of 1.6×10^{-3} at $|\mathbf{U}_{10}| = 37 \text{ m s}^{-1}$, and decreases to 0.7×10^{-3} for $|\mathbf{U}_{10}| > 45 \text{ m s}^{-1}$. The \widetilde{C}_{\perp} also decreases more than 50% for $|\mathbf{U}_{10}| > 37 \text{ m s}^{-1}$, but the orientation offset between stress and \mathbf{U}_{10} changes only slightly, from 30° to 20° for $|\mathbf{U}_{10}| = 37\text{--}56 \text{ m s}^{-1}$.

To further validate our estimates of $\widetilde{C}_{\parallel}$ and \widetilde{C}_{\perp} (Fig. 2.1 and Table 2.2) at the front-right quadrant of Typhoon Megi, we compute the depth-integrated time rate change of horizontal momentum and the Coriolis force (Fig. 2.7), i.e., $\int \frac{\partial \mathbf{v}}{\partial t} dz$ and $\int (\mathbf{f} \times \mathbf{v}) dz$, using float observations, and then compare our results with those from simulations B and C (Fig. 2.7). The downwind component of surface wind stress in Simulation C is computed using the mapped $|\mathbf{U}_{10}|$ and the C_d reported by Holthuijsen et al. (2012) for $|\mathbf{U}_{10}| > 25 \text{ m s}^{-1}$, but assuming no crosswind stress. The correlation coefficient of depth-integrated linear momentum components between Simulation B results and float observations for $|\mathbf{U}_{10}| > 25 \text{ m s}^{-1}$ is 0.83. This is slightly better than that between Simulation C results and observations, 0.68 (Fig. 2.8). That is, simulation results using our adjusted drag coefficients agree with observations better than those using the C_d reported by Holthuijsen et al. (2012). The discrepancy between simulated ocean momentum

response in Simulation B at 42 km to the right of Megi's track and observations (Fig. 2.7e) suggests that the drag coefficient may be affected by factors other than the wind speed.

2.8 Discussion

Many prior studies use wind speed profiles observed in the atmospheric boundary layer to investigate the neutral drag coefficient under tropical cyclones (Powell et al. 2003; Holthuijsen et al. 2012). In this study we instead use oceanic momentum response to study tropical cyclone surface wind stress (Jarosz et al. 2007; Sanford et al. 2011). The estimates of surface wind stress are parameterized by wind speed as drag coefficients.

For $|\mathbf{U}_{10}| < 30 \text{ m s}^{-1}$, the adjusted downwind drag coefficient \tilde{C}_{\parallel} increases with wind speed, in agreement with previous studies (Fig. 2.1a). For $|\mathbf{U}_{10}| = 30\text{--}40 \text{ m s}^{-1}$, the magnitude of $\tilde{C}_{\parallel} > 3.0 \times 10^{-3}$ agrees with that reported in an atmosphere–wave–ocean coupled model at the front-right quadrant of tropical cyclones (Chen et al. 2013), but is much greater than the neutral drag coefficient reported by others (Powell et al. 2003; Donelan et al. 2004). The unstable planetary boundary layer and complex surface wave field under Typhoon Megi may have caused the high drag coefficient (Dyer 1974; Chen et al. 2013). For $|\mathbf{U}_{10}| > 40 \text{ m s}^{-1}$, the drag coefficient decreases with wind speed, in agreement with other studies (Powell et al. 2003; Holthuijsen et al. 2012) that propose drag coefficient saturation by sea foam and spray (Powell et al. 2003; Donelan et al. 2004).

For the crosswind component of surface wind stress for $|\mathbf{U}_{10}| < 30 \text{ m s}^{-1}$, the angle between wind and stress is nearly zero, indicating that the assumed alignment between wind and stress in Monin–Obukhov similarity theory is valid under Typhoon Megi at low wind speeds. For $|\mathbf{U}_{10}| > 30 \text{ m s}^{-1}$, the angle between wind and stress vectors is $> 15^\circ$ (Fig. 2.1b), slightly greater

than a numerical model result from the front-right quadrant of tropical cyclones (Chen et al. 2013). Previous studies suggest swell traveling under the tropical cyclone may yield significant crosswind stress (Chen et al. 2013; Reichl et al. 2014; Potter et al. 2015). The C_{\perp} decreases for $|\mathbf{U}_{10}| > 40 \text{ m s}^{-1}$, similar to the dependence of C_{\parallel} on wind speed.

2.9 Summary

Velocity, temperature, and salinity measurements were taken by seven EM-APEX floats air-deployed on the right side of Typhoon Megi, a small and fast-moving category 5 typhoon, during the ITOP experiment in 2010. Downwind and crosswind drag coefficients were computed from three floats closest to the eye using the depth-integrated linear momentum equation.

Extensive efforts are devoted to estimate the uncertainty of the derived drag coefficients due to the uncertainty in velocity measurements, and imperfections in removing non-wind driven currents. Estimates of the ‘apparent’ drag coefficients are made assuming a linear momentum equation. PWP3D model simulations show that the momentum balance is approximately linear before the arrival of the eye, but with significant components of nonlinear and pressure gradient force after the passage of Megi. The effects of nonlinear and pressure gradient terms before the arrival of the typhoon are corrected using the model to obtain the adjusted downwind and crosswind drag coefficients (Fig. 2.1 and Table 2.2).

At $|\mathbf{U}_{10}| = 27 \text{ m s}^{-1}$, our estimates of adjusted downwind drag coefficient $\tilde{C}_{\parallel} = 3.2 \pm 0.6 \times 10^{-3}$ are greater than the C_d reported in previous studies (Powell et al. 2003; Donelan et al. 2004; Black et al. 2007; Jarosz et al. 2007). At $|\mathbf{U}_{10}| = 31 \text{ m s}^{-1}$, our estimates of $\tilde{C}_{\parallel} = 3.5 \pm 0.7 \times 10^{-3}$ are much greater than previously reported and a factor of two greater than the drag coefficient on the right side of tropical cyclones reported by Holthuijsen et al. (2012). Our results are in agreement

with the numerical model study by Chen et al. (2013), that reports a stronger drag coefficient, $> 3.0 \times 10^{-3}$, in the front-right quadrant of tropical cyclones. At higher wind speeds our estimates of $\widetilde{C}_{\parallel}$ decrease to 2.0×10^{-3} at $|\mathbf{U}_{10}| = 50 \text{ m s}^{-1}$ and remain nearly constant to our observed maximum wind speed of 62 m s^{-1} , consistent with the C_d reported by Bell et al. (2012).

We present, for the first time, measurements of adjusted crosswind drag coefficient \widetilde{C}_{\perp} as a function of $|\mathbf{U}_{10}|$ in tropical cyclones. For $|\mathbf{U}_{10}| \leq 25 \text{ m s}^{-1}$, estimates of \widetilde{C}_{\perp} are $\pm 0.5 \times 10^{-3}$. At $|\mathbf{U}_{10}| = 27 \text{ m s}^{-1}$, the wind stress vector is about 10° clockwise from the wind vector, consistent with the report by Zhang et al. (2009) for lower wind speeds. For $|\mathbf{U}_{10}| > 30 \text{ m s}^{-1}$, \widetilde{C}_{\perp} increases to $> 1.0 \times 10^{-3}$, and the wind stress vector is mostly $> 20^\circ$ clockwise from the wind vector. Chen et al. (2013), in their atmosphere–wave–ocean model simulations, report a similar result near the center of a tropical cyclone. As the wind speed increases from 40 to 60 m s^{-1} , \widetilde{C}_{\perp} decreases to 0.7×10^{-3} . The decrease of \widetilde{C}_{\perp} at higher wind speeds, say $> 40 \text{ m s}^{-1}$, is similar to the decrease in $\widetilde{C}_{\parallel}$.

This chapter focuses on the drag coefficients under Typhoon Megi and on the details of the analysis method. Similar data are available for four other tropical cyclones (Hurricane Frances 2004, Hurricane Gustav 2008, Hurricane Ike 2008, and Typhoon Fanapi 2010). Drag coefficient analyses using the same method are presented in Chapter 3.

Float Name	First Profiling Time (UTC)	Lon (°E)	Lat (°N)
em3763c	00:59 UTC 16 Oct. 2010	128.3	18.7
em4913a	00:52 UTC 16 Oct. 2010	128.3	19.1
em3766c	00:35 UTC 16 Oct. 2010	128.3	19.4
em4911a	00:35 UTC 16 Oct. 2010	128.3	19.7
em4915a	00:32 UTC 16 Oct. 2010	128.3	20.0
em4390d	00:25 UTC 16 Oct. 2010	128.3	20.4
em4908a	00:11 UTC 16 Oct. 2010	128.3	20.7

Table. 2.1. EM-APEX float deployment locations in Megi at the time they began profiling during the ITOP experiment.

Drag Coefficient in Typhoon Megi	Wind Speed at 10m Above the Sea Surface, $ \mathbf{U}_{10} $ (m s^{-1})			
	$ \mathbf{U}_{10} = 27 \pm 2$	$ \mathbf{U}_{10} = 31 \pm 3$	$ \mathbf{U}_{10} = 37 \pm 3$	$ \mathbf{U}_{10} = 56 \pm 9$
Downwind \tilde{C}_{\parallel} ($\times 1000$)	3.2 ± 0.6	3.5 ± 0.7	2.6 ± 0.5	2.0 ± 0.4
Crosswind \tilde{C}_{\perp} ($\times 1000$)	0 ± 0.5	1.3 ± 0.5	1.6 ± 0.5	0.7 ± 0.3

Table. 2.2. The mean and standard errors of adjusted downwind and crosswind drag coefficients at different wind speed intervals during Typhoon Megi. Same as the values shown in Fig. 2.1.

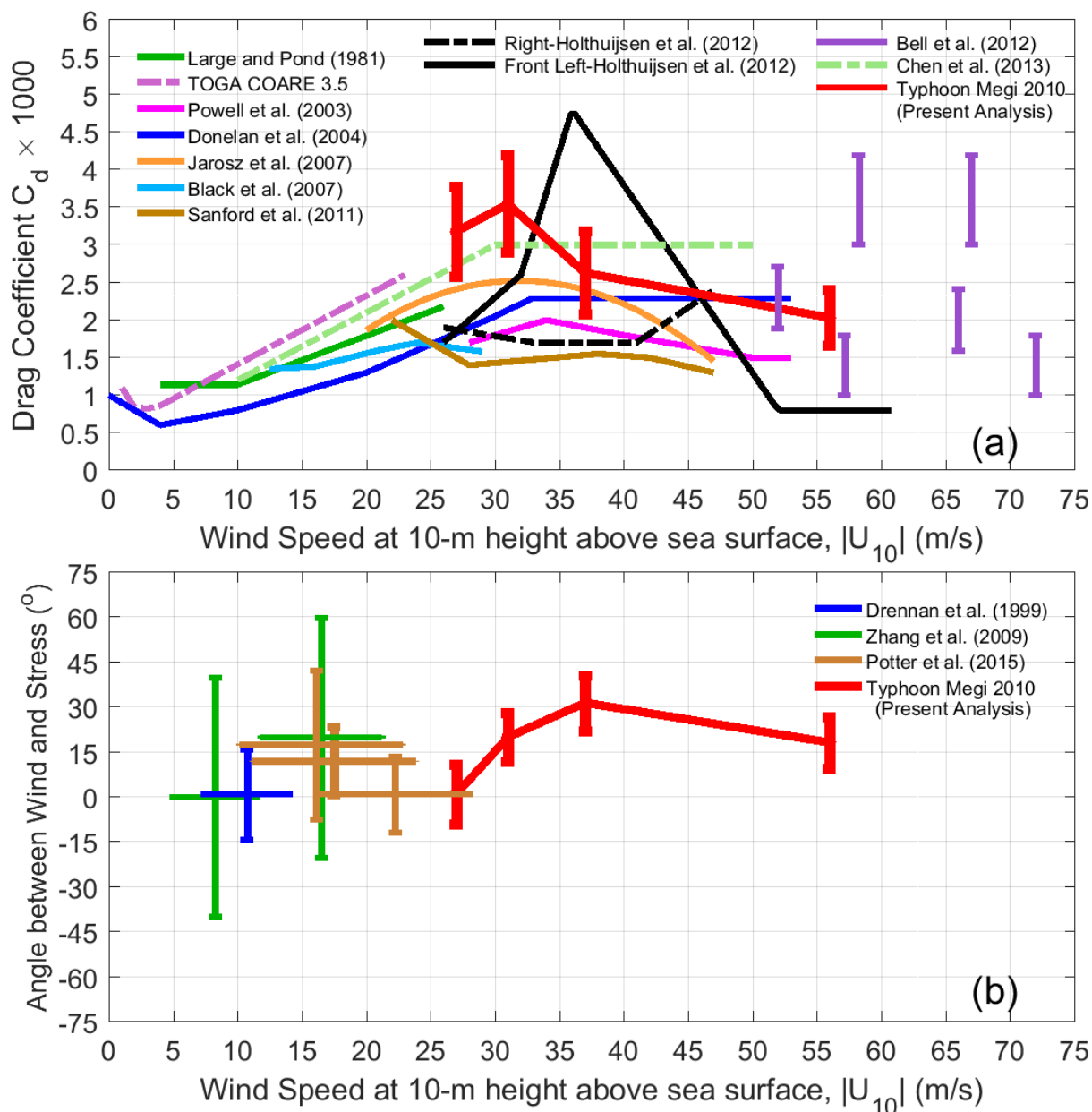


Fig. 2.1. (a) The drag coefficient C_d as a function of wind speed at 10 m above the sea surface $|U_{10}|$ from our analysis (heavy red lines) and as proposed by previous investigators (other colors). (b) Angle between the surface wind and stress vectors from our analysis (heavy red) and from Drennan et al. (1999, Fig. 6), Zhang et al. (2009, Figs. 1 and 3) and Potter et al. (2015, Figs. 1 and 4). Measured wind speed from these investigators is extrapolated to 10 m above the sea surface assuming a logarithmic wind profile. The horizontal and vertical bars describe the ranges

of their data. The positive angle implies a stress vector that points clockwise from the wind vector.

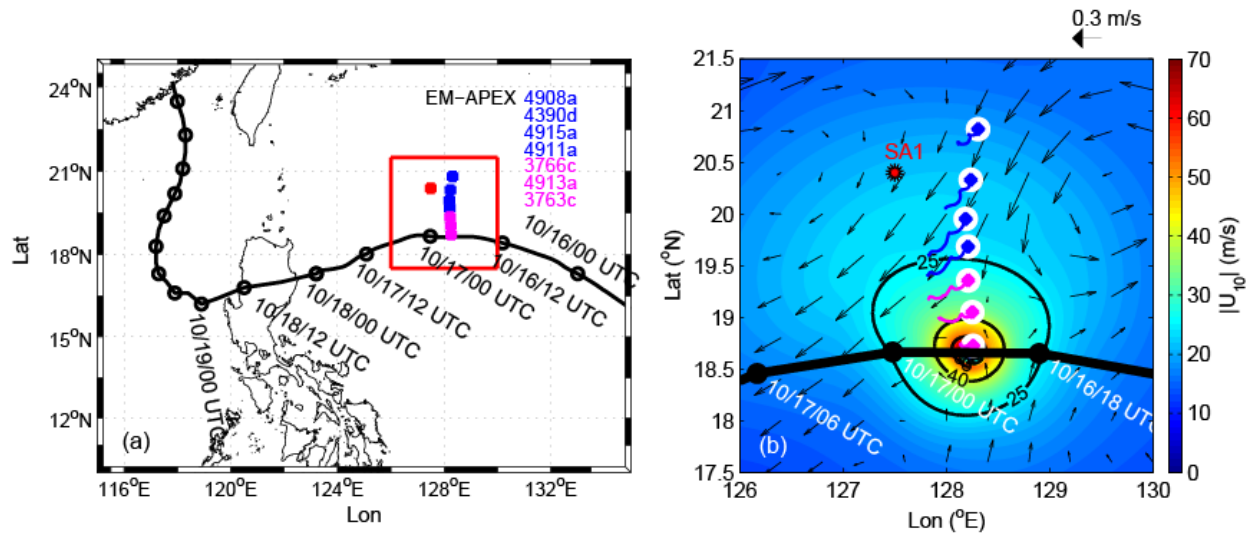


Fig. 2.2. (a) Typhoon Megi's track (black curve with dots), deployment positions of EM-APEX floats (blue and magenta dots), and position of mooring SA1 (red dot), and (b) the wind map of wind speed at 10 m above the sea surface (color shading) at 20:30 UTC 16 October at the arrival time of Typhoon Megi at the float array, AVISO surface geostrophic current velocity (black arrows) on 17 October, EM-APEX float positions and trajectories (blue and magenta dots and curves), and mooring SA1 position (red dot). Typhoon track is labeled with time as month/day/hour UTC. Float deployment details are listed in Table 2.1.

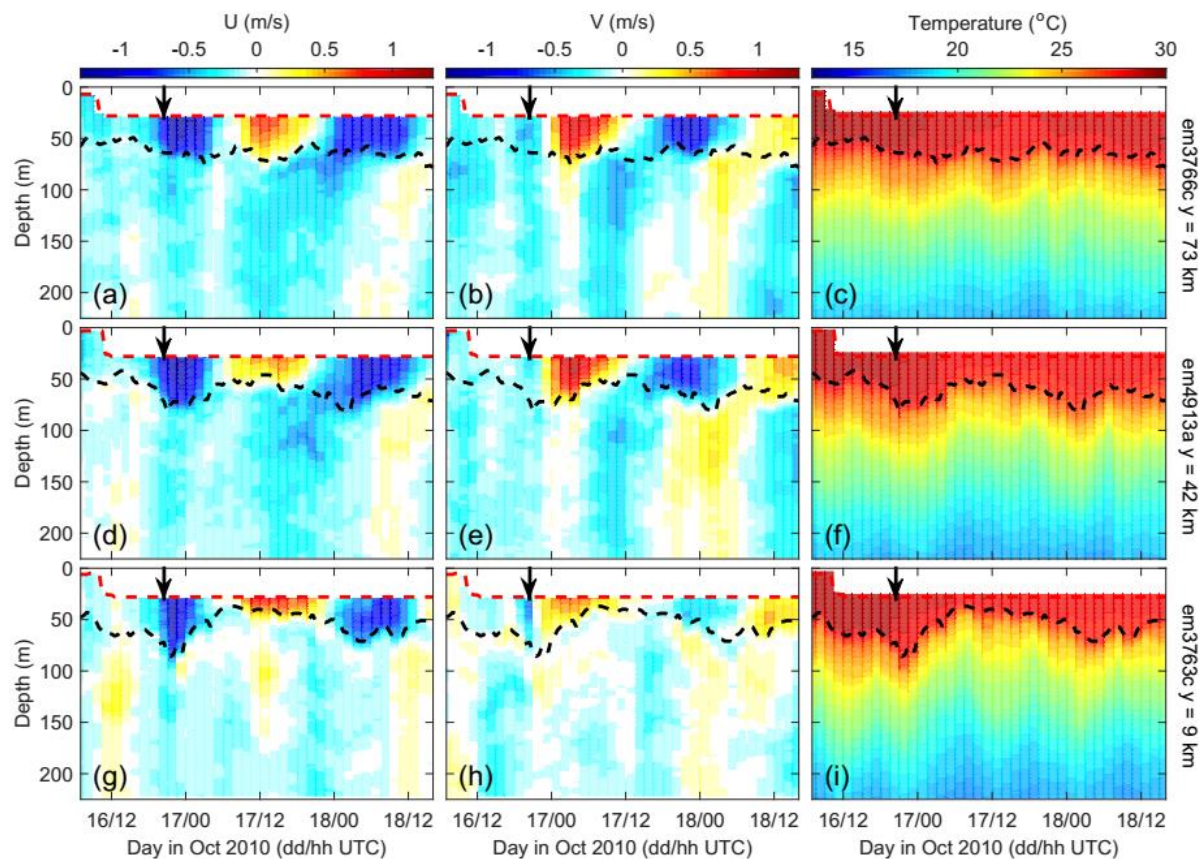


Fig. 2.3. Zonal velocity (left column a, d, g), meridional velocity (middle column b, e, h), and temperature (right column c, f, i) measured by three EM-APEX floats (rows). The dashed red lines mark the shallowest depth of float measurements. The distance of each float from Megi's track is labeled to the right of the right column. The black arrows mark the closest approach of Typhoon Megi to the float array, 20:30 UTC 16 October. The black dash curves represent the depth of the surface mixed layer.

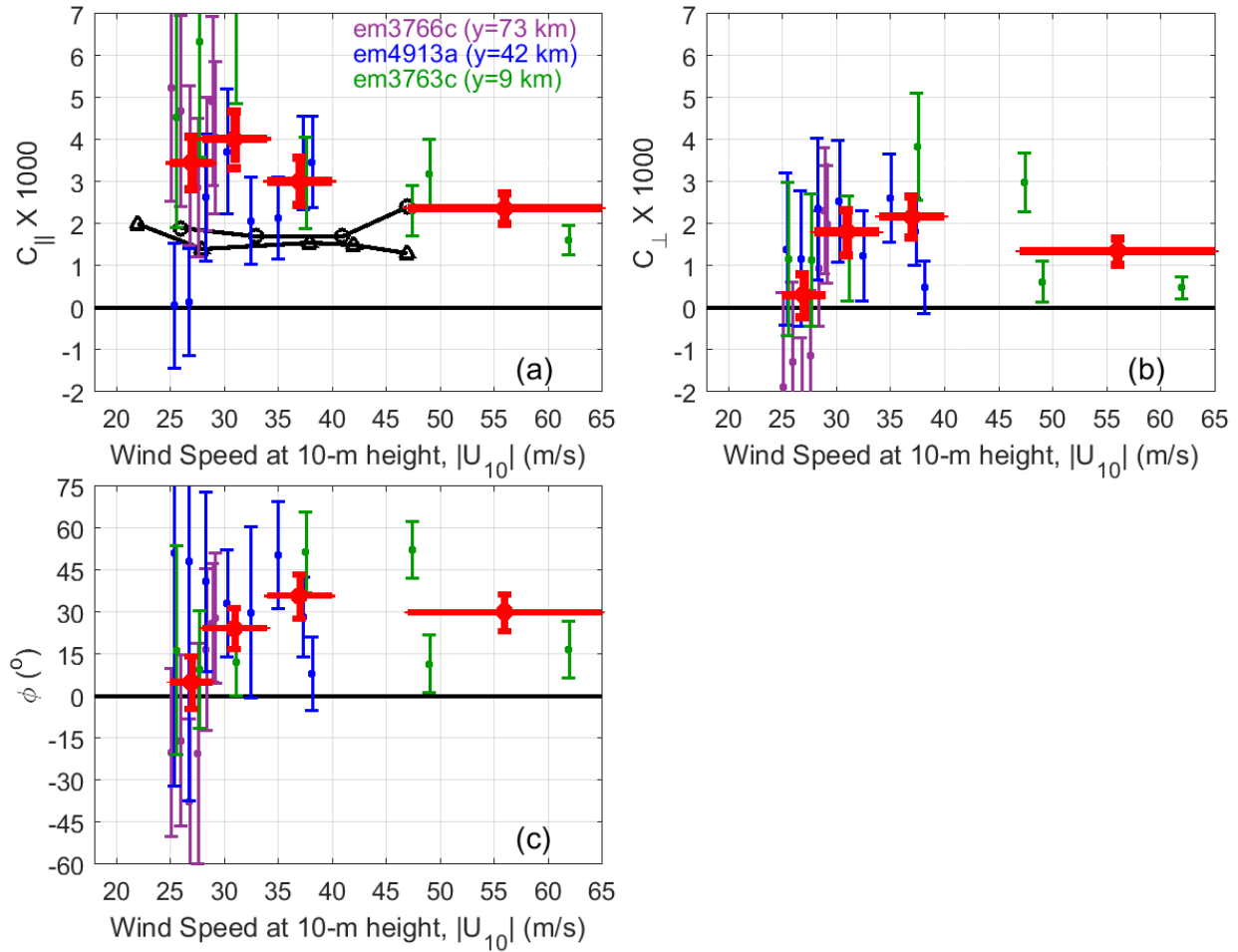


Fig. 2.4. Apparent downwind drag coefficient C_{\parallel} (a), apparent crosswind drag coefficient C_{\perp} (b), and angle ϕ between surface wind stress vector and wind vector (c) for $|U_{10}| > 22 \text{ m s}^{-1}$. This intermediate product is further corrected to give the final results shown in Fig. 2.1. The dots and vertical bars represent the mean of apparent drag coefficients and its \pm one standard deviation, computed using profiles of velocity measurements taken from three EM-APEX floats (purple, blue, and green colors) at different distances from the storm track (labeled). The drag coefficients reported by Sanford et al. (2011) and Holthuijsen et al. (2012) are shown in (a) as black lines with circles and triangles, respectively. Red dots show the averages of apparent drag coefficients in bins of different wind speeds (horizontal lines). The vertical red line represents the \pm one standard deviation of apparent drag coefficient averages.

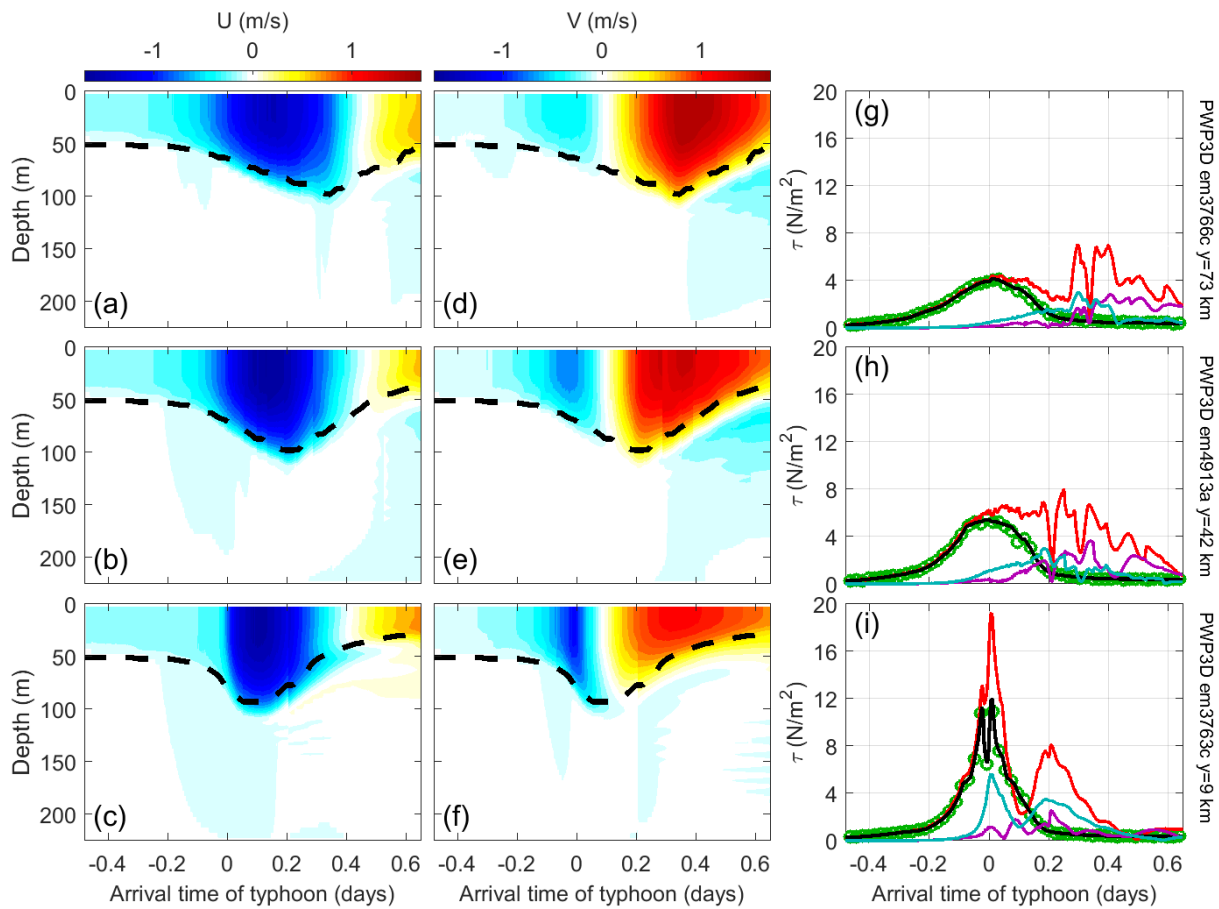


Fig. 2.5. PWP3D model simulations of zonal current velocity (left column a–c), meridional current velocity (middle column d–f), estimated surface wind stress via momentum budget and linear momentum budget (right column g–i) at the three floats’ (em3763c, em4913a and em3766c) positions (rows). Distances of floats from Megi’s track are labeled to the right of the right column. Time is relative to the arrival of Typhoon Megi’s eye at the float array. Black dashed curves in (a)–(f) represent the base of the surface mixed layer. Black lines in (g)–(i) show the surface wind stress computed using observed winds in Typhoon Megi and the parameterization of apparent downwind drag coefficient. Green circles in (g)–(i) are the estimates of surface wind stress computed using the depth-integrated momentum budget (Eq. 2.3). Red curves are the estimates of surface wind stress computed using the depth-integrated

linear momentum budget (Eq. 2.4). Purple curves are the pressure gradient term $\frac{1}{\rho_0} \nabla_h p$ in the depth-integrated momentum budget (Eq. 2.3), and cyan curves are the sum of nonlinear advection terms, $\mathbf{v} \nabla_h \cdot \mathbf{v}$ and $\mathbf{v} \cdot \nabla_h \mathbf{v}$, in the depth-integrated momentum budget (Eq. 2.3).

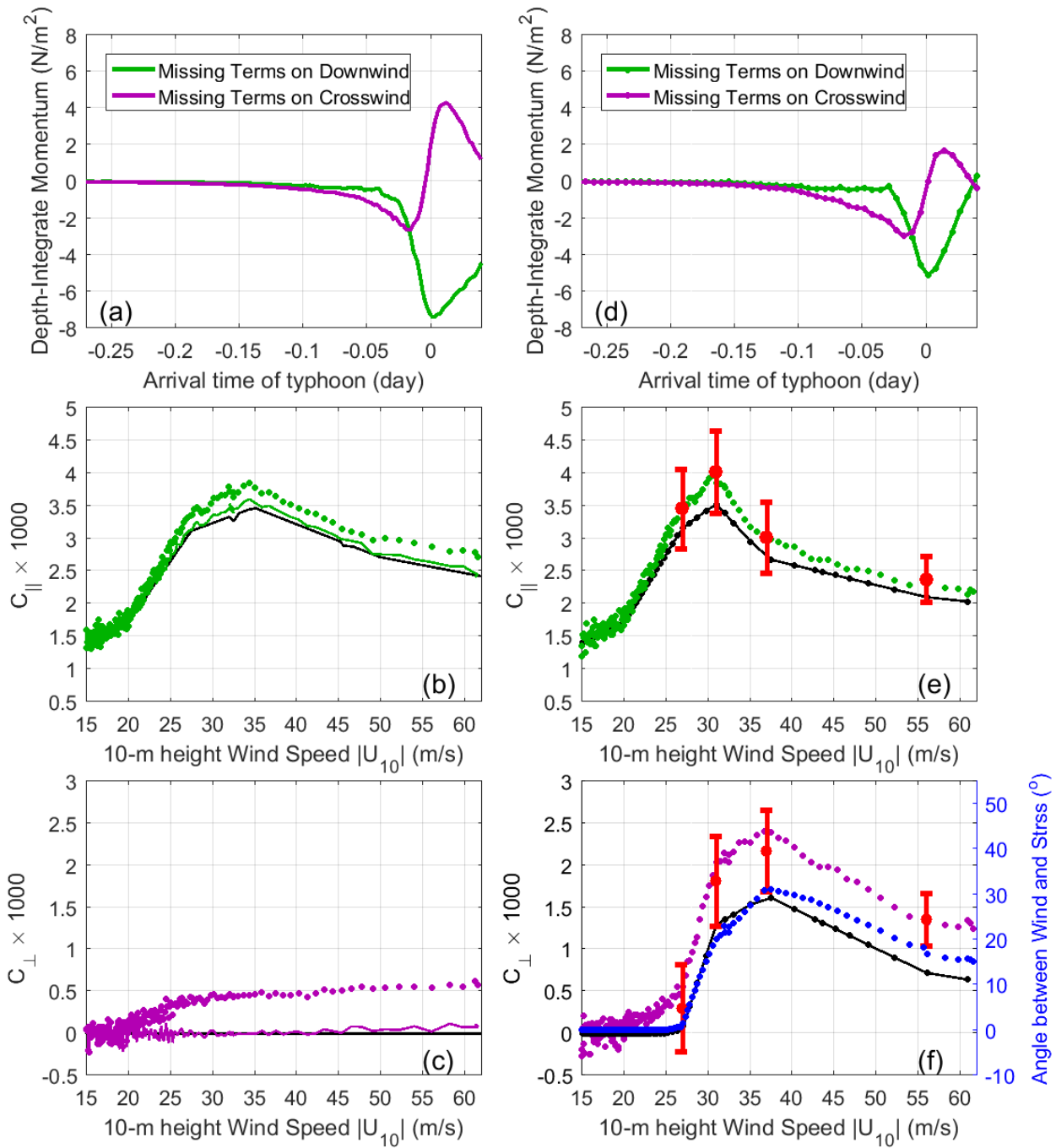


Fig. 2.6. Correction to the apparent drag coefficients due to nonlinear and pressure gradient terms in the momentum budget. Left column, the results from the PWP3D model employing the apparent downwind drag coefficient obtained in this analysis: (a) the sum of the nonlinear and pressure gradient terms on the downwind (green curve) and crosswind (purple curve) directions,

(b) the apparent downwind drag coefficient (black curve) and the drag coefficient derived assuming a linear momentum balance (green dots), (c) the zero crosswind drag coefficient used in the PWP3D model (horizontal black line) and the crosswind drag coefficient derived assuming a linear momentum balance (purple dots). Right column, the results from the PWP3D model employing the adjusted downwind and crosswind drag coefficients: (d) the sum of the nonlinear and pressure gradient terms on the downwind (green curve) and crosswind (purple curve) directions, (e) the adjusted downwind drag coefficient (black curve), the downwind drag coefficient computed from the linear momentum budget (green dots), and the observed apparent downwind drag coefficient (red dots and vertical bars), (f) the adjusted downwind drag coefficient (black curve), the crosswind drag coefficient computed from the linear momentum budget (purple dots), and the observed apparent crosswind drag coefficient (red dots and vertical bars). The blue dots in (f) show the angle between the wind and stress computed in simulation B. These final results are replotted in Fig. 2.1.

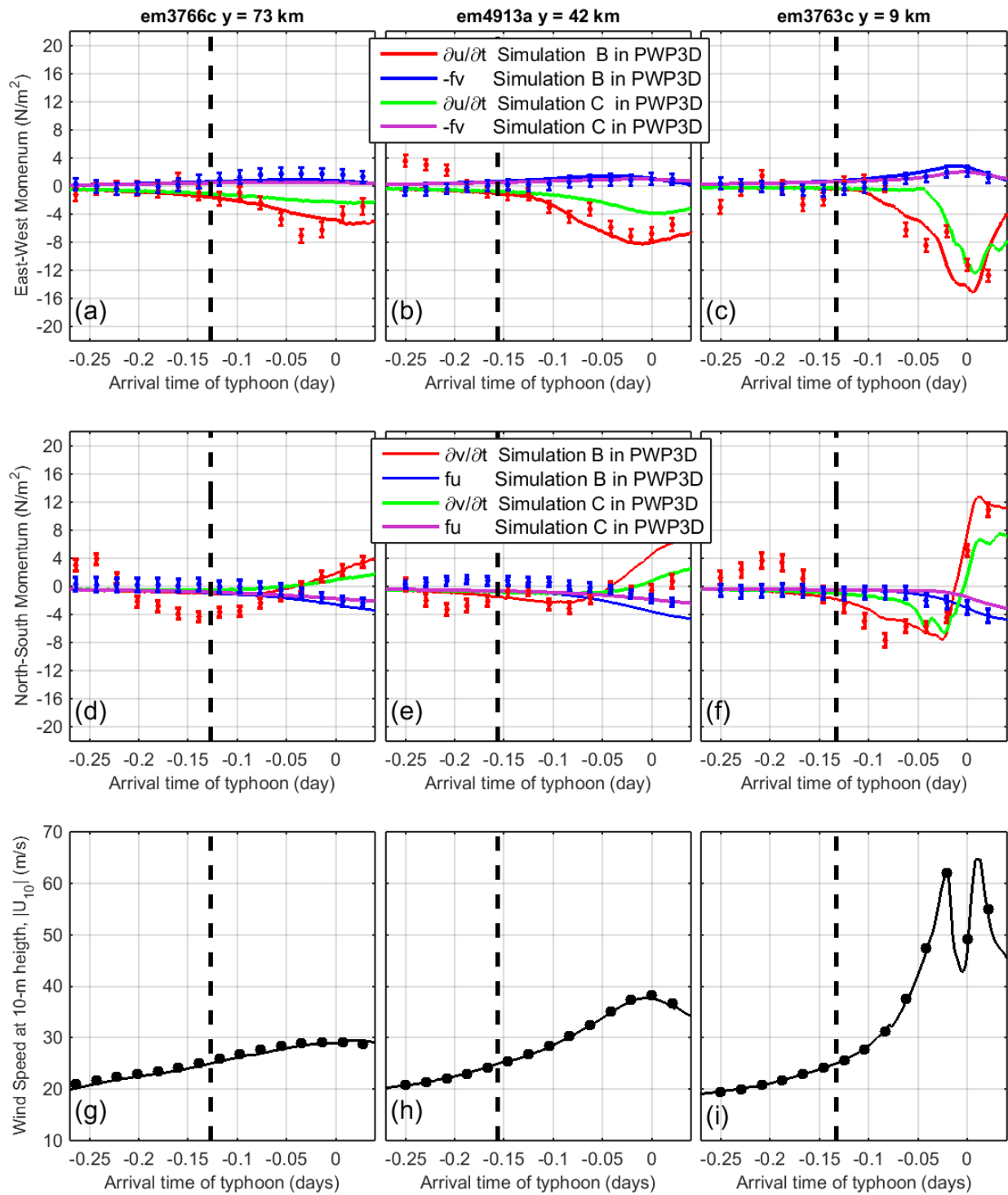


Fig. 2.7. Comparisons of float observations (dots with vertical error bars \pm one standard deviation) and PWP3D model simulations of the depth-integrated (0–150m) storm-induced zonal

linear momentum terms (a–c), and meridional linear momentum terms (d–f). Simulation B is performed using adjusted drag coefficients derived in the present analysis (red and blue curves in a–f). Simulation C is performed using the C_d reported by Holthuijsen et al. (2012) (green and purple curves in a–f). The observed wind speed at 10 m above the sea surface $|\mathbf{U}_{10}|$ at the floats' positions (black line with dots) is shown in the bottom panels. The abscissa is the time relative to the arrival time of Typhoon Megi's eye at the float array. The vertical dashed line represents the time when the measured wind speed at the float positions reaches 25 m s^{-1} .

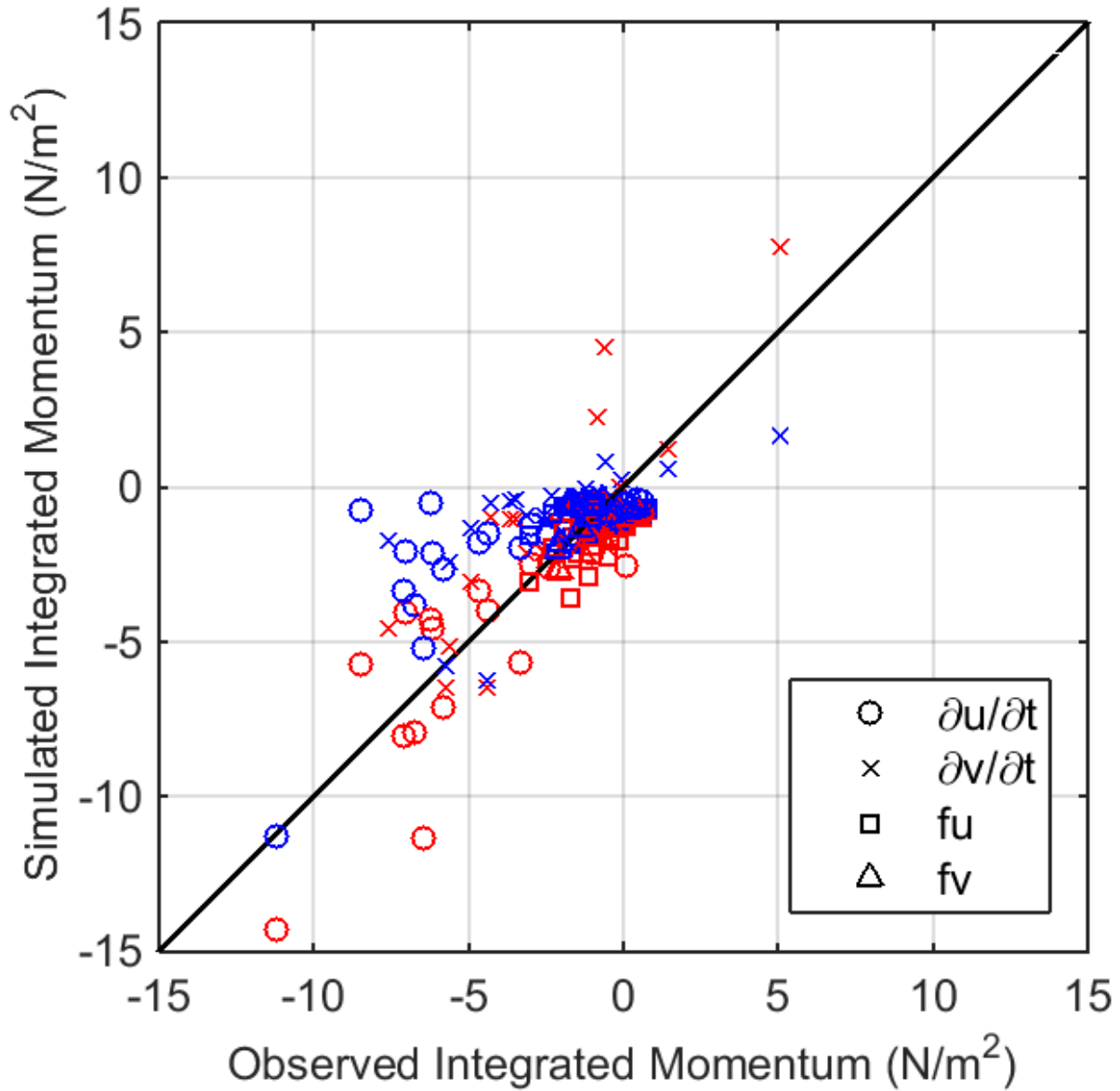


Fig. 2.8. Comparisons of float observations and model results of the depth-integrated (0–150 m) storm-induced linear momentum terms (circle: $\partial u/\partial t$, cross: $\partial v/\partial t$, square: $f \times u$ and triangle: $f \times v$) in Simulation B (red) and Simulation C (blue) before the passage of Typhoon Megi and at $|\mathbf{U}_{10}| > 25 \text{ m s}^{-1}$.

Chapter 3. Scaling of Drag Coefficients under Five Tropical Cyclones

Nineteen EM-APEX floats deployed from aircraft measured the profiles of horizontal ocean current velocity in five tropical cyclones. The surface wind stress τ is estimated using the float velocity measurements, assuming the linear momentum budget balance. At wind speed $|\mathbf{U}_{10}| = 25\text{--}40 \text{ m s}^{-1}$, the adjusted downwind drag coefficient \tilde{C}_{\parallel} in the front-right sector of tropical cyclones is $1.1\text{--}3.1 \times 10^{-3}$, higher than that in the front-left sector, $0.8\text{--}1.7 \times 10^{-3}$. The \tilde{C}_{\parallel} increases with decreasing non-dimensional effective wind duration ζ^* , a function of wind forcing, storm translation speed and fetch. At low ζ^* , we propose that surface waves with larger amplitude are forced more efficiently by the wind under faster storms, and result in stronger wave breaking and momentum transfer into ocean currents, i.e., more efficient momentum transfer and higher drag coefficients. At $|\mathbf{U}_{10}| > 40 \text{ m s}^{-1}$, the \tilde{C}_{\parallel} is saturated, $\sim 1.6 \times 10^{-3}$. The drag angle ϕ to \mathbf{U}_{10} is scattered from $-15\text{--}40^\circ$ at $|\mathbf{U}_{10}| = 25\text{--}40 \text{ m s}^{-1}$, and decreases with increasing $|\mathbf{U}_{10}|$. The data-based parameterizations of $\tilde{C}_{\parallel}(\zeta^*)$ and $\phi(\zeta^*)$ at $|\mathbf{U}_{10}| = 25\text{--}40 \text{ m s}^{-1}$ may provide guidance for future model studies on the oceanic response and maximum cooling under tropical cyclones.

3.1 Introduction

Surface wind stress τ of tropical cyclones acts as a major forcing to upper ocean dynamics, e.g., near-inertial current, and then induces significant shear instability, vertical mixing, and cooling on the right side of storm tracks (Price et al. 1994). Momentum transfer into the ocean via the τ and induced upper ocean cooling can both modify the predictions of tropical cyclone maximum potential intensity (Emanuel 1995; Balaguru et al. 2015). The τ in tropical

cyclone winds has been studied extensively (Powell et al. 2003; Donelan et al. 2004; Sanford et al. 2011; Takagaki et al. 2012; Hsu et al. 2017) and is often parameterized by a drag coefficient C_d as $|\boldsymbol{\tau}| = \rho_{\text{air}} C_d |\mathbf{U}_{10}|^2$, where ρ_{air} is the air density, and \mathbf{U}_{10} the wind at the 10-m height above the sea surface.

Many previous studies conclude that C_d increases with wind speed at $|\mathbf{U}_{10}| < 20 \text{ m s}^{-1}$ (Large and Pond 1981; Edson et al. 2013) and remains constant at $1.5\text{--}2.0 \times 10^{-3}$ at $|\mathbf{U}_{10}| > 40 \text{ m s}^{-1}$ (Powell et al. 2003; Sanford et al. 2011; Hsu et al. 2017). At $|\mathbf{U}_{10}| = 25\text{--}40 \text{ m s}^{-1}$, reported estimates of C_d scatter greatly from $1.5\text{--}4.5 \times 10^{-3}$ (Powell et al. 2003; Donelan et al. 2004; Jarosz et al. 2007; Sanford et al. 2011; Holthuijsen et al. 2012; Hsu et al. 2017), presumably because factors other than wind speed are important, such as the spatial variability of surface gravity waves (Holthuijsen et al. 2012). Several studies use atmosphere–wave–ocean coupling models (Chen et al. 2013; Reichl et al. 2014) to simulate the map of C_d under tropical cyclones. The simulated C_d at the front-right quadrant of tropical cyclones is higher than that at the front-left quadrant, inconsistent with the spatial pattern observed by Holthuijsen et al. (2012). The $\boldsymbol{\tau}$ has also been reported to misalign with \mathbf{U}_{10} under tropical cyclones (Potter et al. 2015; Hsu et al. 2017), presumably due to the alteration of $\boldsymbol{\tau}$ by surface wave propagation (Potter et al. 2015).

In Chapter 2, drag coefficients under Typhoon Megi using EM-APEX floats are estimated assuming the linear momentum balance. The biases of drag coefficient estimates due to the linear momentum assumption and non-wind driven current are corrected. Here, we extend the analysis using all float measurements at $|\mathbf{U}_{10}| > 25 \text{ m s}^{-1}$ under Hurricane Frances 2004, Hurricane Gustav 2008, Hurricane Ike 2008, Typhoon Fanapi 2010, and Megi (section 3.5). The variability of drag coefficients in five tropical cyclones are parameterized using a non-dimensional parameter of surface waves (section 3.6) instead of $|\mathbf{U}_{10}|$.

3.2 Experiments

As a part of the 2004 Coupled Boundary Layer Air-Sea Transfer Experiment (CBLAST) (Black et al. 2007) and 2010 Impact of Typhoons on the Ocean in the Pacific (ITOP) programs (D’Asaro et al. 2014), a series of experiments were conducted in tropical cyclones, including Frances 2004, Gustav 2008 (Rabe et al. 2015), Fanapi 2010, and Megi 2010 (Fig. 3.1). Nineteen EM-APEX floats were air-launched by aircraft from about 1 day before the passage of these four tropical cyclones. The float deployed on the left side of Gustav’s track drifted to the right side of Hurricane Ike’s track. The National Center for Atmospheric Research/Earth Observing Laboratory (NCAR/EOL) deployed 668 dropsondes within ± 1 day relative to the time when tropical cyclones passed the floats, and measured the wind within 100-m height above the sea surface. Stepped-Frequency Microwave Radiometers (SFMR) mounted on the bottom of the C-130 aircraft measured brightness temperature, which is used to estimate Fanapi and Megi wind speeds at 10-m height above the sea surface $|\mathbf{U}_{10}|$ (D’Asaro et al. 2014). SFMR estimates of $|\mathbf{U}_{10}|$ were also taken in Frances, Gustav, and Ike. They were archived and provided by the Atlantic Oceanographic and Meteorological Laboratory/Hurricane Research Division/National Oceanic and Atmospheric Administration (AOML/HRD/NOAA). Tropical cyclones’ wind maps (Fig. 3.1) are processed using the wind measurements (Appendix A), and used to interpolate $|\mathbf{U}_{10}|$ at the float positions.

Megi had the smallest radius of maximum wind speed ($R_{\max} = 14$ km), the fastest translation speed ($U_h = 7.7$ m s⁻¹), and the greatest maximum wind speed ($V_{\max} = 75$ m s⁻¹) (Table 3.1). Gustav has similar V_{\max} with Fanapi, but larger R_{\max} and faster U_h . Ike has the largest R_{\max} of 75 km but the lowest V_{\max} of 41 m s⁻¹ in the five tropical cyclones. Frances has

greater V_{\max} and smaller R_{\max} than Gustav and Ike, i.e., the hurricane with greatest wind speed in our study.

3.3 EM-APEX Float Measurements

EM-APEX floats measured vertical profiles of temperature and salinity, using a SeaBird Electronics SBE-41 CTD sensor mounted on the top end of the floats, and electrical voltage, using two pairs of orthogonal rotating electrodes, in the upper 220 m. The voltage measurements were processed to estimate ocean current velocity in every 50-s data processing window with 25 s overlapped (Sanford et al. 2005). The vertical profiling speed is about 0.11 m s^{-1} , so that the vertical resolution of current velocity measurements is about 3–4 m. During the passage of Frances and Megi, the floats were submerged and profiled below 30 m depth, to avoid damage by storm-induced ocean surface waves (Sanford et al. 2011; Hsu et al. 2017). The missing measurements in the upper 30 m were extrapolated using the shallowest velocity measurements below 30 m depth. Measurements and GPS positions were transmitted by Iridium satellites when floats surface.

Twelve EM-APEX floats profiled the oceanic response to winds greater than 25 m s^{-1} (Table 3.1). Seven floats passed the right side of tropical cyclones' tracks, three floats passed the eyes of Frances, Fanapi and Megi, and two floats passed the left side of the Gustav and Fanapi tracks. Float measurements taken by these twelve floats are used to estimate surface wind stress at $|\mathbf{U}_{10}| > 25 \text{ m s}^{-1}$. The surface mixed layer depth (MLD) is defined as the shallowest depth with a density gradient greater than 0.03 kg m^{-4} and the density differing from the surface value is more than 0.3 kg m^{-3} . The MLD is less than 80 m when tropical cyclones passed the floats. The horizontal ocean current speed $|\mathbf{v}|$ in the MLD is $> 0.7 \text{ m s}^{-1}$ on the right side of the tropical

cyclones' tracks due to significant inertial coupling between wind and surface current (Price et al. 1994), and is greater than the value of $< 0.4 \text{ m s}^{-1}$ on the left side.

3.4 Estimating Adjusted Drag Coefficients

In Chapter 2, the apparent surface wind stress (Eq. 2.4) is computed using the estimates of apparent wind-forced velocity profiles \mathbf{v}_{wnd} before the passage of Megi (section 2.5), and is corrected for the biases $\Delta\boldsymbol{\tau}$ due to the missing momentum terms in the linear momentum budget (section 2.7). The adjusted downwind drag coefficients \tilde{C}_{\parallel} (Eq. 2.7) and the angle ϕ of the corrected surface wind stress $\tilde{\boldsymbol{\tau}}$ clockwise from \mathbf{U}_{10} (Eq. 2.6), are computed using the mean and standard deviation of \mathbf{U}_{10} at the float positions. This method to adjust drag coefficients is repeated using the other float measurements in Frances, Gustav, Ike, and Fanapi. The resulting drag coefficients are parameterized using a new parameter of surface waves (section 3.6).

The apparent surface wind stress is estimated (Eq. 2.4) using the \mathbf{v}_{wnd} at each float (Appendix B.3) in the upper 100 m, at least 20 m deeper than the surface mixed layer base (Table 3.1). The selected integration depth is justified using PWP3D model simulations, as in section 2.6, which confirm that the turbulent fluxes at 100-m depth are negligible. One thousand realizations of normally distributed \mathbf{U}_{10} are generated using the mean and standard deviation of wind speed and direction ($< 3.4 \text{ m s}^{-1}$ and 10° in Appendix A.2) to compute apparent drag coefficients. The estimates of apparent drag coefficients are averaged in three different bins of wind speed ($|\mathbf{U}_{10}| = 27.5 \pm 2.5$, 35 ± 5 , and $> 40 \text{ m s}^{-1}$), and used to simulate the oceanic response to the mapped $|\mathbf{U}_{10}|$ at the float positions in the PWP3D model (section 2.6). For $|\mathbf{U}_{10}| < 25 \text{ m s}^{-1}$, the value of C_d described by Large and Pond (1981) is used. The adjusted drag coefficients are derived by directly subtracting the effects of simulated nonlinear and pressure gradient terms

from the apparent drag coefficients (section 2.7). The corrections on the apparent downwind drag coefficient are $< 0.4 \times 10^{-3}$ (Table 3.2). The angle ϕ of drag clockwise from \mathbf{U}_{10} decreases because the simulated terms of storm-induced pressure gradient and nonlinear momentum point toward the eyes (Fig. 2.6).

The stochastic simulations are used to quantify the error bars of the adjusted drag coefficients in each wind speed bin (Fig. 3.2), thus including the uncertainties of individual estimates of adjusted drag coefficients at each float position. The mean and standard deviation of individual estimates of adjusted drag coefficients are used to generate 1,000 realizations of drag coefficients assuming a normal distribution (section 2.5). The realizations are averaged in each wind speed bin to generate the adjusted drag coefficient averages. The standard deviations of the adjusted drag coefficient averages in each wind speed bin are computed (Fig. 3.2), yielding $< 0.5 \times 10^{-3}$ under all tropical cyclones.

3.5 Adjusted Drag Coefficients by Tropical Cyclone Sector

Estimates of adjusted drag coefficients are presented in two sectors of tropical cyclones: front-right and front-left, divided by $\theta_s = -10^\circ$ (Fig. 3.2c) (where θ_s is the angle clockwise from the storms' translation direction). The front-right sector includes estimates computed using measurements from floats passing under the eyes and the right side of tropical cyclones' tracks; the front-left sector includes measurements from floats on the left side of tracks.

At $|\mathbf{U}_{10}| = 25\text{--}30 \text{ m s}^{-1}$, the \tilde{C}_{\parallel} in the front-right sector of all tropical cyclones is $1.1\text{--}2.9 \times 10^{-3}$ (Table 3.2). The \tilde{C}_{\parallel} is observed only in the front-left sector of Gustav and Fanapi, 0.8×10^{-3} and 1.7×10^{-3} , respectively. Higher \tilde{C}_{\parallel} in the front-right sector of the storms agrees with the simulated spatial pattern of C_d in previous studies (Moon et al. 2004; Chen et al. 2013), but is

inconsistent with that reported by Holthuijsen et al. (2012). At $|\mathbf{U}_{10}| = 30\text{--}40 \text{ m s}^{-1}$, the \tilde{C}_{\parallel} in the front-right sector of all tropical cyclones is about $2.2\text{--}3.1 \times 10^{-3}$, higher than the peak C_d reported by Powell et al. (2003). The scattering of \tilde{C}_{\parallel} decreases at the higher wind speed. The \tilde{C}_{\parallel} in the front-left sector of Fanapi is nearly consistent at $|\mathbf{U}_{10}| = 25\text{--}40 \text{ m s}^{-1}$, $\sim 1.6 \times 10^{-3}$. At $|\mathbf{U}_{10}| > 40 \text{ m s}^{-1}$, the \tilde{C}_{\parallel} in the front-right sector of Fanapi and Megi is saturated, $\sim 1.6 \times 10^{-3}$, in good agreement with the saturation of C_d reported previously (Powell et al. 2003; Jarosz et al. 2007).

At $|\mathbf{U}_{10}| = 25\text{--}30 \text{ m s}^{-1}$, the angle ϕ of drag clockwise from the wind \mathbf{U}_{10} in the front-right sector of Frances, Ike, and Fanapi is $\sim 15\text{--}40^\circ$. The $\tilde{\tau}$ in the front-right sector of Megi is nearly aligned with the wind \mathbf{U}_{10} . The ϕ is $\sim -15^\circ$ in the front-right sector of Gustav and 40° in the front-left sector. Interestingly, the spatial variability of ϕ in Fanapi is opposite that in Gustav. At $|\mathbf{U}_{10}| = 30\text{--}40 \text{ m s}^{-1}$, the ϕ in the front-right sector of tropical cyclones become less scattered than at $|\mathbf{U}_{10}| = 25\text{--}30 \text{ m s}^{-1}$, within $\pm 20^\circ$. The decreasing scattering of ϕ at the higher wind speed is similar with the trend of \tilde{C}_{\parallel} . At the higher wind speed $|\mathbf{U}_{10}| > 40 \text{ m s}^{-1}$, the $\tilde{\tau}$ is nearly aligned with the wind \mathbf{U}_{10} . The angle ϕ between $\tilde{\tau}$ and \mathbf{U}_{10} decreases with increasing wind speed.

3.6 Scaling Drag Coefficients using Surface Waves

Previous studies suggest that properties of surface waves are important to the drag coefficients (e.g., Smith et al. 1992; Johnson et al. 1998), because wind–wave interactions, e.g., wave breaking, can affect the momentum transferred from the atmosphere into the ocean (Jones and Toba 2012). Estimated drag coefficients will be parameterized by a new non-dimensional parameter of surface waves, which will be discussed in the next section.

The non-dimensional wind duration $\zeta = gT/|\mathbf{U}_{10}|$ (Young 1999) is often used to study the growth of duration-limited surface waves, where g is the gravity, and T the duration of constant

wind speed $|\mathbf{U}_{10}|$ which has been blowing along the fetch χ . In this study, T is defined as the time period when the tropical cyclone passes the fetch χ at a translation speed U_h , i.e., $T = \chi/U_h$.

Hwang et al. (2016) derive a parametric model of $\chi(r,\theta)$ (see Fig. 3.2c for r and θ). Note that the convention of θ is opposite that in Hwang et al. 2016), using the measurements of surface wave directional spectra under Hurricane Bonnie 1998, assuming the fetch-limited relationship between the wave height and fetch length. The χ at the front-right quadrant of the storm (Fig. 3.3) is longer than that at the rear-left quadrant due to the coupling between rotating wind vector and propagating surface waves, and results in higher significant wave height (i.e., the extended fetch effect in Young 2003). Two types of ζ are computed, ζ_c and ζ_χ , assuming the constant fetch χ of 150 km and modeled fetch $\chi(r,\theta)$, respectively (the subscript c represents the constant fetch; the subscript χ represents the modeled fetch), to study the effect of fetch to drag coefficient parameterizations. The standard deviation of ζ (horizontal error bars in Fig. 3.4) is estimated using the mean and standard deviation of $\chi(r,\theta)$ and $|\mathbf{U}_{10}|$, assuming the $\chi(r,\theta)$ and $|\mathbf{U}_{10}|$ normally distributed in each wind speed bin (Table 3.3).

At $|\mathbf{U}_{10}| = 25\text{--}40 \text{ m s}^{-1}$, the \tilde{C}_\parallel in the front-right sector of tropical cyclones is about a constant of 2.5×10^{-3} for $\zeta_c \times 10^{-3} < 8$, and decreases with increasing ζ_c (Fig. 3.4a). Because ζ_c is inversely proportional to U_h , faster storms, such as Megi and Frances, may have higher \tilde{C}_\parallel than the slower storms, such as Ike and Fanapi (Table 3.1). The $\phi = 40^\circ$ (i.e., τ is clockwise from \mathbf{U}_{10}) at $\zeta_c \times 10^{-3} \approx 12$ is found in the front-right sector of Fanapi (Fig. 3.4d). The dependence of \tilde{C}_\parallel and ϕ on the ζ_χ is similar with that on the ζ_c (Fig. 3.4b and e). The mean and standard deviation of the adjusted drag coefficient averages in each wind speed bin (Table 3.2) are used to generate 1,000 realizations in the stochastic simulation, assuming a normal distribution. The realizations in the front-right sector of storms are cubic-fitted using ζ_c and ζ_χ (black lines in Fig.

3.4a, b, d, and e), respectively, assuming the constant drag coefficients at $\zeta_c \times 10^{-3}$ and $\zeta_\chi \times 10^{-3} < 8$. The root-mean-squared error (RMS) of $\tilde{C}_{\parallel}(\zeta_c) = 0.33 \times 10^{-3}$ and $\phi(\zeta_c) = 13^\circ$, are higher than the RMS of $\tilde{C}_{\parallel}(\zeta_\chi) = 0.29 \times 10^{-3}$ and $\phi(\zeta_\chi) = 11^\circ$, respectively. The smaller RMS of $\tilde{C}_{\parallel}(\zeta_\chi)$ than $\tilde{C}_{\parallel}(\zeta_c)$ may suggest that the fetch of surface waves is important to the drag coefficients in the front-right sectors of tropical cyclones. Unlike the \tilde{C}_{\parallel} in the front-right sector of tropical cyclones, the \tilde{C}_{\parallel} in the front-left sector of Fanapi and Gustav increases with increasing ζ_χ (Fig. 3.4b). The \tilde{C}_{\parallel} in the front-left sector of tropical cyclones is lower than that in the front-right sector. The $\phi \approx 40^\circ$ is found in the front-right sector of Gustav with short $\zeta_\chi \times 10^{-3} \approx 5$ (Fig. 3.4e).

The ζ_χ is further modified as the non-dimensional ‘effective’ wind duration $\zeta^* = gT/(|\mathbf{U}_{10}|\cos(\psi))$ (Fig. 3.4c and f), where ψ is the angle between dominant surface waves and \mathbf{U}_{10} . Based on the simulations of ψ forced by idealized tropical cyclones with different U_h in Moon et al. (2004), the ψ can be roughly assumed as 30° at $r < 120$ km in the front-right sector of tropical cyclones (see Fig. 3.2c for r), and $\psi = 30 + 6(U_h/U_{h0})$ ($^\circ$) in the front-left sector, where $U_{h0} = 1$ m s^{-1} . The assumed ψ generally agrees with SRA measurements of ψ at $r < 120$ km in Hwang et al. (2017). The estimates of \tilde{C}_{\parallel} decrease with increasing ζ^* (Fig. 3.4c). It improves the inconsistent dependence of \tilde{C}_{\parallel} on the ζ_c or ζ_χ between the front-right and front-left sectors of storms (Fig. 3.4a, b, d and e). The effect of $\cos(\psi)$ may be regarded as either the adjustment of wind forcing on the direction of surface waves for wave growth (Phillips 1957; Miles 1960; Donelan et al. 2012), or the extended fetch effect (Young 2003; Sullivan et al. 2012).

We now parameterize all realizations of \tilde{C}_{\parallel} and ϕ in the front-right and front-left sectors of storms as a function of ζ^* (black lines in Fig. 3.4c and f), respectively. i.e.,

$$\tilde{C}_{\parallel} \times 1000 = \begin{cases} a_{\parallel} \left(\frac{\zeta^*}{1000}\right)^2 + b_{\parallel} \left(\frac{\zeta^*}{1000}\right) + c_{\parallel}; & \text{for } \frac{\zeta^*}{1000} = 6 - 9 \\ 2.7 & ; \text{for } \frac{\zeta^*}{1000} = 9 - 21 \end{cases} \quad (3.1)$$

$$\phi(^{\circ}) = \begin{cases} a_{\phi} \left(\frac{\zeta^*}{1000}\right)^2 + b_{\phi} \left(\frac{\zeta^*}{1000}\right) + c_{\phi}; & \text{for } \frac{\zeta^*}{1000} = 6 - 12 \\ 0 & ; \text{for } \frac{\zeta^*}{1000} = 12 - 21 \end{cases} \quad (3.2)$$

The mean and standard deviation of the coefficients are $a_{\parallel} = (-5.2 \pm 0.2) \times 10^{-3}$, $b_{\parallel} = (3.8 \pm 5.5) \times 10^{-3}$, $c_{\parallel} = 3.05 \pm 0.03$, $a_{\phi} = 0.44 \pm 0.01$, $b_{\phi} = -9.70 \pm 0.19$ and $c_{\phi} = 52.45 \pm 0.16$. The RMS of $\tilde{C}_{\parallel}(\zeta^*)$ and $\phi(\zeta^*)$ are about 0.35×10^{-3} and 14° , respectively. The scattering of ϕ implies that ζ^* may not be the only factor in the generation of crosswind surface wind stress.

3.7 Discussion: Parameter ζ^*

Young (2003) discusses the importance to wave growth of the time that surface waves remain in the intense wind region. We therefore define a ‘motion-forced’ frequency f_r for surface waves when their group velocity c_g equals the storm translation speed U_h . For deep-water surface waves, $f_r = g/(4\pi c_g) = g/(4\pi U_h)$. These waves are forced continuously by the wind under a moving tropical cyclone. Because the f_r is inversely proportional to U_h , i.e., $U_h \propto f_r^{-1}$, faster tropical cyclones (larger U_h) force more efficiently on surface waves of a faster group velocity, i.e., lower frequency waves. The difference between c_g and U_h determines the time of wind forcing on surface waves in moving tropical cyclones (Young and Vinoth 2013).

Because of the local equilibrium between the wind input and energy dissipation, the fetch of fetch-limited surface waves χ is inversely proportional to peak frequency f_p , i.e., $\chi \propto f_p^{-1}$, under the constant wind speed (Fontaine 2013). Therefore, the duration $T = \chi/U_h \propto f_r/f_p$. The

ratio of f_r to f_p under Gustav, Ike, and Fanapi is all greater than 1 (Appendix E). Faster storms (e.g., Gustav) have the value of f_r/f_p closer to 1 than the slower storms (e.g., Fanapi) (Table 3.1). Assuming a mono-modal surface wave spectrum under tropical cyclones (Young 1998; Hu and Chen 2011) as a reference (Fig. 3.5), e.g., the JONSWAP spectrum (Hasselmann et al. 1973), lower f_r/f_p may imply higher wave energy S_η at f_r if $f_r/f_p > 1$. Because faster storms have the ratio of f_r/f_p closer to 1, surface waves containing higher energy may be forced continuously by the wind of faster storms. The continuous forcing of $|\mathbf{U}_{10}|$ at f_r may lead to the efficient increase of wave energy at the spectral level $S_\eta(f_r)$ (as the red shaded region in Fig. 3.5), and then result in wave breaking when the ratio of the wave height to the wavelength at f_r exceeds 0.1 (Donelan et al. 2012). The dissipation of wave energy into the ocean current via wave breaking is proportional to the spectral level $S_\eta(f_r)$ (e.g., Tolman and Chalikov 1996; Donelan et al. 2012). Stronger wave breaking may therefore occur under faster storms. The parameter T introduces a new concept to wave energy dissipation under a tropical cyclone moving at a speed of U_h . We compute T using the parametric model $\chi(r, \theta)$ as $T = \chi/U_h$. The correlation coefficient between T and the estimates of f_r/f_p under Gustav, Ike, and Fanapi is ~ 0.6 at $|\mathbf{U}_{10}| = 25 - 40 \text{ m s}^{-1}$ (Appendix E).

This study uses the non-dimensional effective wind duration $\zeta^* = gT/|\mathbf{U}_{10}|\cos(\psi)$ to study the variability of drag coefficients. The ζ^* is parameterized by the T , which may be regarded as an indicator of wave energy dissipation forced by moving tropical cyclones. The wind forcing on the direction of dominant surface waves $|\mathbf{U}_{10}|\cos(\psi)$ in the ζ^* may be associated with the wind energy input. According to the dependence of \tilde{C}_{\parallel} on the ζ^* in the front-right sector of storms (Fig. 3.4c), faster storms may force more efficiently on surface waves with larger amplitude, and result in stronger wave breaking, i.e., more wave momentum transfer into the ocean current. The

breaking wave energy under faster storms may therefore lead to higher drag coefficients than under slower storms. The lower $\tilde{C}_{\parallel}(\zeta^*)$ in the front-left sector of storms than in the front-right sector may be due to a greater angle of ψ , and thereby less wind energy input to induce wave breaking. Because the process of wave breaking is important to the momentum transferred efficiency (Jones and Toba 2012), i.e., the drag coefficients, the ζ^* may be used as a predictor of wave breaking under tropical cyclones in the future. The parameter $\zeta^* \propto f_r/(f_p|\mathbf{U}_{10}|\cos(\psi))$ may broaden the concept of waveage $c_p/|\mathbf{U}_{10}| \propto 1/(f_p|\mathbf{U}_{10}|)$ (Table 1.1), which focuses only on the relative speed between wind and surface waves, where c_p is the phase speed at f_p .

In short, the U_h of tropical cyclones may alter the surface wind stress $\boldsymbol{\tau}$ by affecting not only the time for surface waves staying in the moving tropical cyclone, but the wind forcing on the dominant surface waves. Note that the U_h also affects the maximum cooling induced by tropical cyclones (Price et al. 1994; Balaguru et al. 2015). The forecast of tropical cyclone motion is therefore important to the prediction of storm-induced ocean momentum and thermal response, and thereby maximum potential intensity of tropical cyclones (Emanuel 1995; Fig. 1.1). We summarize several potential parameters that might be important to drag coefficients in Table 3.3, and encourage further investigations, especially the parameterization of ϕ .

3.8 Summary

Nineteen EM-APEX were deployed from aircraft in five different tropical cyclones: Frances, Gustav, Ike, Fanapi, and Megi, to measure profiles of ocean current velocity, temperature, and salinity. The surface wind stress $\tilde{\boldsymbol{\tau}}$ is estimated by depth-integrating the estimated wind-driven current in the linear momentum budget. The biases due to the linear momentum assumption are corrected using results of PWP3D model simulations. The adjusted

drag coefficients are computed using the estimates of corrected $\tilde{\tau}$ in the front-right and front-left sectors of tropical cyclones.

At $|\mathbf{U}_{10}| = 25\text{--}40 \text{ m s}^{-1}$, the adjusted downwind drag coefficient \tilde{C}_{\parallel} in the front-right sector of tropical cyclones, $1.1\text{--}3.1 \times 10^{-3}$, is mostly higher than that in the front-left sector of Gustav and Fanapi, 0.8×10^{-3} and 1.7×10^{-3} , respectively. The peak \tilde{C}_{\parallel} is found at $|\mathbf{U}_{10}| = 30\text{--}40 \text{ m s}^{-1}$. The \tilde{C}_{\parallel} in Fanapi and Megi is saturated at $|\mathbf{U}_{10}| > 40 \text{ m s}^{-1}$, $\sim 1.6 \times 10^{-3}$, in good agreement with the C_d reported by Powell et al. (2003). The angle ϕ in the front-right sector of tropical cyclones is $-15\text{--}40^\circ$ at $|\mathbf{U}_{10}| = 25\text{--}30 \text{ m s}^{-1}$, and the scatter of ϕ decreases with increasing $|\mathbf{U}_{10}|$.

The estimates of drag coefficients are parameterized for the first time as a function of the non-dimensional effective wind duration ζ^* . The parameter ζ^* includes the wind forcing, storm translation speed, and fetch. Parameterization based on these factors fits the variations in the \tilde{C}_{\parallel} of $0.8\text{--}3.1 \times 10^{-3}$ to a RMS of 0.35×10^{-3} , and the variations in the angle ϕ between \mathbf{U}_{10} and surface wind stress $\boldsymbol{\tau}$ of $-15\text{--}40^\circ$ to a RMS of 14° , at $|\mathbf{U}_{10}| = 25\text{--}40 \text{ m s}^{-1}$. The \tilde{C}_{\parallel} in the front-right sector of tropical cyclones decreases with slower U_h , presumably due to less breaking wave energy under slower storms. The \tilde{C}_{\parallel} in the front-left sector of tropical cyclones is lower than in the front-right sector, presumably due to a greater angle between the wind and waves.

This chapter presents a new data-based parameterization of drag coefficients at $|\mathbf{U}_{10}| = 25\text{--}40 \text{ m s}^{-1}$ by using the properties of surface waves and wind forcing of moving tropical cyclones. The dependence of drag coefficients on surface waves emphasizes the importance of tropical cyclone–wave–ocean interactions, in good agreement with the previous model studies (e.g., Chen et al. 2013; Reichl et al. 2014). These results are important and useful to guide future model studies on the oceanic thermal and momentum responses to tropical cyclones, especially the maximum cooling on the right side of tropical cyclone tracks.

EM-APEX float	Y (km)	MLD (m)	$ \mathbf{v} $ in MLD (m s^{-1})	Max $ \mathbf{U}_{10} $ (m s^{-1})	Tropical Cyclone ($R_{\text{max}}, V_{\text{max}}, U_h$)
em1633a	59	73	1.14	35	Frances (30, 56, 6.2)
em1636a	5	58	0.82	46	
em3763a	55	30	1.51	36	Gustav (46, 46, 7.7)
em3766a	-34	26	0.44	30	
em3766a	74	58	1.06	34	Ike (75, 41, 5.3)
em4912a	92	76	0.79	30	Fanapi (20, 52, 3.8)
em4907a	38	75	1.17	35	
em4910a	1	52	0.97	44	
em4906a	-35	62	0.43	38	
em3766c	72	63	0.97	29	Megi (14, 76, 7.8)
em4913a	41	71	0.85	37	
em3763c	7	77	0.78	62	

Table. 3.1. The oceanic properties measured by twelve EM-APEX floats at $|\mathbf{U}_{10}| > 25 \text{ m s}^{-1}$, and tropical cyclone properties as storm eyes passed float positions. The distance of floats' positions to the tracks Y (km) is positive to the right side. The mixed layer depth (MLD) is computed using the temperature and salinity profiles measured by the CTD mounted on the floats. The horizontal ocean current speed $|\mathbf{v}|$ in the MLD (m s^{-1}) is averaged using the profiles of velocity measured by the floats. The wind speed at 10-m height above the sea surface $|\mathbf{U}_{10}|$ at the floats' positions is interpolated linearly using the processed wind maps (Appendix A). The units of tropical cyclone properties: radius of maximum wind speed R_{max} , maximum wind speed V_{max} , and translation speed U_h , are km, m s^{-1} , and m s^{-1} , respectively.

Sector	Storms		Adjusted Drag Coefficients			Apparent Drag Coefficients		
			U ₁₀ (m s ⁻¹)			U ₁₀ (m s ⁻¹)		
			27.5±2.5	35±5	> 40	27.5±2.5	35±5	> 40
Front-Right	Frances	C _∥ ×1000	2.83±0.29	2.84±0.21	N/A	2.79±0.27	2.98±0.21	N/A
		ϕ (°)	25±5	14±3	N/A	29±5	22±3	N/A
	Gustav	C _∥ ×1000	2.34±0.31	2.18±0.19	N/A	2.28±0.30	2.30±0.20	N/A
		ϕ (°)	-12±5	-9±4	N/A	-7±4	0±4	N/A
	Ike	C _∥ ×1000	2.05±0.27	2.56±0.20	N/A	2.57±0.26	2.66±0.26	N/A
		ϕ (°)	18±5	0±3	N/A	28±4	19±4	N/A
	Fanapi	C _∥ ×1000	1.13±0.26	2.37±0.17	1.63±0.33	1.17±0.25	2.30±0.17	1.65±0.36
		ϕ (°)	42±10	2±4	6±12	45±10	5±4	2±12
	Megi	C _∥ ×1000	2.98±0.44	3.13±0.44	1.67±0.32	3.11±0.45	3.48±0.46	2.41±0.32
		ϕ (°)	-2±7	11±6	11±8	9±7	22±5	22±5
Front-Left	Gustav	C _∥ ×1000	0.77±0.13	N/A	N/A	0.74±0.13	N/A	N/A
		ϕ (°)	42±8	N/A	N/A	52±7	N/A	N/A
	Fanapi	C _∥ ×1000	1.69±0.46	1.4±0.21	N/A	2.00±0.43	1.60±0.24	N/A
		ϕ (°)	-9±13	-12±9	N/A	-2±12	-11±7	N/A

Table. 3.2. The mean and standard deviation of adjusted and apparent downwind drag coefficients, and the angle ϕ of drag $\tilde{\tau}$ clockwise from \mathbf{U}_{10} , in the front-right and front-left sectors of five tropical cyclones.

Sector	Storms	Parameters	U ₁₀ (m s ⁻¹)		
			27.5±2.5	35±5	> 40
Front-Right	Frances	r (km)	85±11	56±16	N/A
		θ (°)	30±21	46±36	N/A
		χ (km)	161±29	140±24	N/A
		θ _w (°)	-118±21	-133±36	N/A
	Gustav	r (km)	114±15	69±12	N/A
		θ (°)	30±5	58±14	N/A
		χ (km)	196±7	167±10	N/A
		θ _w (°)	-145±5	-171±13	N/A
	Ike	r (km)	124±18	84±7	N/A
		θ (°)	40±7	65±9	N/A
		χ (km)	205±16	173±7	N/A
		θ _w (°)	-135±4	-147±7	N/A
	Fanapi	r (km)	102±13	57±18	23±5
		θ (°)	40±29	32±29	-0±1
		χ (km)	166±28	140±24	103±2
		θ _w (°)	-120±24	-111±27	-84±0
Megi	r (km)	88±14	51±11	16±10	
	θ (°)	41±26	45±30	-51±48	
	χ (km)	166±24	145±21	121±5	
	θ _w (°)	-114±24	-111±28	-123±52	
Front-Left	Gustav	r (km)	81±13	N/A	N/A
		θ (°)	-26±4	N/A	N/A
		χ (km)	111±3	N/A	N/A
		θ _w (°)	-88±7	N/A	N/A
	Fanapi	r (km)	95±9	55±15	N/A
		θ (°)	-24±2	-49±23	N/A
		χ (km)	110±2	108±15	N/A
		θ _w (°)	-64±3	-38±20	N/A

Table. 3.3. The mean and standard deviation of drag coefficient estimates at the distance of floats to tropical cyclones' eyes r , azimuth θ of float positions clockwise from the motion of tropical cyclones (see Fig. 3.2c), the fetch length $\chi(r,\theta)$ using the parametric model in Hwang et al. (2016), and the orientation of wind θ_w .

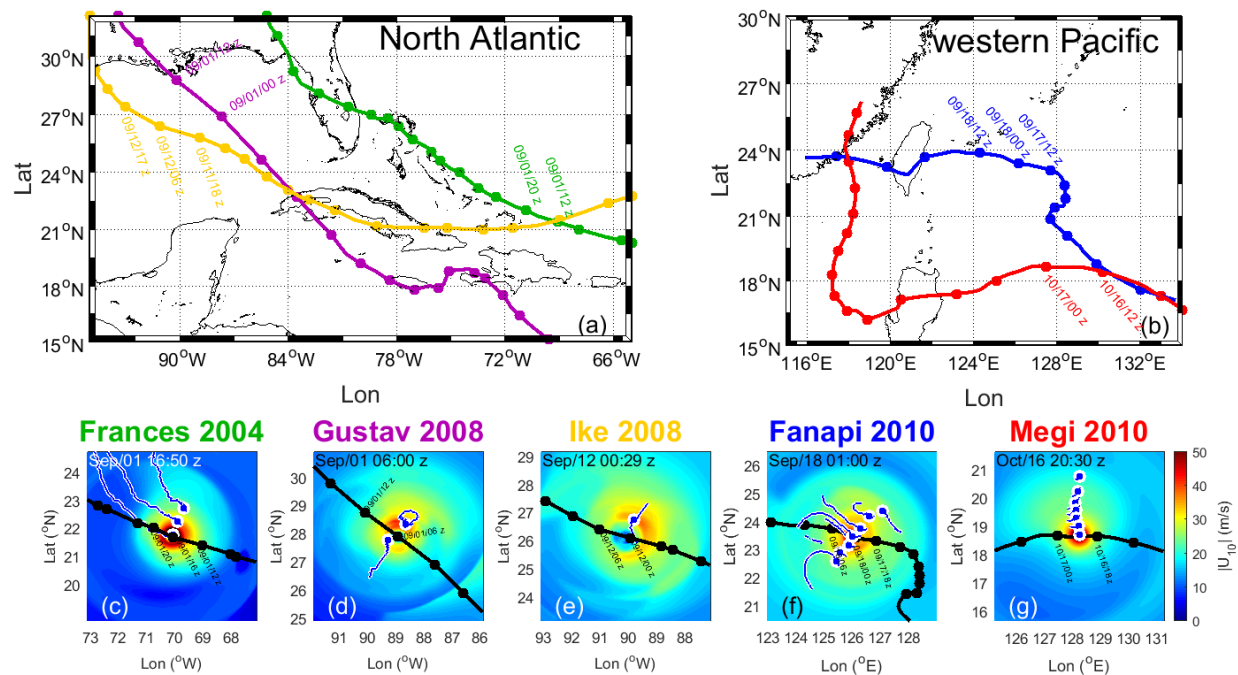


Fig. 3.1. The tracks of hurricanes in the North Atlantic (a), Frances: green; Gustav: purple; Ike: gold. The tracks of typhoons in the western Pacific (b), Fanapi: blue; Megi: red. Tropical cyclone wind maps at the time eyes pass near EM-APEX float positions (c–g) and trajectories of float positions (blue dots connected with lines in c–g). The colored dots connected with thick lines in (a) and (b) are tracks of tropical cyclone eyes every 12 h, and the black dots connected with a thick line in (c)–(g) are tracks of tropical cyclone eyes every 6 h.

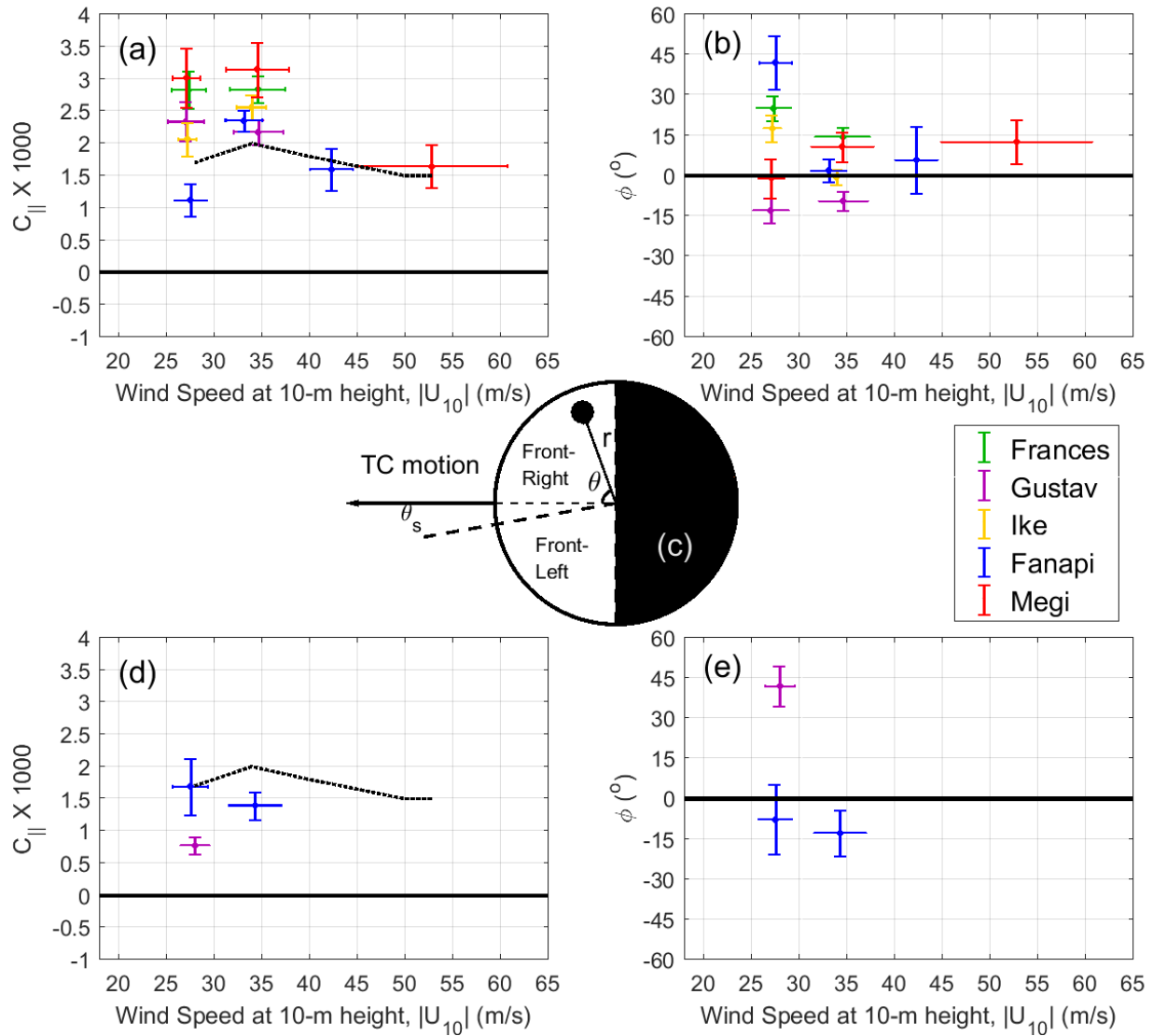


Fig. 3.2. Estimates of adjusted downwind drag coefficient $\tilde{C}_{||}$ (a and d) and the angle ϕ (b and e) between the surface wind stress $\tilde{\tau}$ and wind \mathbf{U}_{10} in five different tropical cyclones (colored lines as in Fig. 3.1), using the float measurements in the front-right (a and b) and front-left (d and e) sectors of tropical cyclones (c). The vertical error bars represent the standard deviations of $\tilde{C}_{||}$ averages and ϕ , respectively, and the horizontal error bars represent the standard deviations of interpolated $|\mathbf{U}_{10}|$ at the float positions. The boundary between two sectors is defined assuming $\theta_s = -10^\circ$. For the positions of the floats, the azimuth $\theta > 0$ is clockwise from tropical cyclones'

(TC) motion, and r the distance of floats to the tropical cyclone's eye. Black dashed lines are results using the Powell et al. (2003) drag coefficient.

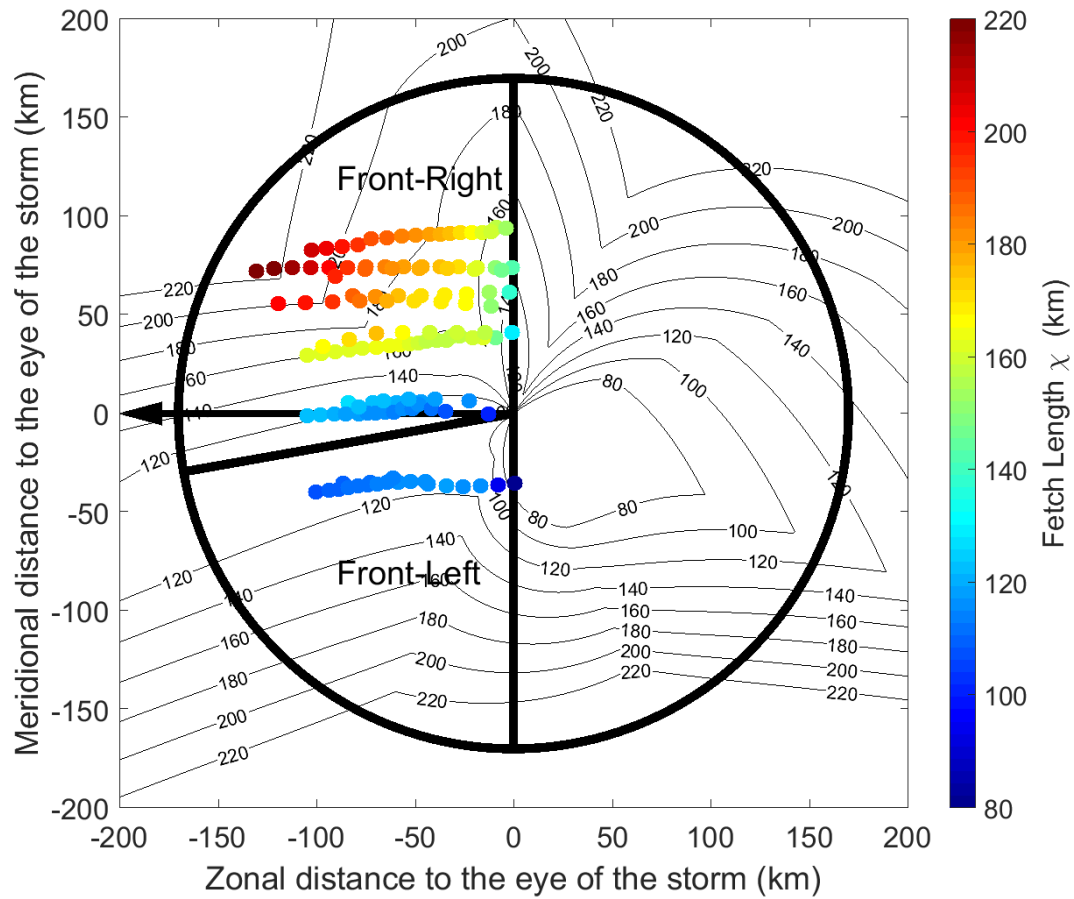


Fig. 3.3. Fetch length χ at the float positions (color shading) relative to tropical cyclone eye positions computed using the parametric model of $\chi(r,\theta)$ of fetch-limited surface waves (black contour lines) in Hwang et al. (2016). The black arrow is the motion of the storm. See Fig. 3.2c for the definition of sectors under tropical cyclones.

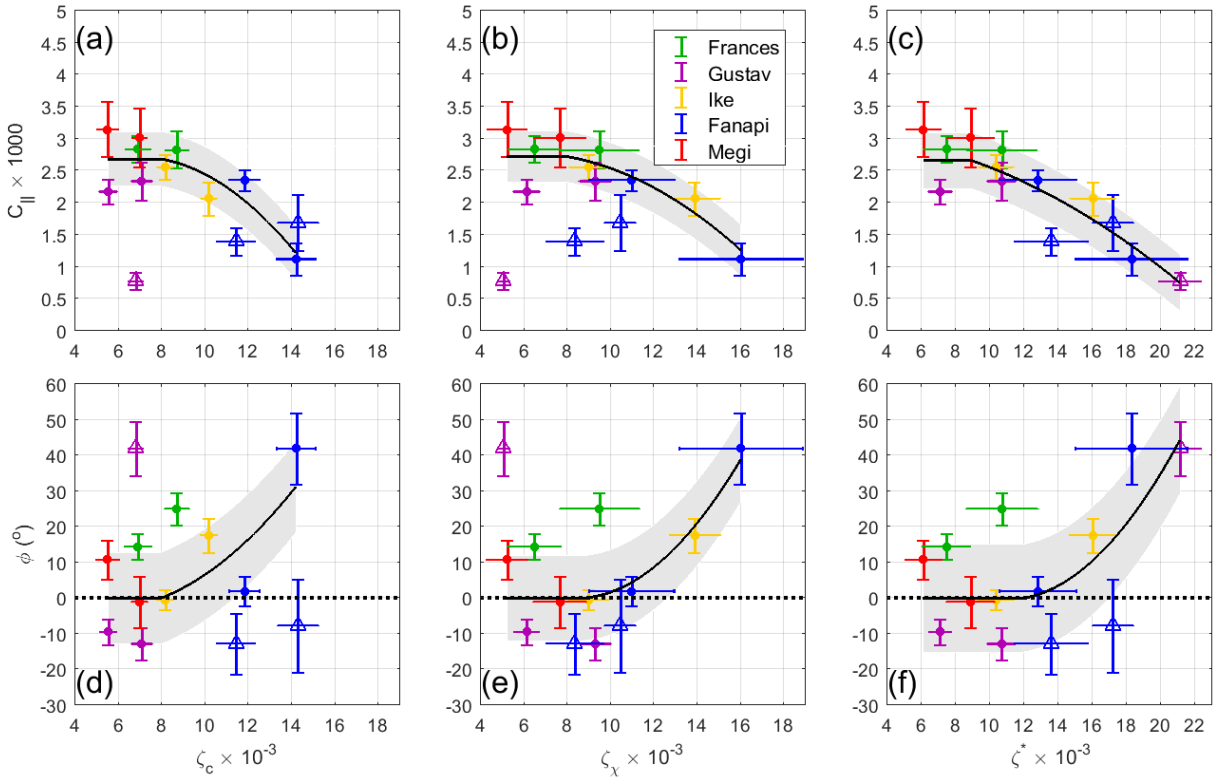


Fig. 3.4. Dependence of adjusted downwind drag coefficient \tilde{C}_{\parallel} (a–c) and the angle ϕ between the surface wind stress $\tilde{\tau}$ and wind \mathbf{U}_{10} (d–f) under five tropical cyclones (colored lines as in Fig. 3.1) at $|\mathbf{U}_{10}| = 25\text{--}40 \text{ m s}^{-1}$ (front-right sector: dots; front-left sector: triangles) on nondimensional wind duration ζ_c assuming the constant fetch (a and d), ζ_{χ} assuming the parametric model $\chi(r, \theta)$ in Hwang et al. (2016) (b and e), and nondimensional effective wind duration ζ^* (c and f), respectively. The black lines in (a and b) and (d and e) are the fitted parameterizations of \tilde{C}_{\parallel} and ϕ using the estimates in the front-right sector of tropical cyclones, and in (c) and (f) are the $\tilde{C}_{\parallel}(\zeta^*)$ and $\phi(\zeta^*)$ using the all estimates. The bounds of grey area from the black lines are the standard errors between individual drag coefficient estimates and cubic-fitted curves. See Fig. 3.2 for the descriptions of vertical error bars. Horizontal error bars represent one standard deviation of ζ .

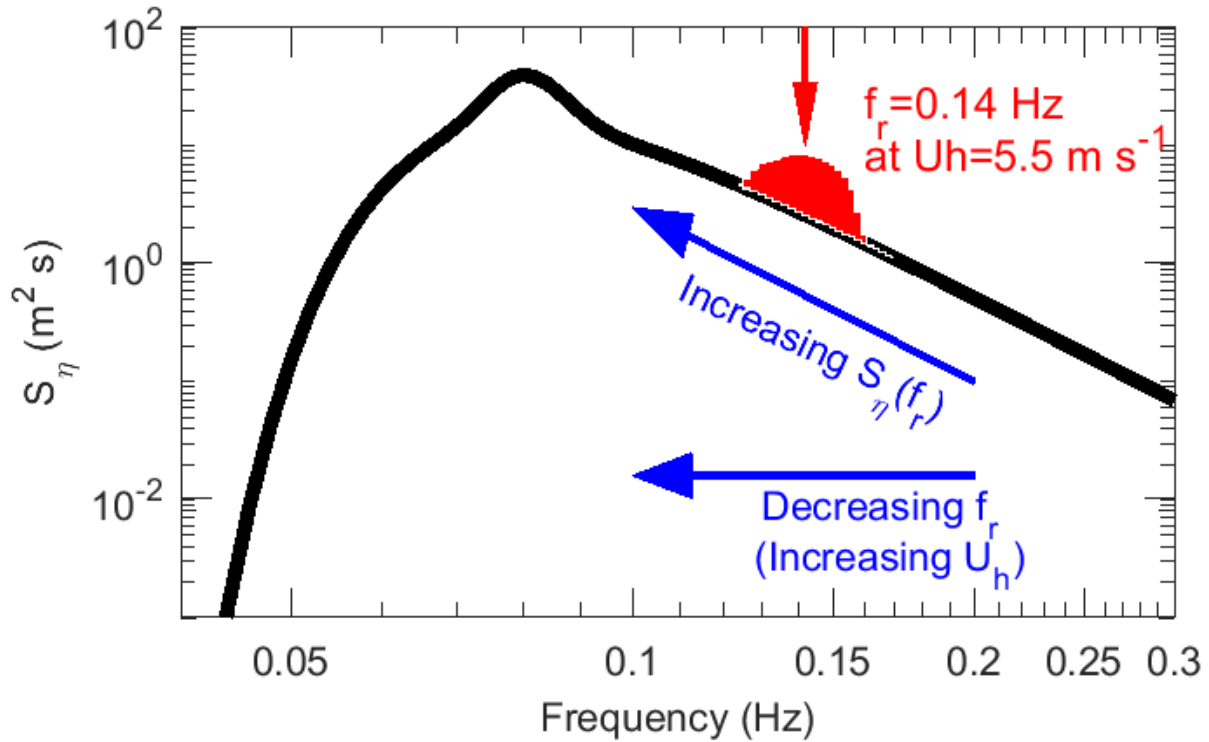


Fig. 3.5. An illustration of surface wave energy $S_\eta(f_r)$ at the motion-forced frequency f_r . The black line is the empirical JONSWAP spectrum with the peak frequency $f_p = 0.08$ Hz. Assuming a tropical cyclone moving at the translation speed $U_h = 5.5$ m s⁻¹, the tropical cyclone wind may resonate with the surface waves at the $f_r \approx 0.14$ Hz (red arrow), and enhance the spectral level at the f_r (red area). Surface waves at lower f_r containing higher wave energy $S_\eta(f_r)$ will be forced continuously by faster tropical cyclones if $f_r/f_p > 1$.

Chapter 4. Estimates of Surface Waves Using Subsurface EM-APEX floats under Typhoon Fanapi 2010

Seven subsurface EM-APEX floats measured the voltage induced by the motional induction of seawater under Typhoon Fanapi 2010. Measurements were processed to estimate high-frequency (> 0.02 Hz) oceanic velocity variance $\widetilde{\sigma}_u^2(z)$ associated with surface gravity waves. Surface wave peak frequency f_p and significant wave height H_s are estimated by nonlinear least-squared fit to $\widetilde{\sigma}_u^2$, assuming a broadband JONSWAP surface wave spectrum. The H_s is further corrected for the effects of float rotation, Earth's geomagnetic field inclination, and surface wave propagation direction. The f_p is 0.08 – 0.10 Hz, with the maximum f_p of 0.10 Hz in the rear-left quadrant of Fanapi, which is ~ 0.02 Hz higher than in the rear-right quadrant. The H_s is 6 – 12 m with the maximum in the rear sector of Fanapi. Comparing our estimated f_p and H_s with those assuming a single dominant surface wave yields differences of more than 0.02 Hz and 4 m, respectively. The surface waves under Fanapi simulated in the WAVEWATCH III (ww3) model are used to assess and compare to float estimates. Differences in the surface wave spectra of JONSWAP and ww3 yields uncertainties of $< 5\%$ outside Fanapi's eyewall, and $> 10\%$ within the eyewall. The estimated f_p is 10% less than simulated f_p^{ww3} before the passage of Fanapi's eye, and 20% less after eye passage. Most differences between H_s and simulated H_s^{ww3} are < 2 m, except those in the rear-left quadrant of Fanapi, which are ~ 5 m. Improving ww3 surface wave simulations is important to future studies of tropical cyclone–wave–ocean interactions.

4.1 Introduction of Surface Wave Measurements

Surface waves carried by the storm surges of tropical cyclones are disasters for coastlines. Surface waves also change the roughness of the ocean, altering the surface wind stress under tropical cyclones (Moon et al. 2004; Chen et al. 2013). The wave-dependent surface wind stress extracts the tropical cyclone's momentum to force ocean current (Emanuel 1995). The induced ocean current then leads to shear instability, vertical mixing, and cooling in the upper ocean (Price et al. 1994), thereby lessening heat available for cyclone intensification (Lin et al. 2013). Measuring surface waves under tropical cyclones is important for improving the parameterizations of surface wind stress in the forecast of tropical cyclone intensification (Fan et al. 2009).

The most often used platforms to measure surface waves include wave sensors mounted on drifting buoys (e.g., Herbers et al. 2012), sensors mounted on buoys connected to moorings (e.g., Mitsuyasu et al. 1975; Steele et al. 1992; Young 1998; Graber et al. 2000; Dietrich et al. 2011; Drennan et al. 2014), satellite altimeters (e.g., Envisat-1 and ERS-2 in Fan et al. 2009), radar altimeters mounted on aircraft or ships (e.g., Hwang et al. 1999; Walsh et al. 2002; Wright et al. 2001; Black et al. 2007; Magnusson and Donelan 2013), and Doppler sonar radar mounted on towers in shallow water or on coastlines (e.g., Pinkel and Smith 1987; Reichert et al. 1999; Lin et al. 2002). Deploying buoys to measure surface waves after tropical cyclone formation is risky, when possible (Collins III et al. 2014). Most tropical cyclones do not pass buoys deployed in the open ocean. Recently, however, moored buoy measurements were taken as Typhoon Nepartak's eye passed (Jan et al. 2017). Wave sensors and wire cables mounted on buoys may be damaged by strong tropical cyclone winds (e.g., $> 25 \text{ m s}^{-1}$) and turbulence at the sea surface (Collins III et al. 2014). Scanning radar altimeters (SRA) mounted on aircraft have been used to

study surface waves under tropical cyclones by remote sensing of ocean surface displacements (e.g., Wright et al. 2001; Black et al. 2007; Fan et al. 2009). Unfortunately, SRA backscattered signals are vulnerable to the contamination by sea foam, spray, and bubbles (Magnusson and Donelan 2013), which are ubiquitous in strong tropical cyclone wind environments (Black et al. 2007).

When seawater is moved by ocean currents and surface gravity waves through the Earth's geomagnetic field, an electric field is induced (Longuet-Higgins et al. 1954; Weaver 1965; Sanford 1971; Podney 1975), producing electric current in the ocean (Cox et al. 1978). The temporal variations of wave-induced electric current in the ocean will further generate an electromagnetic field according to Ampere's law (Watermann and Mangunia 1997; Lilley et al. 2004). Sanford et al. (2011) measured the high-frequency velocity variance (> 0.02 Hz) associated with the motional induction of surface waves using EM-APEX floats under Hurricane Frances 2004. These subsurface floats were air-launched (e.g., Sanford et al. 2011; Hsu et al. 2017) from C-130 aircraft about 1 day before the passage of the tropical cyclone's eye, and took measurements of temperature, salinity, current velocity, and high-frequency velocity variance under strong tropical cyclone winds (e.g., > 25 m s⁻¹). They estimated significant wave height and mean wave period, assuming a single dominant surface wave under the hurricane. This study aims to provide an improved method for estimating surface waves using EM-APEX float measurements by assuming a broadband surface wave spectrum. Uncertainties in the surface wave estimates are assessed.

Seven EM-APEX floats were launched from a C-130 aircraft (Mrvaljevic et al. 2013; Fig. 4.1) starting at 01:00 UTC 17 September 2010 in Typhoon Fanapi (Table 4.1), along 126.1°E between 22.6°N and 24.4°N, with a horizontal separation of ~25 km. Details of measurements

taken under Typhoon Fanapi during the Impact of Typhoons on the Ocean in the Pacific (ITOP) project are described in D'Asaro et al. (2014). Section 4.2 describes EM-APEX float measurements. The theory of the motional induction by surface wave velocity and ocean currents is discussed in section 4.3. Methods to estimate surface wave velocity variance from float measurements, and surface wave properties at the float positions assuming the empirical JONSWAP spectrum (Hasselmann et al. 1973; Appendix D.2) are presented in section 4.4. In section 4.5, we estimate surface waves under Fanapi using two methods — one assuming the JONSWAP spectrum and one assuming a single dominant surface wave (Sanford et al. 2011). An oceanic surface wave model WAVEWATCH III (ww3) is used to simulate the surface wave field under Typhoon Fanapi. The ww3 model outputs are compared with the float estimates of surface waves in section 4.6. The model is used to study uncertainties in our surface wave estimates in section 4.7. Section 4.8 will summarize the methodology and results.

4.2 EM-APEX Float Measurements of Velocity Variance

EM-APEX floats measure the voltage using two pairs of Ag-AgCl electrodes (Fig. 4.2), E_1 and E_2 pairs, mounted on orthogonal axes (Sanford et al. 2005). The sampling rate of voltage is 1 Hz. As the floats profile vertically, they rotate by an array of slanted blades mounted on the float. The rotation frequency is about 0.08 Hz when floats ascend, and 0.12 Hz when floats descend. Oceanic horizontal currents are estimated by least-squared fitting every 50 s of float voltage measurements (Sanford et al. 1978), with the moving window of 25 s, i.e., the raw voltage data size is 25 times larger than the processed current velocity. The residuals in the least-squared fitting are often used to compute the output of Verr in the float measurements. We compute the high-frequency (> 0.02 Hz) velocity variance $\widetilde{\sigma}_u^2$ using the Verr (Appendix C.2.4).

The $\widetilde{\sigma}_u^2$ is the sum of the horizontal velocity variance of high-frequency (>0.02 Hz) surface waves plus measurement errors (details in section 4.4), and is previously used for estimating surface waves in Sanford et al. (2011). Float GPS positions and measurements of salinity, temperature, horizontal current velocity, and $\widetilde{\sigma}_u^2$ are transmitted via Iridium satellite communications when floats surface. The amount of raw voltage data was too large to be transmitted due to the slow transmission speed, and cannot be used for further analysis unless the floats are recovered by ships.

Four EM-APEX floats measured velocity variances at wind speeds > 25 m s⁻¹ under Typhoon Fanapi (magenta dots in Fig. 4.1). The $\widetilde{\sigma}_u^2$ decayed ‘exponentially’ with depth (Fig. 4.3e–h), in agreement with the report by Sanford et al. (2011). Air pump tubing inside the floats used to inflate air bags was broken due to strong Fanapi downwelling winds, resulting in the floats descending from the sea surface slower than usual in the first several minutes, and thereby lengthening the rotation period for measuring voltage. Voltage measured by the electrodes with a rotation period > 25 s was excluded from the data processing (Sanford et al. 2005), so 38% of profiles of $\widetilde{\sigma}_u^2$ have no measurements in the upper 20 m. The $\widetilde{\sigma}_u^2$ is used to estimate surface wave properties in this study (section 4.5).

4.3 Theory of Seawater Motion-induced Electric Current

4.3.1 *Electric current in a moving medium*

Sanford (1971) reports on the motional induction of oceanic current modulated by the electromagnetic field \mathbf{b} in the Earth’s geomagnetic field (Appendix C.1.1). Because the temporal variations of \mathbf{b} and the motional induction of ocean current in the \mathbf{b} affect the electric field

insignificantly, the electric current induced by a low-frequency ocean current is mainly driven by the motional induction resulting from the ocean current \mathbf{V} crossing the Earth's geomagnetic field \mathbf{F} (Longuet-Higgins et al. 1954), and the background electric field $-\nabla\Phi$. i.e.,

$$\frac{\mathbf{J}}{\sigma} \approx -\nabla\Phi + \mathbf{V} \times \mathbf{F} \quad (4.1)$$

where $\mathbf{J} = J_x \hat{\mathbf{i}} + J_y \hat{\mathbf{j}} + J_z \hat{\mathbf{k}}$, $\mathbf{V} = u \hat{\mathbf{i}} + v \hat{\mathbf{j}} + w \hat{\mathbf{k}}$, and $\mathbf{F} = F_y \hat{\mathbf{j}} + F_z \hat{\mathbf{k}}$ (Table. 4.1). Eq. (4.1) can also be applied to the electric current induced by a surface wave, because the electromagnetic field induced by surface waves affects the electric field negligibly (Appendix C.1.2; Weaver 1965).

4.3.2 Electric current induced by a surface wave and low-frequency current in the upper ocean

Sanford et al. (1978) describes that the electric current induced by a low-frequency ocean current $\mathbf{v} = u\hat{\mathbf{i}} + v\hat{\mathbf{j}}$ (Eq. C.10 in Appendix C.1.3), assuming the horizontal scale of the ocean current much greater than its vertical scale. If the surface wave velocity \mathbf{V}_{sgw} (Eq. C.11) is assumed to induce the electric current \mathbf{J}' the same as the low-frequency current (the superscript ' represents the wave-induced component), then \mathbf{J}' can be expressed as

$$\mathbf{J}'/\sigma \approx \sqrt{2}\sigma_{u0}F_z \sin \psi (\sin \theta \hat{\mathbf{i}} - \cos \theta \hat{\mathbf{j}})e^{kz} + \left(\left(\frac{J_x}{\sigma} \right)^* \hat{\mathbf{i}} + \left(\frac{J_y}{\sigma} \right)^* \hat{\mathbf{j}} \right) \quad (4.2)$$

where $\psi = k_x x + k_y y - \omega t + \phi_0$, $\theta = \tan^{-1} \frac{k_y}{k_x}$, and $k = (k_x^2 + k_y^2)^{\frac{1}{2}}$ (Table. 4.1). The \mathbf{J}' is affected by the surface wave velocity amplitude ($\sigma_{u0}e^{kz}$) at different depths, where σ_{u0}^2 is the variance of horizontal velocity of surface waves at the sea surface.

We assume the locally uniform conductivity σ in the upper ocean, $\nabla(1/\sigma) = 0$, the conservation of electric current \mathbf{J} , $\nabla \cdot \mathbf{J} = 0$, the boundary condition $J_z \approx 0$ at the ocean surface $z = 0$

(Eq. C.13; Longuet-Higgins et al. 1954), and the boundary condition $\Phi \approx 0$ at $z = -\infty$ (Eq. C.14).

Using the above assumptions and boundary conditions in Eq. (4.1), the electric current $\mathbf{J}' =$

$J'_x \hat{\mathbf{i}} + J'_y \hat{\mathbf{j}}$ induced by a single surface wave in the deep ocean is (Eq. C.17 in Appendix C.1.4)

$$\mathbf{J}'/\sigma = \sqrt{2}\sigma_{u0}F_z\sqrt{1+\beta^2}\sin\psi_\omega(\sin\theta\hat{\mathbf{i}} - \cos\theta\hat{\mathbf{j}})e^{kz} \quad (4.3)$$

where $\psi_\omega = \psi + \tan^{-1}(\beta)$ and the geomagnetic field inclination effect $\beta = \frac{F_y}{F_z}\sin\theta$. Compared

with Eq. (4.2), the amplitude and phase of \mathbf{J}' are modified for the geomagnetic field inclination

F_y/F_z and surface wave propagation direction θ .

Assuming the interaction between the low-frequency current and surface waves in the motional induction due to the electromagnetic field is negligible, the electric current $\mathbf{J} = J_x \hat{\mathbf{i}} + J_y \hat{\mathbf{j}}$ induced by a low-frequency current and a surface wave in the upper ocean is

$$\begin{cases} \frac{J_x}{\sigma} = \frac{J'_x}{\sigma} + \frac{\bar{J}_x}{\sigma} = \sqrt{2}\sigma_{u0}F_z\sqrt{1+\beta^2}\sin\psi_\omega\sin\theta e^{kz} + \frac{\bar{J}_x}{\sigma} \\ \frac{J_y}{\sigma} = \frac{J'_y}{\sigma} + \frac{\bar{J}_y}{\sigma} = -(\sqrt{2}\sigma_{u0}F_z\sqrt{1+\beta^2}\sin\psi_\omega\cos\theta e^{kz}) + \frac{\bar{J}_y}{\sigma} \end{cases} \quad (4.4)$$

4.4 Method to Estimate Surface Waves Using EM-APEX Float Measurements

4.4.1 Profiles of high-frequency velocity variance $\widetilde{\sigma}_u^2$ measured by floats

EM-APEX floats measure the voltage $\Delta\Phi$ associated with the electric field $-\nabla\Phi_{EM}$ around floats (Fig. 4.2), which is primarily from the electric current \mathbf{J} (Eq. 4.4) induced by the motional induction of seawater (Eq. C.20 in Appendix C.2.1). Voltage measurements taken by two pairs of rotating electrodes E_1 and E_2 (Appendix C.2.2), $\Delta\Phi_i$ ($i = 1$ for E_1 pair and $i = 2$ for E_2 pair), are least-squared fitted in 50-s data windows to demodulate the voltage associated with the low-frequency electric current $\bar{\mathbf{J}}$ (< 0.02 Hz) from the voltage measurement offset and trend (Appendix C.2.3; Sanford et al. 1978), because the offset and trend are much greater than $\bar{\mathbf{J}}$. The

residuals ϵ^i in the harmonic fit contain part of the voltage associated with the wave-induced electric current \mathbf{J}' (> 0.02 Hz), which are often used to compute the Verr on each pair of electrodes in the float measurements (Appendix C.2.4).

The Verr containing the voltage measurements with frequency 0.02–1 Hz (Appendix C.2.3) is used to provide the profiles of estimated velocity variance $\widetilde{\sigma}_u^2$ on the pair of electrodes E_i (Eqs. C.23 and 27 in Appendix C.2.4) as

$$\widetilde{\sigma}_u^2 \approx \frac{(1+\alpha)}{4} (1 + \beta^2) \sigma_{u0}^2 e^{2kz} + \delta_i^2; \text{ for } i = 1 \text{ or } 2 \quad (4.5)$$

where $\alpha = 2\langle \cos^2 \widetilde{\psi} \rangle - 2\langle \cos \widetilde{\psi} \rangle^2 - 2\langle \cos 2\psi_\Omega \rangle$ represents the rotational demodulation effect due to the difference between the surface wave angular frequency ω and the EM-APEX float angular rotation frequency Ω , $\widetilde{\psi} = -(\omega - \Omega)t + \widetilde{\phi}_0$, $\widetilde{\phi}_0 = k_x x + k_y y + \phi_0 + \phi_i + \tan^{-1}(\beta) - \theta$, $\psi_\Omega = \theta - \Omega t + \phi_i$, $\langle \rangle$ represents the average over the 50-s fitting window ($\Delta T = 50$), and δ_i^2 the instrumental noise on each pair of electrodes ($\delta_i = 0.8\text{--}1.5$ cm s⁻¹ in Hsu et al. 2017).

Estimated velocity variance may differ from the actual surface wave velocity variance ($\sigma_{u0}^2 e^{2kz}$) due to the rotational demodulation effect α and the geomagnetic field inclination effect β (Eq. 4.5), biasing surface wave estimates. The α is always less than 1 for surface waves and low-frequency current when the float rotation rate $\Omega \geq \Omega_c$, where $\Omega_c = 2\pi/\Delta T$ rad s⁻¹. Typically, float $\Omega \approx 4\Omega_c$ when ascending. The $2\langle \cos \widetilde{\psi} \rangle^2$ in the expression of α , associated with the mean of surface wave measurements on the rotating electrodes, is removed as the offset in the processing of voltage measurements (Eq. C.22), and may not be zero if $|\omega - \Omega|/2\pi < 1/50$ Hz. So, $\alpha = 0\text{--}1$. The F_y and F_z were about 36 and -24 μT under Typhoon Fanapi, respectively, according to the geomagnetic field data from the National Centers for Environmental Information (NCEI)/NOAA (Thébault et al. 2015), i.e., $\beta^2 \leq 2.25$.

In short, the α effect may underestimate the actual surface wave velocity variance by 50–75% ($\alpha = 0 - 1$), and the β effect may overestimate by > 2 times ($\beta^2 = 2.25$). Sanford et al. (2011) neglect the α and β effects when estimating surface waves, assuming a single dominant surface wave velocity variance as $\widetilde{\sigma}_u^2 = \sigma_{u0}^2 e^{2kz}$ (Table 4.1). In this study, we use the profiles of $\widetilde{\sigma}_u^2$ to estimate surface waves assuming a broadband surface wave spectrum, including corrections of the α and β effects (section 4.5.1). The results from two different approaches will be compared in section 4.5.2.

4.4.2 *Estimating surface waves from velocity variance profiles*

Surface wave spectra S_η under tropical cyclones have been reported previously (Ochi and Chiu 1982; Young 1998; Ochi 2003; Young 2003). Over 85% of surface waves under hurricanes have a single peak frequency spectrum (Hu and Chen 2011), similar to the empirical JONSWAP surface wave spectrum (Young 1998). The remaining 15% of surface waves have two frequency spectral peaks.

We assume that surface wave spectra under Typhoon Fanapi can be parameterized by the empirical JONSWAP spectrum form $S_\eta(f_p, S_p, \sigma_a, \sigma_b, \gamma)$ (Eq. D.3), where S_p is the peak spectrum level of S_η at the peak frequency f_p , and σ_a , σ_b , and γ the dimensionless shape parameters. This assumption is reliable to most wind-waves in the open ocean. We further assume constant shape parameters σ_a , σ_b , and γ so that $S_\eta = f(f_p, S_p)$. Modeled velocity variance $\widehat{\sigma}_u^2(S_\eta, z)$ of surface waves depends on only f_p and S_p (Appendix D.2.1), i.e.,

$$\widehat{\sigma}_u^2(S_\eta, z) = \widehat{\sigma}_u^2(f_p, S_p, z).$$

The parameters \widetilde{f}_p and \widetilde{S}_p are estimated by minimizing root mean-squared logarithmic error (RMSLE) between observed velocity variance $\widetilde{\sigma}_u^2(z)$ (Eq. 4.5) corrected by an estimated instrument error δ^2 , and modeled velocity variance $\widehat{\sigma}_u^2(f_p, S_p, z)$ as

$$\text{RMSLE}(f_p, S_p) = \sqrt{\frac{\sum_{i=1}^N (\log(\widetilde{\sigma}_u^2(z_i) - \delta^2) - \log(\widehat{\sigma}_u^2(f_p, S_p, z_i)))^2}{N}} \quad (4.6)$$

where N is the number of $\widetilde{\sigma}_u^2$ measurements in the upper 100 m (~ 31 data points when floats ascend), and δ^2 estimated as the average of observed $\widetilde{\sigma}_u^2(z)$ between 150 m and 200 m, assuming that surface wave signals are negligible within this layer. The \widetilde{S}_η is estimated using \widetilde{f}_p and \widetilde{S}_p (Eq. D.3). Confidence intervals of surface wave estimates are evaluated using the bootstrapping method (Roy 1994). We randomly select 80% of $\widetilde{\sigma}_u^2$ measurements in each profile to estimate surface waves and repeat 100 times. Results of 100 realizations are used to compute the mean and standard deviation of surface wave estimates.

Significant wave height \widetilde{H}_s is estimated using \widetilde{S}_η , assuming a Rayleigh distribution of surface waves (Young 1999) as

$$\widetilde{H}_s \approx 4\widetilde{\sigma}_\eta = 4\sqrt{\int \widetilde{S}_\eta df} \quad (4.7)$$

where $\widetilde{\sigma}_\eta^2$ is the estimated variance of ocean surface displacements.

4.5 Surface Waves under Typhoon Fanapi 2010

4.5.1 Surface wave estimates assuming the JONSWAP spectrum

The peak frequency \tilde{f}_p and significant wave height \tilde{H}_s are estimated using the observed velocity variance $\tilde{\sigma}_u^2$ in the upper 100 m (Fig. 4.3e-h), assuming the JONSWAP spectrum ($\sigma_a = 0.07$, $\sigma_b = 0.09$ and $\gamma = 3.3$ in Eq. D.3). Three successive profiles of $\tilde{\sigma}_u^2$ taken within 1.5 h are used in the fitting to reduce errors in estimates. We exclude profiles with no measurements in the upper 20 m, because the surface wave exponential depth-decaying scale (g/ω^2) is less than 20 m at frequencies > 0.12 Hz, where g is the gravity.

The sum of $\tilde{\sigma}_u^2$ (Eq. 4.5) from the orthogonal E_1 and E_2 may not equal the actual surface wave velocity variance, because some variance of surface waves might have been removed as the offset in the data processing on each pair of electrodes (Eq. C.22). In this study, the surface waves are estimated using measurements on E_1 and E_2 separately. The α effect on the estimated \tilde{H}_s is corrected using an empirical corrected function (section 4.7.3), derived using the simulated surface waves under Typhoon Fanapi in the WAVEWATCH III (ww3) model (section 4.6), assuming a random distribution of initial surface wave phase. The β effect on the \tilde{H}_s is corrected using the ww3 model output of surface wave propagation direction at f_p (section 4.7.4).

Estimates of \tilde{f}_p and \tilde{H}_s under Typhoon Fanapi using estimated $\tilde{\sigma}_u^2$ taken by two independent pairs of electrodes on each float agree with each other (Fig. 4.4). The mean and standard deviation of all fitted profiles' RMSLE (Eq. 4.6) is computed, $\sim 0.048 \pm 0.017$, respectively. At 0.4 day before the arrival of Typhoon Fanapi's eye, the \tilde{f}_p is about 0.07–0.08 Hz, and remains nearly constant until the passage of Fanapi. The \tilde{H}_s on the right side of Fanapi's track is mostly 6–10 m before the passage of Fanapi's eye. The \tilde{H}_s at the front-left quadrant of

Fanapi is about 6 m, and sometimes 5 m lower than at the front-right quadrant. After the eye of Typhoon Fanapi passes the float array, \tilde{f}_p changes from 0.08 to 0.1 Hz at floats em4906a (left) and em4910a (track), and about 0.08 ± 0.01 Hz on the right side of the track (em4907a and em4912a). The maximum \tilde{H}_s at the rear-left quadrant of Typhoon Fanapi is about 11 m at 0.15 day after the eye of Typhoon Fanapi passed the float (em4906a), nearly the same as that at the rear-right quadrant (em4907a).

The \tilde{f}_p at the rear-left quadrant of Fanapi is higher than at the front-right quadrant, supporting the spatial variability reported in previous model studies (e.g., Moon et al. 2004; Fan et al. 2009). The $\tilde{H}_s > 10$ m at the rear-left quadrant of Fanapi is higher than reported in studies using radar altimeters SRA under hurricanes (e.g., Wright et al. 2001; Fan et al. 2009). Because the RMSLE at the rear-left quadrant of Fanapi, ~ 0.043 , is within the 95% confidence interval, the nonlinear fitted results using the assumption of the JONSWAP spectrum may still be reliable. Note that Fanapi's translation speed U_h is $\sim 4 \text{ m s}^{-1}$. The slow motion of Fanapi may reduce the 'extended fetch' effect (Young 2003), and result in more symmetric \tilde{H}_s at the rear sector of Fanapi than other storms, e.g., $U_h \sim 5 \text{ m s}^{-1}$ in Hurricane Ivan (from NHC best track data). Collins (2014) also estimates surface waves under Fanapi, but the wave measurements on the nearest buoy were > 300 km to the left side of Fanapi's track, and therefore of little use in this analysis.

4.5.2 *Surface wave estimates assuming a single dominant surface wave*

Sanford et al. (2011) assume that estimated velocity variance $\tilde{\sigma}_u^2$ equals a single dominant surface wave's velocity variance as $\tilde{\sigma}_u^2 = \sigma_{u0}^2 e^{2kz}$, and linearly least-square fit the

observed profiles of $\widetilde{\sigma}_u^2$ to derive wavenumber k and σ_{u0}^2 in the logarithmical scale, i.e.,

$\log(\widetilde{\sigma}_u^2(z)) = 2kz + \log(\sigma_{u0}^2)$. The peak frequency $\widetilde{f}_p = (2\pi)^{-1}(gk)^{\frac{1}{2}}$ and significant wave

height $\widetilde{H}_s = 4\sigma_{u0}(gk)^{-\frac{1}{2}}$ are computed using estimated k and σ_{u0}^2 (Fig. 4.4). The \widetilde{H}_s is corrected for the α effect according to Eq. (4.5), and for β effects using the ww3 model output (section 4.7.4). The difference of \widetilde{H}_s due to the α and β effects can be more than 3 m (dashed lines vs. solid lines with dots in Fig. 4.4), unless these two effects (α : underestimated; β : overestimated) are fortuitously balanced by each other, i.e., the corrections of α and β effects are required.

Estimates of \widetilde{f}_p and \widetilde{H}_s are compared with the \widetilde{f}_p and \widetilde{H}_s using the JONSWAP spectrum (Fig. 4.4). At the positions of floats em4907a and em4906a (within 40 km of Fanapi's track; Fig. 4.4c and g), the \widetilde{f}_p is > 0.01 Hz lower than \widetilde{f}_p at 0.2 day before the passage of Fanapi's eye, and is < 0.01 Hz lower than \widetilde{f}_p after the passage of eye. The \widetilde{H}_s on the left side of Fanapi's track is about 1–2 m lower than \widetilde{H}_s , but mostly more than 3 m lower than at floats em4907a (right) and em4910a (track). The difference between \widetilde{f}_p and \widetilde{f}_p is less than 0.01 Hz at 92 km on the right side of Fanapi's track (em4912a; Fig. 4.4a), and more than 50% of \widetilde{H}_s differs from the \widetilde{H}_s within 2 m. The difference in surface wave estimates is due to the assumption of a surface wave spectrum, i.e., broadband vs. narrow band.

4.6 Surface Waves Simulations under Typhoon Fanapi in WAVEWATCH III (ww3)

WAVEWATCH III oceanic surface wave model version 5.16 (The WAVEWATCH III Development Group 2016) is developed by NOAA/National Centers for Environmental Prediction (NCEP), and has been used in studies of global and regional surface wave forecasts

(e.g., Moon et al. 2004; Reichl et al. 2014). In this study, we simulate surface waves under Typhoon Fanapi using ww3 (section 4.6.2) for several purposes: (1) to compare directly surface waves derived from floats with those from ww3 model simulations (section 4.6.3), (2) to justify the uncertainties of float estimates of surface waves due to the assumption of the JONSWAP spectrum (sections 4.7.1 and 4.7.2), and (3) to quantify the biases of float estimates of surface waves caused by the aliasing effect α (section 4.7.3) and the geomagnetic field inclination effect β (section 4.7.4).

4.6.1 *Typhoon Fanapi's wind forcing in the ww3*

The ITOP project is an international joint field experiment conducted in the western Pacific in 2010 to study the oceanic response under three tropical cyclones: Fanapi, Malakas, and Megi (D'Asaro et al. 2014). About 139 dropsondes were deployed from a C-130 aircraft to measure the vertical wind profiles in Typhoon Fanapi during September 14–18, with complementary measurements of wind speed at 10-m height above the sea surface taken by a Stepped-Frequency Microwave Radiometer (SFMR) mounted on the aircraft. With data assimilation of dropsondes and SFMR wind measurements, the wind field under Typhoon Fanapi is modeled using the Weather Research and Forecasting (WRF) model, supplemented with Navy Operational Global Atmospheric Prediction System (NOGAPS) products (Ko et al. 2014). The temporal resolution is 1 h, and horizontal spatial resolution is 0.0375° latitude \times 0.0375° longitude. At 01:30 UTC 18 September 2010, the maximum wind radius of Typhoon Fanapi was about 32 km, the maximum wind speed about 45 m s^{-1} , and the translation speed about 4 m s^{-1} (Fig. 4.1).

4.6.2 Simulated surface waves during Typhoon Fanapi in the ww3

The surface wave field under Typhoon Fanapi is simulated in the ww3 model from 01:00 UTC 17 September to 12:00 UTC 18 September (Fig. 4.5), using the model results of Typhoon Fanapi winds (section 4.6.1). The simulated directional surface wave number spectra are discretized in 24 directions of 15° intervals, and 45 frequencies from 0.012 to 1.3 Hz at a logarithmic increment $f_{n+1} = 1.1f_n$, following previously described methods (e.g., Moon et al. 2004; Fan et al. 2009; Reichl et al. 2014). The model includes wind forcing, wave–wave interaction and the dissipation due to white-capping and wave–bottom interaction. The wind forcing is parameterized in the package of ST2 following Tolman and Chalikov (1996) (The WAVEWATCH III Development Group 2016). The drag coefficient c_d of 2.5×10^{-3} is set, occurring at wind speed $> 30 \text{ m s}^{-1}$. The nonlinear wave–wave interaction is simulated using the discrete interaction approximation (Hasselmann et al. 1985). The temporal resolution is 180 s, and the spatial resolution 0.1° latitude x 0.1° longitude. The water depth is obtained from NOAA/National Centers for Environmental Information (NCEI) in the western Pacific.

At the front-right quadrant of Fanapi, simulated surface waves are longer and higher than waves at the rear-left quadrant, a pattern consistent with the simulated and observed surface wave fields under other tropical cyclones (Wright et al. 2001; Moon et al. 2004; Chen et al. 2013). The simulated propagating directions of surface waves in different quadrants also agree qualitatively with those observed under other tropical cyclones (Wright et al. 2001; Young 2006; Potter et al. 2015), i.e., propagating nearly perpendicular to the wind at the front-left quadrant of the typhoon, and nearly parallel with the wind at the right side of the storm’s track.

Black et al. (2007) and Holthuijsen et al. (2012) define three sectors to describe surface wave fields under tropical cyclones: front-left, right, and rear sector, based on reported observations of surface wave propagation directions relative to the wind. Frequency spectra of ocean surface displacement S_{η}^{ww3} in the ww3 model simulation show a similar single peak broadband structure in the three sectors (Fig. 4.6b–d), except that the spectrum shows double peaks within the eyewall of the typhoon (Fig. 4.6e), presumably due to complicated nonlinear wave–wave interactions suggested by Hu and Chen (2011). Surface waves have higher values of maximum spectral energy level S_p and significant wave height H_s in the right sector of Typhoon Fanapi (Fig. 4.5 and 4.6c). The S_{η}^{ww3} is used to compute the vertical profiles of surface wave velocity variance σ_{ww3}^2 (Eq. D.2). The σ_{ww3}^2 of surface waves with shorter mean wavelength in the rear sector of Typhoon Fanapi decays more rapidly with depth than in the right sector (Fig. 4.5 and 4.6f).

4.6.3 Comparison between model results and float estimates

The ww3 model outputs of f_p^{ww3} and H_s^{ww3} are compared with \tilde{f}_p and \tilde{H}_s on the EM-APEX floats (Fig. 4.7). Before the arrival of Fanapi, f_p^{ww3} at all float positions is about 10% higher than \tilde{f}_p (Fig. 4.7c), consistent with the validation of ww3 by Fan et al. (2009). H_s^{ww3} is in good agreement with \tilde{H}_s , with the difference < 2 m (Fig. 4.7f). After the passage of Typhoon Fanapi, f_p^{ww3} within 40 km of the track differs $> 20\%$ from \tilde{f}_p . The difference between H_s^{ww3} and \tilde{H}_s on the right side of Fanapi’s track is mostly within 2 m, in agreement with the validation of ww3 by Fan et al. (2009). Interestingly, the H_s^{ww3} at the rear-left quadrant of Fanapi can be > 5 m lower than \tilde{H}_s . Fan and Rogers (2016) present directional surface wave spectra under

Hurricane Ivan using SRA measurements, and make comparisons to the ww3 model simulations. The ww3 model underestimates/overestimates the spectral energy at the wind-wave/swell frequency at the rear sector of the hurricane. Better parameterizations of surface wave physics at the rear-left quadrant of Fanapi in the ww3 may be needed.

4.7 Simulations of Float Estimated Surface Waves using WAVEWATCH III (ww3)

4.7.1 JONSWAP model spectrum

Our method to estimate surface waves assumes the JONSWAP spectrum. The uncertainty due to this assumption is assessed using the simulated surface wave horizontal velocity variance $\sigma_{ww3}^2(z)$ (Fig. 4.6f), computed using S_{η}^{ww3} (Eq. D.2). Assuming $\overline{\sigma_{ww3}^2} = \sigma_{ww3}^2 + \delta^2$, \tilde{f}_p^{ww3} and \tilde{H}_s^{ww3} (superscript ww3 represents the simulated float estimates) are estimated using $\overline{\sigma_{ww3}^2}$ in the upper 100 m, assuming the JONSWAP spectrum ($\sigma_a = 0.07$, $\sigma_b = 0.09$, and $\gamma = 3.3$ in Eq. D.3). The δ is assumed 1 cm s^{-1} (Hsu et al. 2017). The vertical resolution of $\overline{\sigma_{ww3}^2}$ is 3 m, similar to the actual EM-APEX float measurements ($\sim 3 \text{ m}$).

The \tilde{f}_p^{ww3} and \tilde{H}_s^{ww3} are compared with the actual ww3 model outputs of f_p^{ww3} and H_s^{ww3} (Fig. 4.8 and 4.9). Most estimates of \tilde{f}_p^{ww3} and \tilde{H}_s^{ww3} (Fig. 4.9a and d) on the right side of Typhoon Fanapi's track agree with the f_p^{ww3} and H_s^{ww3} (Fig. 4.9b and e), and the $\Delta f_p/f_p^{ww3}$ ($\Delta f_p = \tilde{f}_p^{ww3} - f_p^{ww3}$) and $\Delta H_s/H_s^{ww3}$ ($\Delta H_s = \tilde{H}_s^{ww3} - H_s^{ww3}$) are less than 2% (Fig. 4.9c and f). The S_{η}^{ww3} differs slightly from the fitted JONSWAP spectrum (Fig. 4.6c). The $\Delta f_p/f_p^{ww3}$ and $\Delta H_s/H_s^{ww3}$ on the left side of the storm's track are larger but still within 5%, because the spectral peak of S_{η}^{ww3} (Fig. 4.6b) is broader than on the right side of the track. Our analysis

shows that \widetilde{f}_p^{ww3} and \widetilde{H}_s^{ww3} estimated assuming the JONSWAP spectrum are reliable outside the eyewall of Typhoon Fanapi, even the single spectral peak of the S_η^{ww3} is broader than the fitted JONSWAP spectrum. If the frequency of wind-waves and swell on the left hand side of the track is similar, e.g., $f = 0.08 - 0.10$ Hz in Wright et al. (2001), the S_η computed by integrating bi-modal ‘directional’ spectra will remain a broader and mono-modal spectrum feature.

However, within the eyewall of Typhoon Fanapi (grey shaded area in Fig. 4.8e and f), the $\Delta f_p / f_p^{ww3}$ and $\Delta H_s / H_s^{ww3}$ can be up to 25% and 14%, respectively, because the S_η^{ww3} has two spectral peaks within the eyewall (Fig. 4.6e). Therefore, our estimates using the float measurements within Fanapi’s eyewall (e.g., grey shaded area in Fig. 4.4e and f) might not be reliable.

4.7.2 Variations of empirical spectrum

We further evaluate the influence of variations in the spectral shape on surface wave estimates using $\widetilde{\sigma_{ww3}^2}$ (Table 4.1). Donelan et al. (1985) propose a one-dimensional surface wave spectrum $S_\eta^*(f_p, S_p, |\mathbf{U}_{10}|)$ (Eq. D.4). The single spectral peak in S_η^* near the f_p is mainly parameterized by the peak enhancement factor γ_d (Young 1999), similar to the S_η of the JONSWAP spectrum (Eq. D.3). But, the spectral energy of S_η^* is proportional to f^{-4} at $f \gg f_p$, instead of f^{-5} in the S_η of the JONSWAP spectrum. The \widetilde{f}_p^{ww3} and \widetilde{H}_s^{ww3} estimated using S_η^* are nearly the same as those estimated using the JONSWAP spectrum (Fig. 4.10). Surface waves’ spectral slope at high-frequency bands does not alter the estimates of surface waves significantly.

Previous studies (Hasselmann et al. 1976; Mitsuyasu et al. 1980; Lewis and Allos 1990; Young 1998) report values of non-dimensional shape parameters σ_a , σ_b , and γ in the JONSWAP spectrum varying within $\pm 50\%$ from their mean values ($\sigma_a = 0.07$, $\sigma_b = 0.09$, and $\gamma = 3.3$). We estimate \widetilde{f}_p^{ww3} and \widetilde{H}_s^{ww3} using different values of σ_a , σ_b , and γ within $\pm 50\%$ separately in the JONSWAP spectrum (Fig. 4.11), and conclude that variations of JONSWAP shape parameters within $\pm 50\%$ have negligible effects on our surface wave estimates.

4.7.3 *Surface wave estimates from rotating-frame measurements*

Measurements of $\widetilde{\sigma}_u^2$ are affected by EM-APEX float rotation (Table 4.1). The difference between $\widetilde{\sigma}_u^2$ and actual surface wave velocity variance depends on the float rotation rate and surface wave frequency, termed the rotational demodulation effect α in Eq. (4.5). Sanford et al. (2011) neglect the α effect and assume $\widetilde{\sigma}_u^2 = \sigma_{u0}^2 e^{2kz}$ (i.e., $\alpha = 3$ in Eq. 4.5), which may underestimate the $\sigma_{u0}^2 e^{2kz}$ measured by the rotating electrodes. We use ww3 model simulations to quantify the α effect.

We simulate 2,700 realizations of zonal propagating surface waves ($\theta = 0$) in each float profile using ww3 model outputs of S_η^{ww3} , assuming initial phase ϕ_0 randomly distributed from 0 to 2π . The motional induction of simulated surface waves then generates the simulated electric current \mathbf{J}' in the upper ocean (Eq. 4.3). The voltage measurements associated with simulated \mathbf{J}' are taken by the electrodes at a constant rotation rate $\Omega/2\pi$ (Eq. C.21), and then processed to generate the simulations of estimated velocity variance $\widetilde{\sigma}_{ww3}^2$ at the float positions (Eq. 4.5). The simulated rotation rate $\Omega/2\pi$ of EM-sensors is varied from 0.05 to 0.25 Hz. The float vertical

profiling speed is assumed 0.11 m s^{-1} , and the vertical resolution of $\widetilde{\sigma_{ww3}^2}$ is $\sim 3 \text{ m}$, similar to EM-APEX float measurements.

The \widetilde{f}_p^{ww3} and \widetilde{H}_s^{ww3} are estimated using the simulated float measurements $\widetilde{\sigma_{ww3}^2}$ at float em4907a in the upper 100 m, assuming the JONSWAP spectrum ($\sigma_a = 0.07$, $\sigma_b = 0.09$, and $\gamma = 3.3$ in Eq. D.3). We compare the \widetilde{f}_p^{ww3} and \widetilde{H}_s^{ww3} with the actual ww3 model outputs of f_p^{ww3} and H_s^{ww3} . The \widetilde{f}_p^{ww3} is consistent with the f_p^{ww3} and the standard deviation is $< 5\%$ (Fig. 4.12a). The frequency difference between surface waves and rotating electrodes does not affect estimates of \widetilde{f}_p^{ww3} . On the other hand, the \widetilde{H}_s^{ww3} is affected slightly by the difference between $\frac{\Omega}{2\pi}$ and \widetilde{f}_p^{ww3} (Fig. 4.12b). The $\frac{\widetilde{H}_s^{ww3}}{H_s^{ww3}}$ is about $\frac{1}{\sqrt{2}}$ if $\left| \widetilde{f}_p - \frac{\Omega}{2\pi} \right| > 0.07 \text{ Hz}$, and about $\frac{1}{2}$ if $\widetilde{f}_p \approx \frac{\Omega}{2\pi}$. The amplitude of any signals measured by the rotating electrodes will remain at least $\frac{1}{\sqrt{2}}$ of their actual amplitude, i.e., $\alpha = 1$ and $\widetilde{\sigma}_u = \frac{1}{\sqrt{2}} \sigma_{u0} e^{kz}$ (Eq. 4.5). The smaller the difference between $\frac{\Omega}{2\pi}$ and \widetilde{f}_p^{ww3} the more measurements of surface wave velocity variance near the f_p with non-zero averages are removed as the offset (Eq. C.22), i.e., $\alpha \rightarrow 0$ and $\widetilde{\sigma}_u = \frac{1}{2} \sigma_{u0} e^{kz}$ (Eq. 4.5), and the \widetilde{H}_s^{ww3} underestimation will be greater.

The $\frac{\widetilde{H}_s^{ww3}}{H_s^{ww3}}$ is averaged within every $\pm 0.01 \text{ Hz}$ interval of $\left| \widetilde{f}_p^{ww3} - \frac{\Omega}{2\pi} \right|$ to quantify the rotational demodulation effect α (Fig. 4.12b). The results at $\left| \widetilde{f}_p^{ww3} - \frac{\Omega}{2\pi} \right| > 0.07 \text{ Hz}$ maintain the constant of $1/\sqrt{2}$. The float estimated \widetilde{f}_p and the float rotation rate $\frac{\Omega}{2\pi}$ in this study are mostly within 0.04 Hz (covered by black bars in Fig. 4.12). The results averaged in $\left| \widetilde{f}_p^{ww3} - \frac{\Omega}{2\pi} \right| = 0 -$

0.04 Hz are used to correct the float estimates of \widetilde{H}_s (Fig. 4.4 in section 4.5), assuming surface waves with a random distribution of initial phase.

4.7.4 Geomagnetic field inclination and surface wave propagation direction effects

Measurements of $\widetilde{\sigma}_u^2$ affected by the geomagnetic field inclination effect β ($= F_y/F_z \sin \theta$) are further studied (Eq. 4.5). The difference between $\widetilde{\sigma}_u^2$ and actual surface wave velocity variance depends on the geomagnetic field inclination F_y/F_z and surface wave propagation direction θ . Sanford et al. (2011) neglect the geomagnetic field's inclination effect (i.e., $\beta = 0$ in Eq. 4.5), which may overestimate surface wave velocity variance by more than 2 times for the meridional propagating surface waves ($\beta^2 = 2.25$) at the front-left quadrant of Fanapi (section 4.6).

We use the surface wave propagation direction θ from the ww3 model output (Eq. 4.4) to assess the β effect on \widetilde{H}_s^{ww3} , because the β effect on \widetilde{f}_p^{ww3} is negligible (not shown in this study). The \widetilde{H}_s is estimated using 2,700 realizations of simulated float measurements $\widetilde{\sigma}_{ww3}^2$ (section 7.3) in the upper 100 m at float em4907a, assuming the JONSWAP spectrum ($\sigma_a = 0.07$, $\sigma_b = 0.09$, and $\gamma = 3.3$ in Eq. D.3). Estimates of \widetilde{H}_s are averaged and corrected for the rotational demodulation effect α (Fig. 4.12b) using estimates of \widetilde{f}_p^{ww3} . We expect that, after averaging over a random initial phase, the ratio of corrected \widetilde{H}_s^{ww3} to H_s^{ww3} equals to $\sqrt{1 + \beta^2}$ (Fig. 4.13), because $\widetilde{\sigma}_u \propto \sqrt{1 + \beta^2} \sigma_{u0}$ (Eq. 4.5).

The expression of β is for a single wave (Eq. 4.4). The effect of single wave-dependent β on \widetilde{H}_s^{ww3} estimated assuming the JONSWAP spectrum also needs to be assessed. Two

parameters β_m and β_p are computed using the ww3 model outputs of mean surface wave direction and wave direction at peak frequency, respectively (Kuik et al. 1988). The correlation coefficient between $\widetilde{H}_s^{ww3}/H_s^{ww3}$ and $\sqrt{1 + \beta_m^2}$ is about 0.75, and that between $\widetilde{H}_s^{ww3}/H_s^{ww3}$ and $\sqrt{1 + \beta_p^2}$ is about 0.88 (Fig. 4.13). Estimates of \widetilde{H}_s^{ww3} in this study are corrected for the β effect by dividing $\sqrt{1 + \beta_p^2}$ to the \widetilde{H}_s^{ww3} (Fig. 4.4 in section 4.5), i.e., corrected $\widetilde{H}_s^{ww3} = \widetilde{H}_s^{ww3}/\sqrt{1 + \beta_p^2}$. Most $\sqrt{1 + \beta_p^2}$ outliers occur when the $(\widetilde{f}_p^{ww3} - f_p^{ww3})/f_p^{ww3}$ is more than 5% (> one standard deviation in Fig. 4.12a), i.e., when the estimates of \widetilde{f}_p^{ww3} are poor. The root-mean-squared error between $\widetilde{H}_s^{ww3}/H_s^{ww3}$ and $\sqrt{1 + \beta_p^2}$ is about 0.08 at $(\widetilde{f}_p^{ww3} - f_p^{ww3})/f_p^{ww3} < 5\%$. It is used as one standard deviation to run 1,000 realizations of β_p as bootstrapping simulations to compute the uncertainties of corrected \widetilde{H}_s^{ww3} , $\sim 8\%$ (Fig. 4.4 in section 4.5).

4.8 Summary

Seven EM-APEX floats were air-launched from a C-130 aircraft under Typhoon Fanapi 2010 (D'Asaro et al. 2014) to measure oceanic temperature, salinity, current velocity, and high-frequency velocity variance $\widetilde{\sigma}_u^2$. The $\widetilde{\sigma}_u^2$ induced by the motion of surface waves (Longuet-Higgins et al. 1954; Sanford et al. 1978) in the upper 100 m are used to estimate the peak frequency \widetilde{f}_p and significant wave height \widetilde{H}_s , assuming the empirical JONSWAP spectrum under Typhoon Fanapi. The \widetilde{f}_p and \widetilde{H}_s are compared with the \widetilde{f}_p and \widetilde{H}_s estimated assuming a single dominant surface wave (Sanford et al. 2011) and the model outputs in the WAVEWATCH III

(ww3) model. The uncertainties of \tilde{f}_p and \tilde{H}_s on the EM-APEX floats due to assuming the JONSWAP spectrum are $< 5\%$ outside Fanapi's eyewall, but sometimes $> 10\%$ within the eyewall, assessed using the ww3 model outputs.

At 0.4 day before the arrival of Typhoon Fanapi's eye, the \tilde{f}_p is almost homogenous under Typhoon Fanapi, about 0.08 Hz. The \tilde{H}_s at the front-right quadrant of Typhoon Fanapi is about 6–10 m, and can be 5 m higher than that on the front-left quadrant. The spatial variability of surface wave height and wavelength before the arrival of Fanapi's eye has similar features with those reported using SRA measurements (Wright et al. 2001; Walsh et al. 2002; Fan et al. 2009). After the passage of Fanapi's eye, the \tilde{f}_p on the left side of Fanapi's track changes more significantly than on the right side of the track, from 0.08 Hz to 0.1 Hz. The \tilde{H}_s can be > 10 m at the rear-left quadrant of Typhoon Fanapi, and is higher than those estimated using SRA measurements at the rear-left quadrant of hurricanes (e.g., Wright et al. 2001).

Estimates of \tilde{f}_p and \tilde{H}_s are compared with \check{f}_p and \check{H}_s . The \tilde{f}_p is mostly > 0.01 Hz higher than \check{f}_p within 40 km of Fanapi's track at 0.2 day before the passage of Fanapi's eye. The greatest difference of peak frequency occurs on Fanapi's track, ~ 0.02 Hz. The difference between \tilde{H}_s and \check{H}_s is mostly 2–3 m, except those estimates on the left side of Fanapi's track. The difference in surface wave estimates is due to the surface wave spectrum assumed, i.e., broadband vs. narrow band. Assuming a broadband surface wave spectrum under tropical cyclones is more appropriate.

The \tilde{f}_p and \tilde{H}_s are also compared with the ww3 model outputs of f_p^{ww3} and H_s^{ww3} . The \tilde{f}_p is 10% lower than the f_p^{ww3} , in good agreement with the ww3 validation by Fan et al. (2009). In the rear sector of Fanapi in the ww3, the \tilde{f}_p on the three EM-APEX floats within 40 km of Fanapi's track is at least 20% lower than the f_p^{ww3} . Differences between \tilde{H}_s and H_s^{ww3} are mostly

within 2 m in the rear-right quadrant of Fanapi. In the rear-left quadrant of Fanapi, the \widetilde{H}_s can be 5.5 m higher than the H_s^{ww3} .

This chapter presents a method of using subsurface float measurements to study surface waves, avoiding the strong impacts of wave breaking and wind forcing on surface platforms. More than 180 surface wave estimates are presented at wind speeds $> 20 \text{ m s}^{-1}$ and outside of Fanapi's eyewall, including the complex surface wave field in the rear sector of storms (Black et al. 2007). In this study, we use surface wave propagation direction θ from the ww3 model output to correct the β effect on \widetilde{H}_s . An extension of this work would be developing a method to estimate θ using high-resolution voltage measurements. Direct observations of surface waves under tropical cyclones are important for guiding model simulations to study typhoon-wave-ocean interactions (Chen et al. 2013; Reichl et al. 2014).

Table

Notations in the equations of motional induction	
J	Electric current
x, y and z	Directions (positive x toward geomagnetic east, positive y toward geomagnetic north, and the depth z positive vertically upward from sea floor). x, y and z in the subscript of the parameters represent the components in the corresponding directions.
\hat{i} , \hat{j} and \hat{k}	Unit vectors in x, y, z directions
b	Electromagnetic field induced by ocean current
V	Ocean current velocity
F	Earth's geomagnetic field
σ	Electrical conductivity
Φ	Electric field potential
V_{sgw}	Surface waves' velocity
σ_{u0}^2	Horizontal velocity variance of surface waves at the ocean surface
ψ	Phase of surface waves
k_x and k_y	Wavenumber components in x and y directions, respectively
ϕ_0	Initial phase of the surface wave (at $x = 0$, $y = 0$ and $t = 0$)
θ	Surface wave propagation direction counterclockwise from the east
f	Surface waves' frequency
ω	Surface waves' angular frequency
k	Wavenumber magnitude
J'	Electric current induced by surface waves
$\overline{\left(\frac{J_x}{\sigma}\right)^*}$ and $\overline{\left(\frac{J_y}{\sigma}\right)^*}$	All depth-independent electric current terms in Sanford et al. (1978)
β	Geomagnetic field inclination effect
\bar{J}	Electric current induced by a low-frequency ocean current (Appendix C.1.3)

EM-APEX float estimated surface waves	
$-\nabla\Phi_{EM}$	Electric field around EM-APEX floats
$\widetilde{\sigma}_u^2$	Profiles of velocity variance measured by EM-APEX floats
\widetilde{f}_p and \widetilde{H}_s	Estimates of f_p and H_s using $\widetilde{\sigma}_u^2$ assuming the JONSWAP spectrum
\check{f}_p and \check{H}_s	Estimates of f_p and H_s using $\widetilde{\sigma}_u^2$ assuming the single dominant surface wave following Sanford et al. (2011)
Ω	EM-APEX float angular rotation frequency
Φ_i	Orientation of the two pairs of electrodes at $t = 0$ (Fig. 4.2)
t	Time in the 50-s harmonic fit
α	Rotational demodulation effect
Surface wave spectrum in the least-squared fitting method	
S_η	Surface wave spectral energy
S_p	Peak spectrum level of S_η at f_p
$\sigma_a, \sigma_b,$ and γ	Dimensionless shape parameters in the JONSWAP spectrum
f_p	Peak frequency
H_s	Significant wave height
$\widehat{\sigma}_u^2$	Modeled velocity variance of surface waves using empirical surface wave spectrum S_η
WAVEWATCH III model (ww3)	
σ_{ww3}^2	ww3 simulations of surface waves' horizontal velocity variance
$\widetilde{\sigma}_{ww3}^2$	Simulations of σ_{ww3}^2 measured by EM-APEX floats
\widetilde{f}_p^{ww3} and \widetilde{H}_s^{ww3}	Estimates of f_p and H_s using $\widetilde{\sigma}_{ww3}^2$
f_p^{ww3} and H_s^{ww3}	ww3 model output of f_p and H_s
S_η^{ww3}	ww3 model output of S_η

Table. 4.1. Notations in Chapter 4.

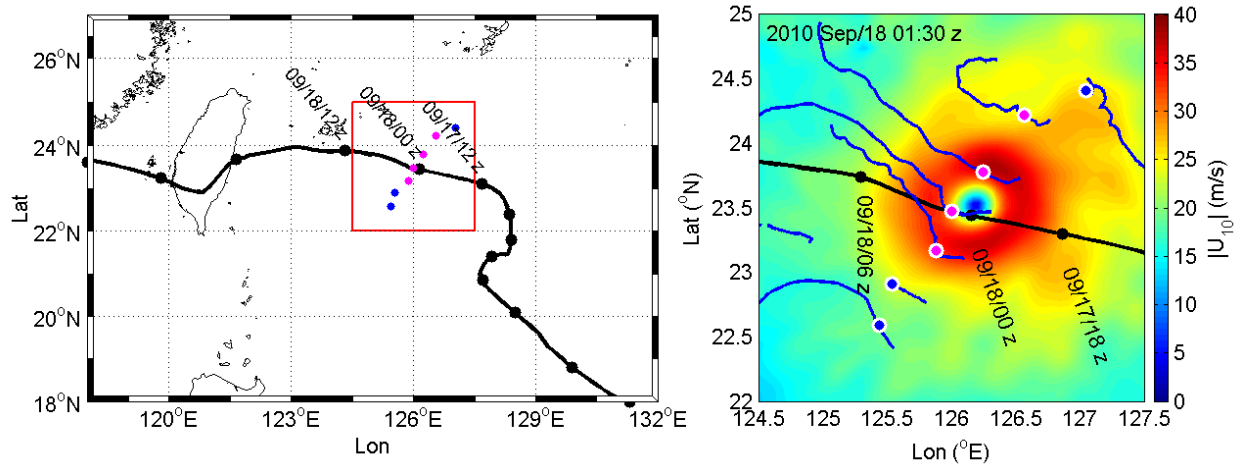


Fig. 4.1. (a) Typhoon Fanapi's track in the western Pacific (black curve with dots), deployment positions of EM-APEX floats (blue and magenta dots), and (b) the map of wind speed at 10-m height above the sea surface (color shading) and EM-APEX float positions (blue and magenta dots) at 01:30 UTC 18 September 2010 when Typhoon Fanapi arrived at the float array. Blue lines are the float trajectories. Typhoon track (black line with dots) is labeled with time as month/day/hour UTC. The construction of Fanapi's wind map $|U_{10}|$ is described in section 4.6.1. The measurements taken by four EM-APEX floats (magenta dots) within 100 km of Fanapi's track are mostly at $|U_{10}| > 20 \text{ m s}^{-1}$, and are used to estimate surface wave properties in Fig. 4.4.

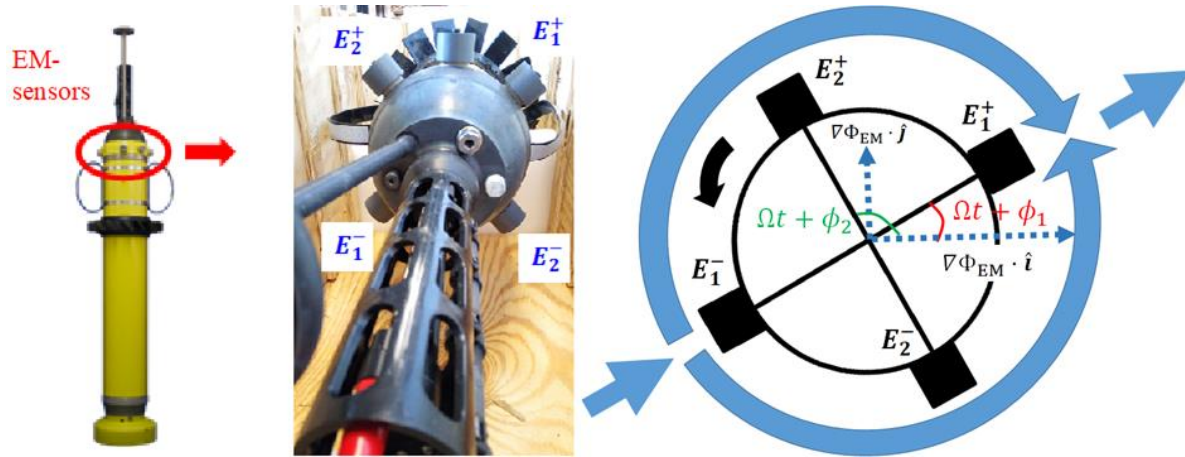


Fig. 4.2. Photo of EM-APEX floats (left), the top view of EM-APEX floats (middle), and an illustration of electric field around floats (right), $-\nabla\Phi_{EM}$ (blue arrows). The voltage measured by two orthogonal pairs of electrodes, E_1 and E_2 , is associated with the $\nabla\Phi_{EM}$. The float rotates counter-clockwise viewed from the top when ascending, at a rotation angular frequency Ω (black arrow). The angle between the pair of electrodes E_i and the magnetic east is $\Omega t + \phi_i$ ($i = 1$ for E_1 pair and $i = 2$ for E_2 pair). The projection of $\nabla\Phi_{EM}$ on E_i is equal to $(\nabla\Phi_{EM} \cdot \hat{i}) \cos(\Omega t + \phi_i) + (\nabla\Phi_{EM} \cdot \hat{j}) \sin(\Omega t + \phi_i)$, where t is the time and ϕ_i the initial phase at $t = 0$.

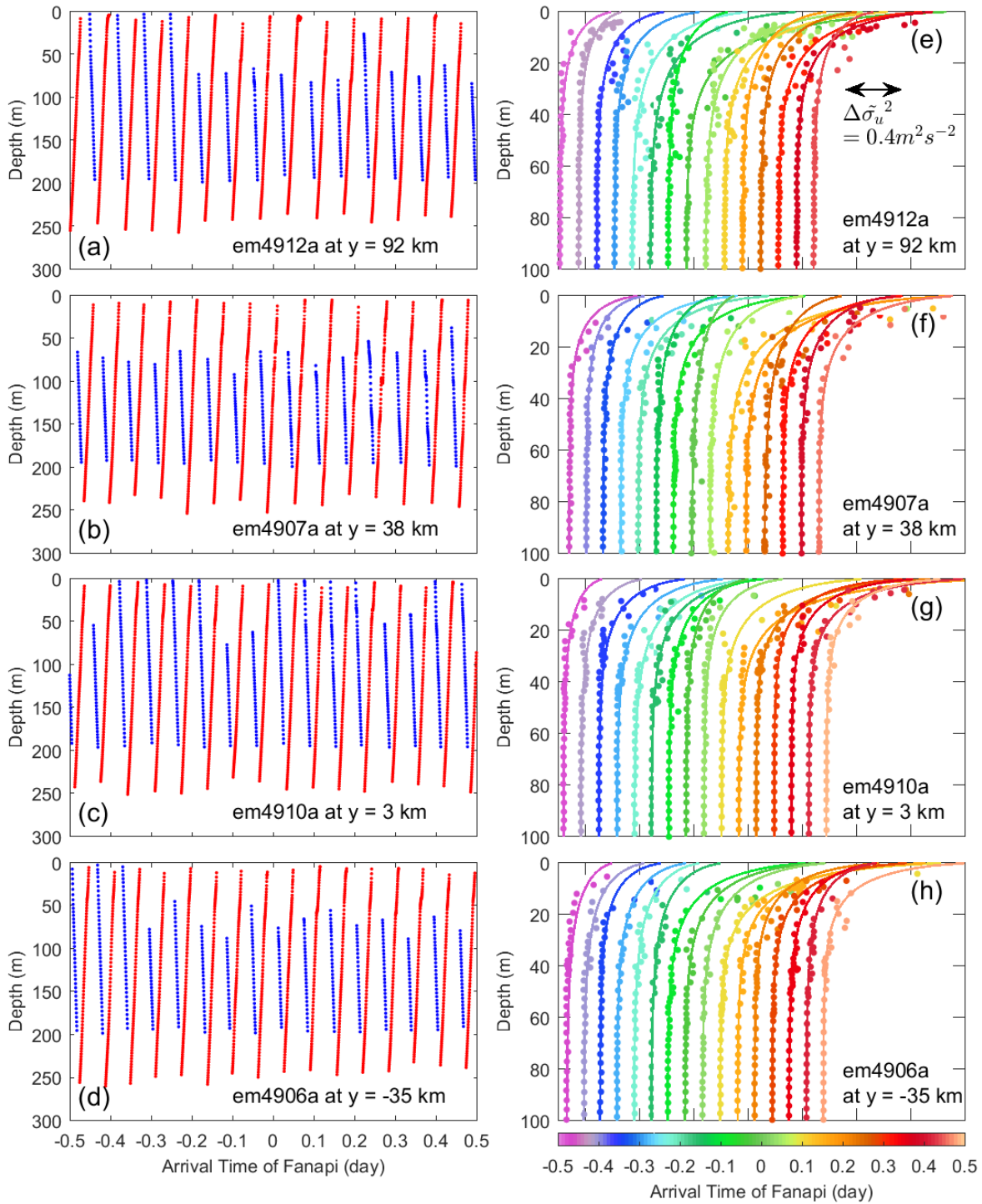


Fig. 4.3. Vertical positions of four EM-APEX floats near Fanapi's track descending (blue dots in a–d) and ascending (red dots a–d), and the profiles of measured velocity variance $\tilde{\sigma}_u^2$ taken by

one pair of the electrodes E_1 on the floats ascending (dots in e–h) at the time relative to the arrival time of Typhoon Fanapi’s eye at the float array (different colors in e–h). The abscissa in (a)–(d) is the time relative to the arrival time of Typhoon Fanapi’s eye at the float array. The scale of $\Delta\widetilde{\sigma}_u^2$ is presented in (e). Colored curves in (e)–(h) are the estimated surface wave profiles using the method described in section 4.4. The average float distance to Fanapi’s track is labeled in the lower-right corner in each panel, with the positive values to the right side of the track.

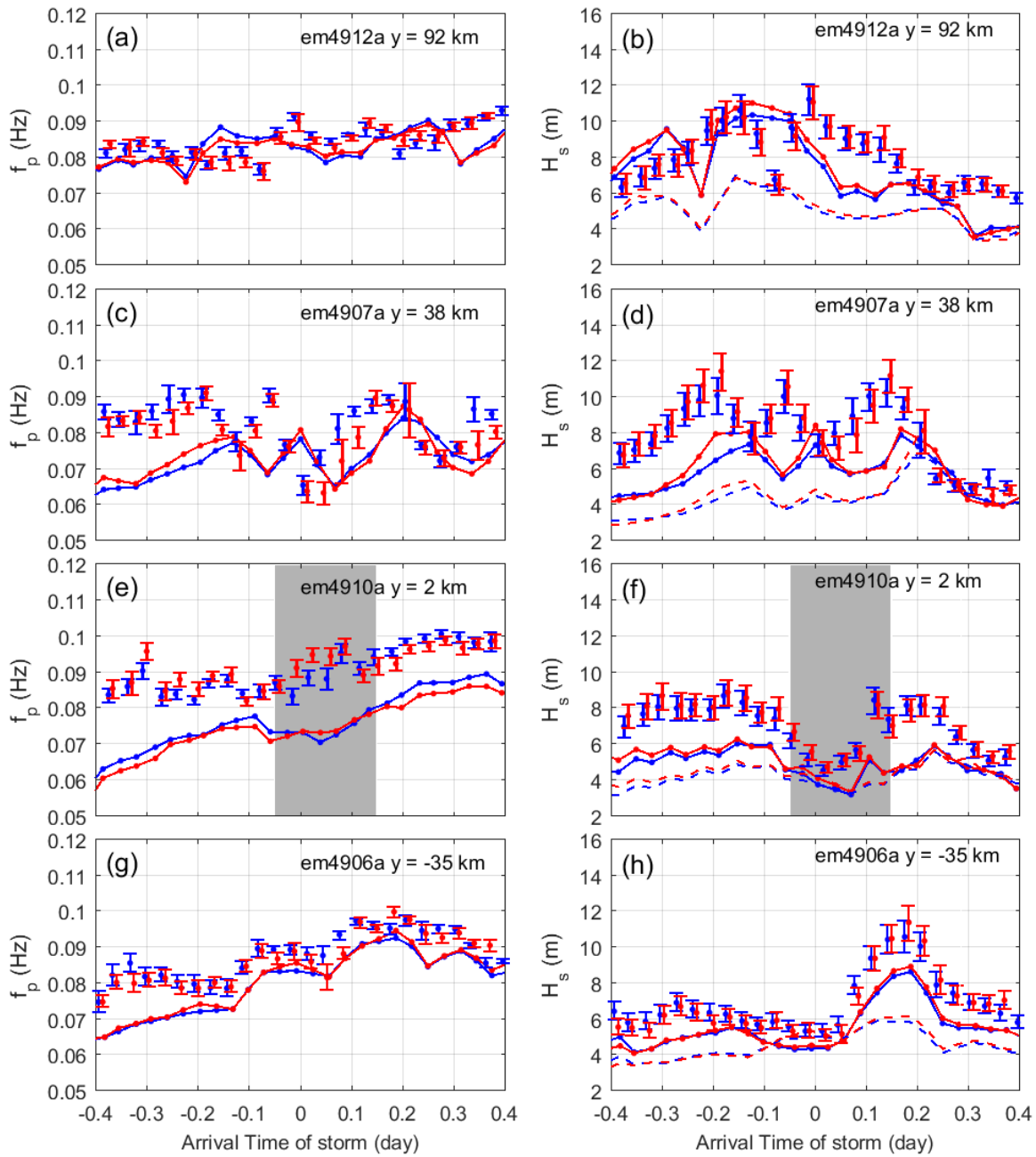


Fig. 4.4. EM-APEX float estimates of peak frequency (a, c, e, and g) and significant wave height (b, d, f, and h) under Typhoon Fanapi assuming the JONSWAP spectrum (\tilde{f}_p and \tilde{H}_s , dots with error bars as one standard deviation) or assuming a single dominant surface wave (\tilde{f}_p and \tilde{H}_s , dots connected with lines) on electrodes E₁ (blue) and E₂ (red) of four EM-APEX floats. Dashed

lines show the \overline{H}_s without the correction of α and β effects. The average float distance to Fanapi's track is labeled in the upper-right corner of each panel, with positive values to the right side of the track. The shaded grey area represents the poor surface wave estimates within Fanapi's eyewall due to the assumption of the JONSWAP spectrum (see Fig. 4.6).

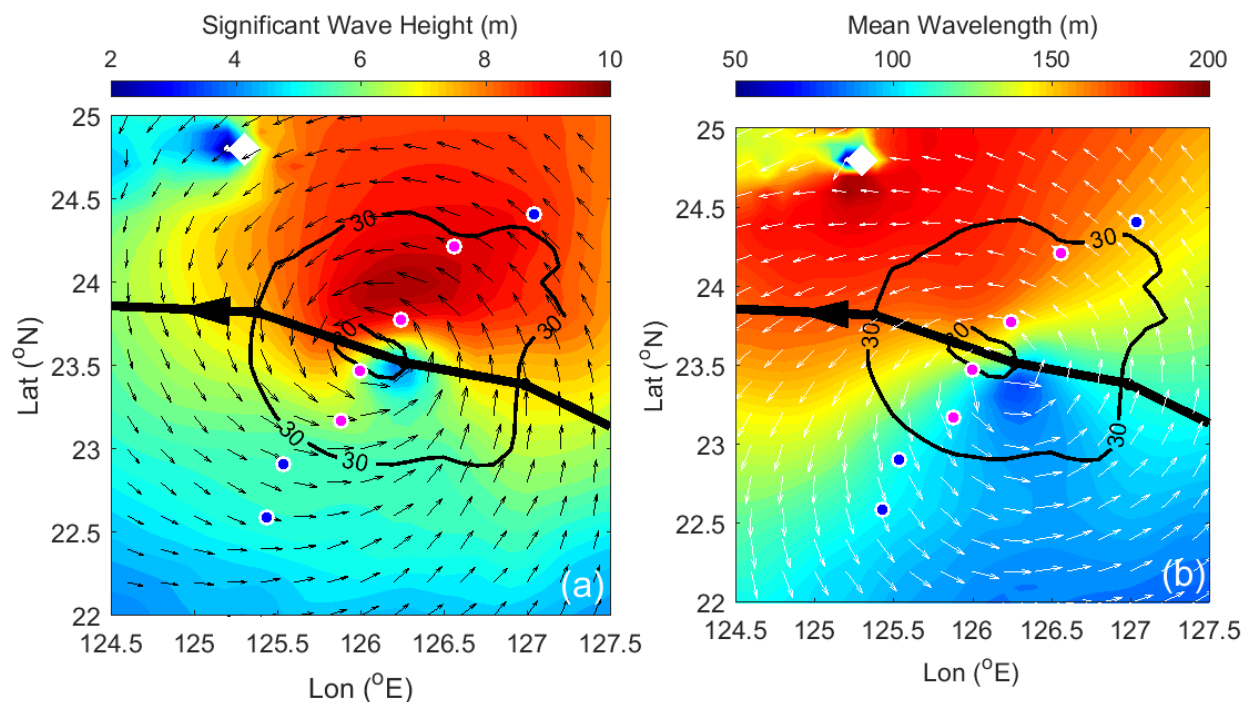


Fig. 4.5. WAVEWATCH III (ww3) model outputs of significant wave height (color shading in a), surface wave mean wavelength (color shading in b), and surface wave propagating direction (white arrows in b) at 01:30 UTC 18 September 2010 forced by the modeled Typhoon Fanapi winds $|\mathbf{U}_{10}|$ (m s^{-1}) (black contour lines and black arrows in a). The ww3 model results for surface waves at the EM-APEX float positions (e.g., blue and magenta dots) are used for the discussion of float estimated surface waves in this study. Typhoon Fanapi moved nearly westward (black thick line).

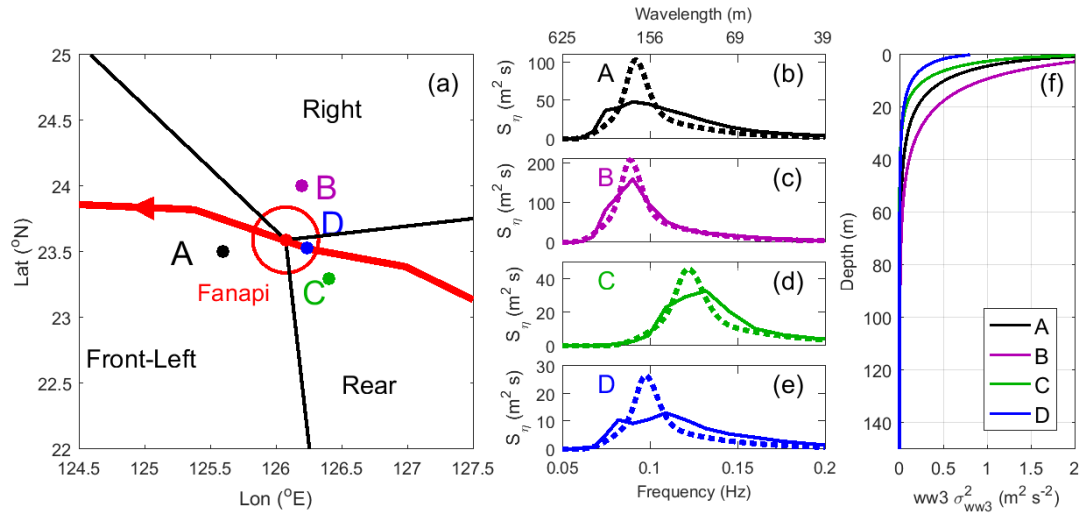


Fig. 4.6. WAVEWATCH III model outputs (ww3) of frequency spectrum of ocean surface displacement S_{η}^{ww3} (solid lines in b–e) at four locations (a) under Typhoon Fanapi: Front-Left (represented by black A), Right (represented by purple B), and Rear (represented by green C), and within the eyewall (represented by blue D within the red circle). Dashed lines show the fitted results assuming the JONSWAP spectrum. Typhoon Fanapi (red dot) moves along the storm’s track (red line) in the model. Profiles of σ_{ww3}^2 are computed (Eq. D.2) using the ww3 model results of surface wave spectra S_{η}^{ww3} at different locations (colored lines in f).

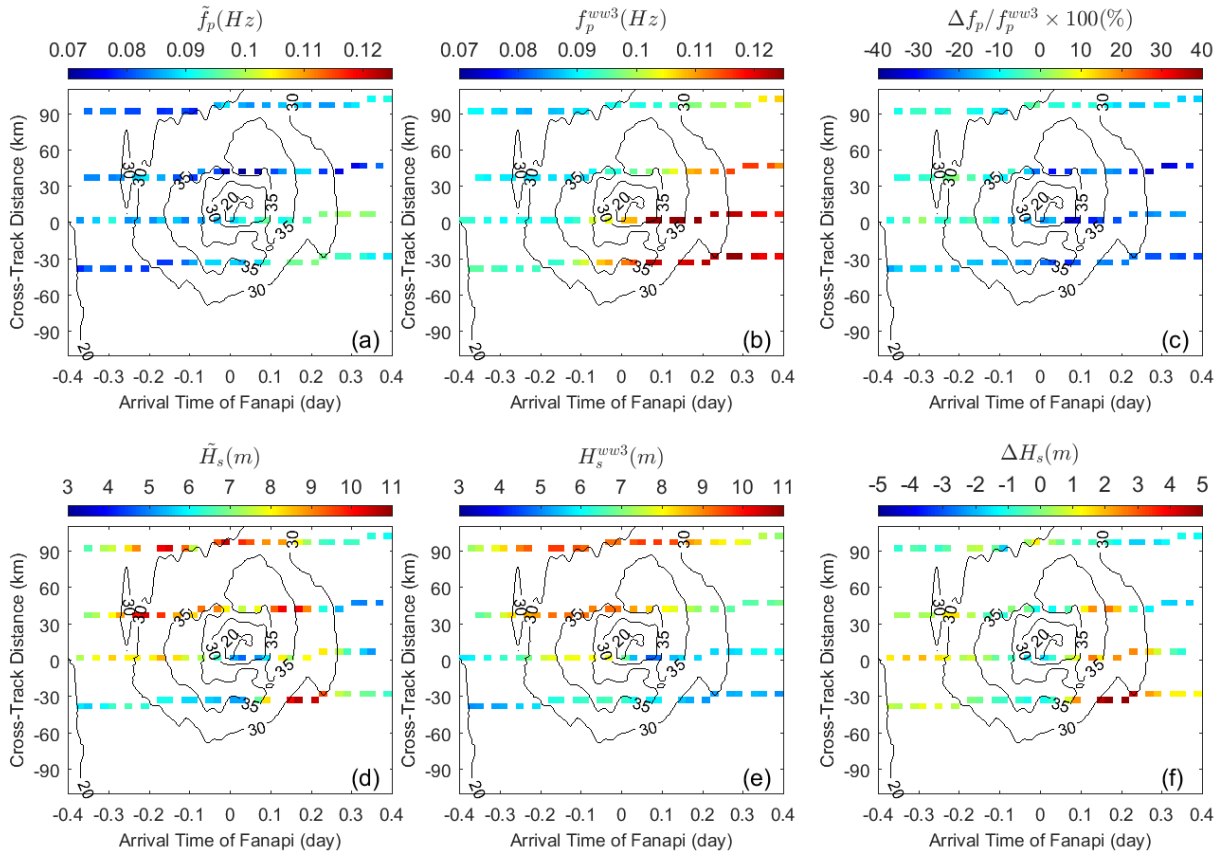


Fig. 4.7. Maps of EM-APEX float estimated peak frequency \tilde{f}_p (a) and significant wave height \tilde{H}_s (d) using results in Fig. 4.4, and the actual ww3 model outputs of f_p^{ww3} (b) and H_s^{ww3} (e). The ratio $\Delta f_p / f_p^{ww3}$ ($\Delta f_p = \tilde{f}_p - f_p^{ww3}$) and ΔH_s ($\Delta H_s = \tilde{H}_s - H_s^{ww3}$) are shown in (c) and (f), respectively. Black contour lines show the wind speed $|\mathbf{U}_{10}|$ (m s^{-1}) at 10-m height above the sea surface. The abscissa shows the relative arrival time of Typhoon Fanapi' eye to the float array. The ordinate is the distance of float positions to Fanapi's track.

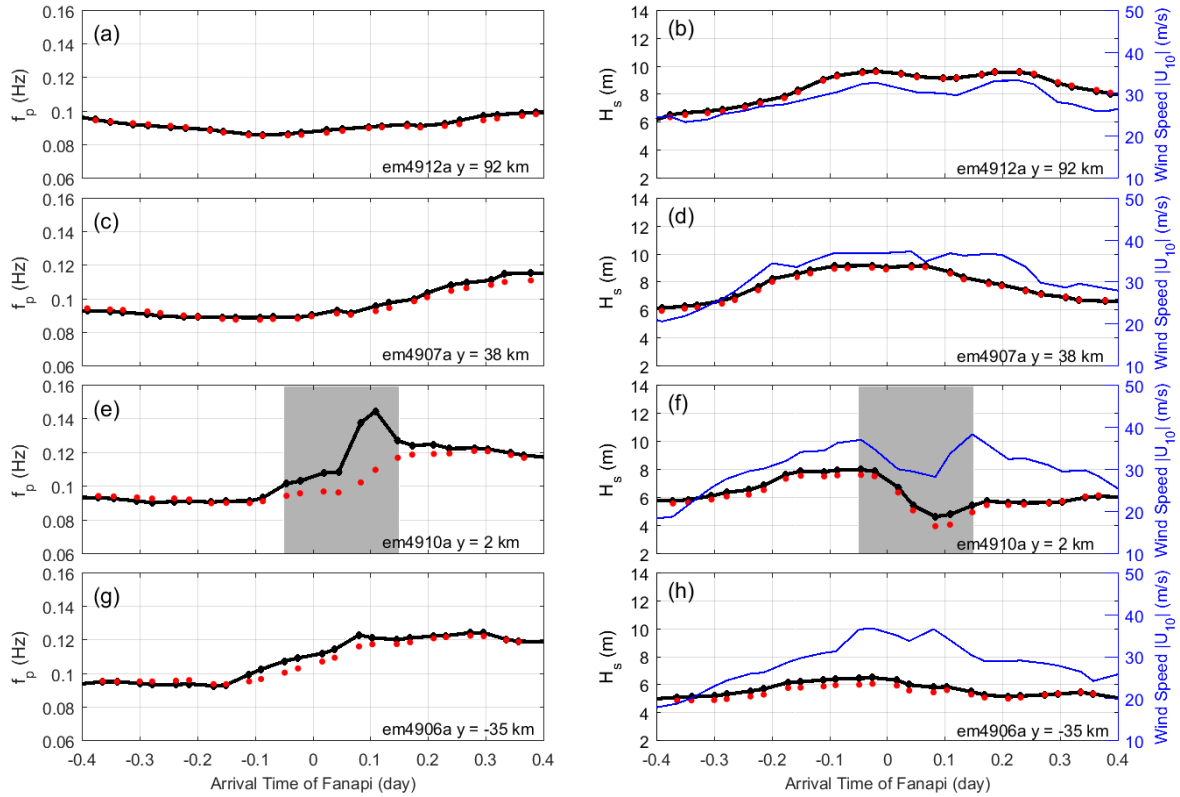


Fig. 4.8. Peak frequency \tilde{f}_p^{ww3} (a, c, e, and g) and significant wave height \tilde{H}_s^{ww3} (b, d, f, and h) estimated using the ww3 simulated $\widetilde{\sigma_{ww3}^2}$ (red dots) and the actual ww3 model outputs of f_p^{ww3} and H_s^{ww3} (black lines) at different float positions under Typhoon Fanapi. The average float distance to Fanapi's track is labeled in the lower-right corners of each panel, with the positive values to the right side of the track. The wind speed at 10-m height above the sea surface $|\mathbf{U}_{10}|$ (blue lines) is labeled on the right side of the right column (b, d, f and h). The grey area shades the poor estimates of $\Delta f_p / f_p^{ww3} > 5\%$ within the Fanapi's eyewall, due to the assumption of the JONSWAP spectrum, where $\Delta f_p = \tilde{f}_p^{ww3} - f_p^{ww3}$.

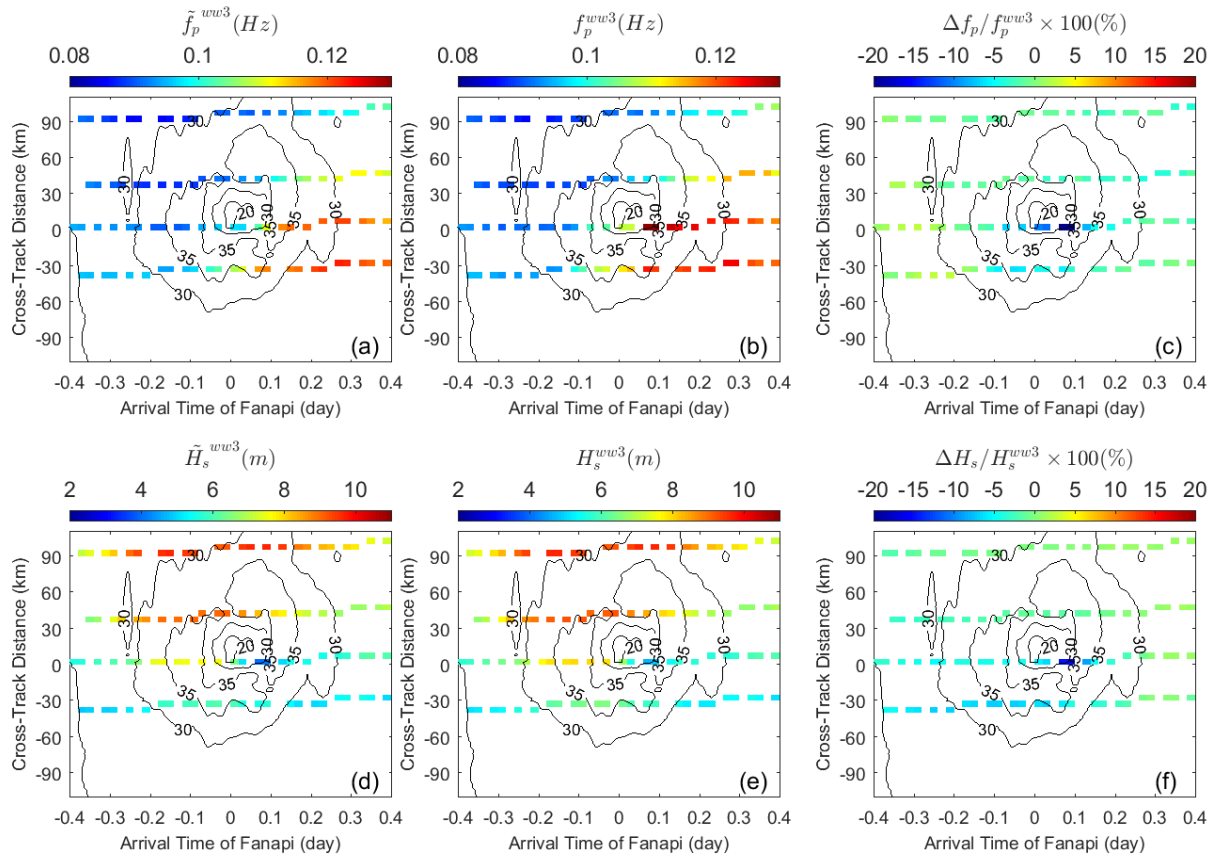


Fig. 4.9. Maps of ww3 estimated peak frequency \tilde{f}_p^{ww3} (a) and significant wave height \tilde{H}_s^{ww3} (d) using results in Fig. 4.8, and the actual ww3 model outputs of f_p^{ww3} (b) and H_s^{ww3} (e). The ratio $\Delta f_p / f_p^{ww3}$ and $\Delta H_s / H_s^{ww3}$ are shown in (c) and (f), where $\Delta f_p = \tilde{f}_p^{ww3} - f_p^{ww3}$ and $\Delta H_s = \tilde{H}_s^{ww3} - H_s^{ww3}$. Black contour lines are the wind speed at 10-m height above the sea surface. The abscissa is the relative arrival time of Typhoon Fanapi' eye to the float array. The ordinate is the distance of float positions to Fanapi's track.

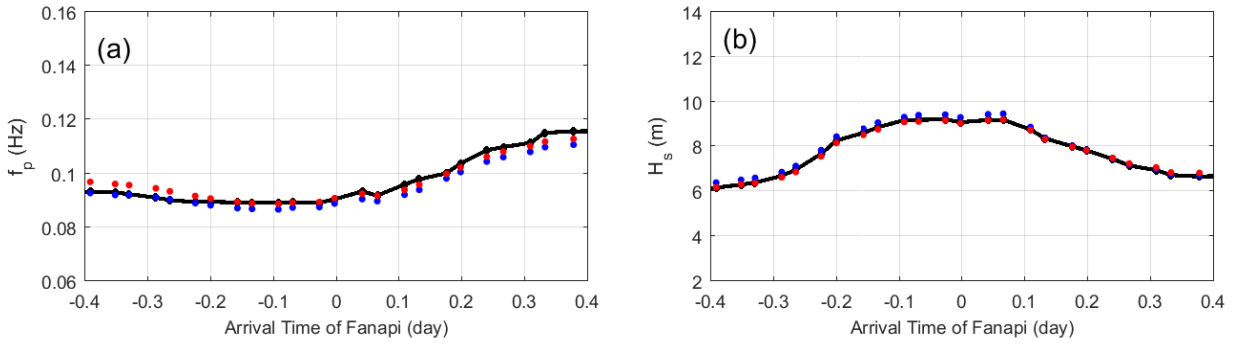


Fig. 4.10. Peak frequency \tilde{f}_p^{ww3} (a) and significant wave height \tilde{H}_s^{ww3} (b) estimated using the ww3 simulated $\widetilde{\sigma_{ww3}^2}$ at float em4907a, assuming the JONSWAP spectrum (blue dots) and the empirical spectrum in Donelan et al. (1985) (red dots), respectively. Black lines are the ww3 model outputs.

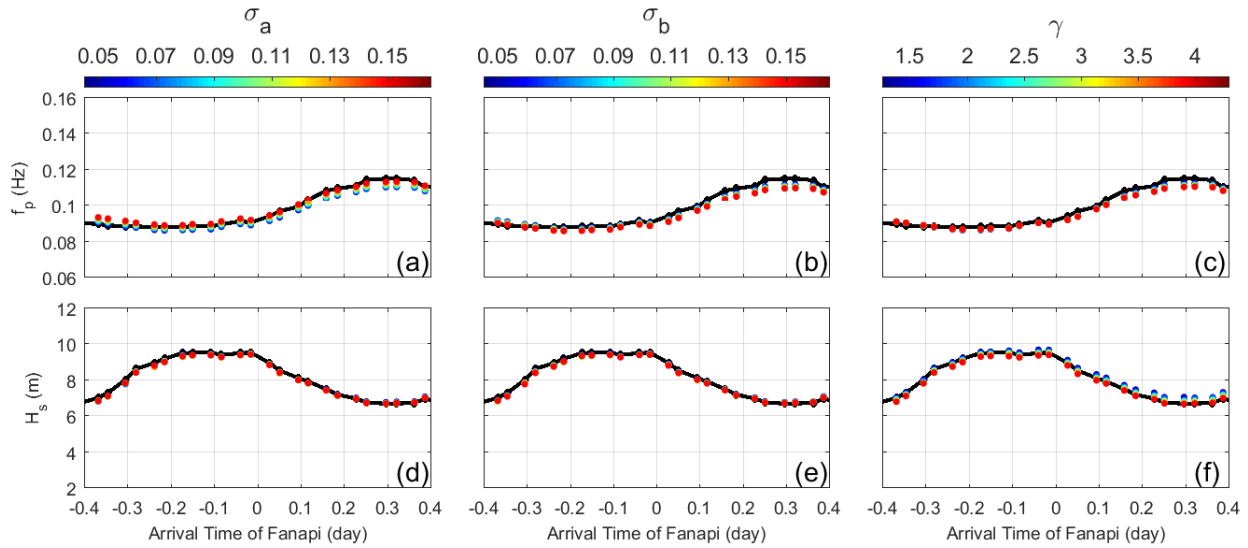


Fig. 4.11. Peak frequency \tilde{f}_p^{ww3} (a, b, and c) and significant wave height \tilde{H}_s^{ww3} (d, e, and f) estimated using the ww3 simulated $\widetilde{\sigma_{ww3}^2}$ at float em4907a, assuming different values for the shape parameters σ_a [different colors of dots in (a) and (d) with $\gamma = 3.3$ and $\sigma_b = 0.09$], σ_b [different colors of dots in (b) and (e) with $\gamma = 3.3$ and $\sigma_a = 0.07$], and γ [different colors of dots in (c) and (f) with $\sigma_a = 0.07$ and $\sigma_b = 0.09$] in the JONSWAP spectrum. Black lines with dots are the actual ww3 model outputs.

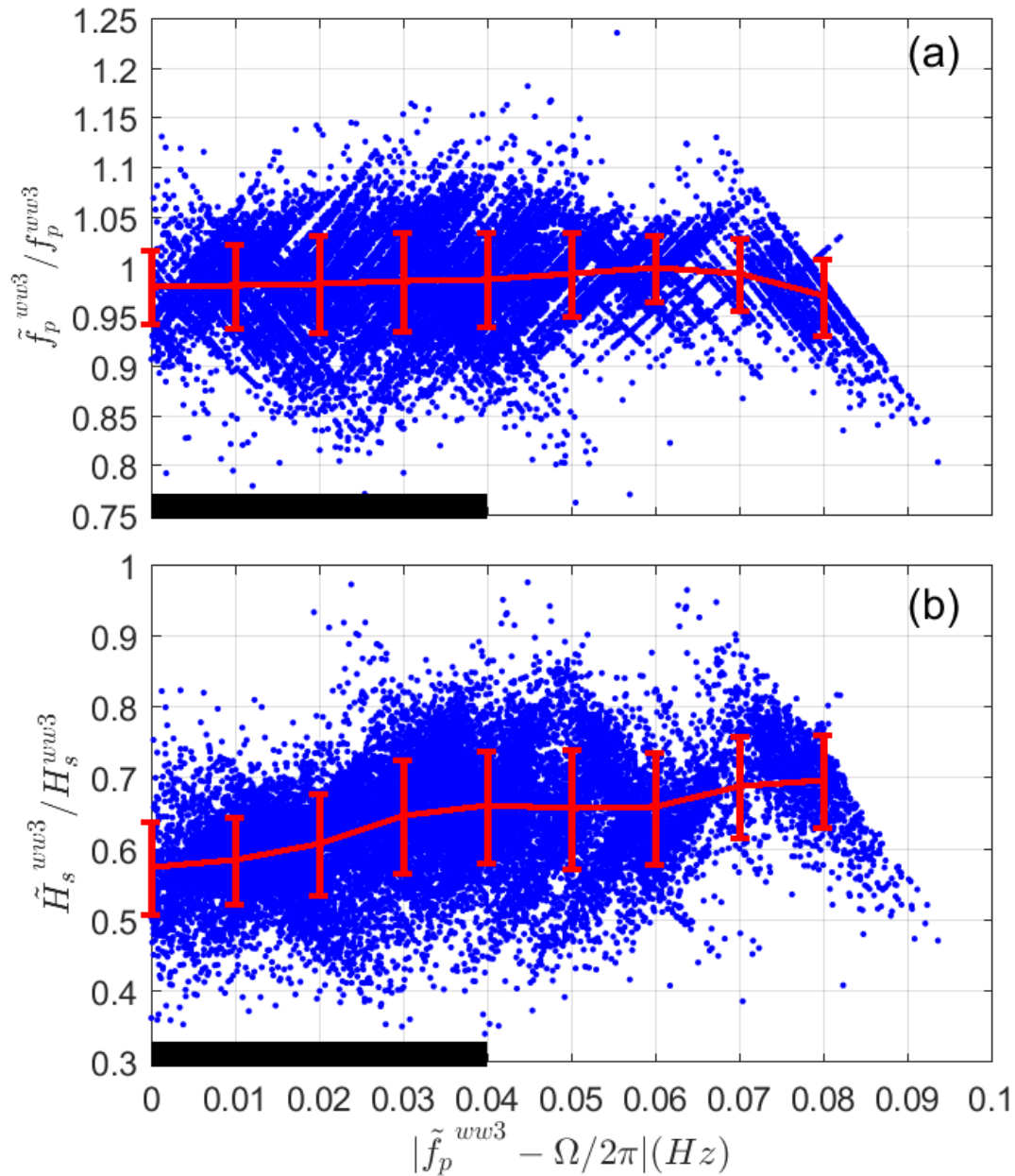


Fig. 4.12. Ratio of the ww3 estimated \tilde{f}_p^{ww3} (a) and \tilde{H}_s^{ww3} (b) to the actual ww3 model outputs of f_p^{ww3} and H_s^{ww3} at float em4907a. The mean and standard deviation are computed using the estimates in every ± 0.01 interval of $\left| \tilde{f}_p^{ww3} - \frac{\Omega}{2\pi} \right|$ (red lines with vertical bars as one standard deviation), where Ω is the float angular rotation frequency. The black bars indicate the range of $\left| \tilde{f}_p^{ww3} - \frac{\Omega}{2\pi} \right|$ covering float estimates of surface waves in Fig. 4.4.

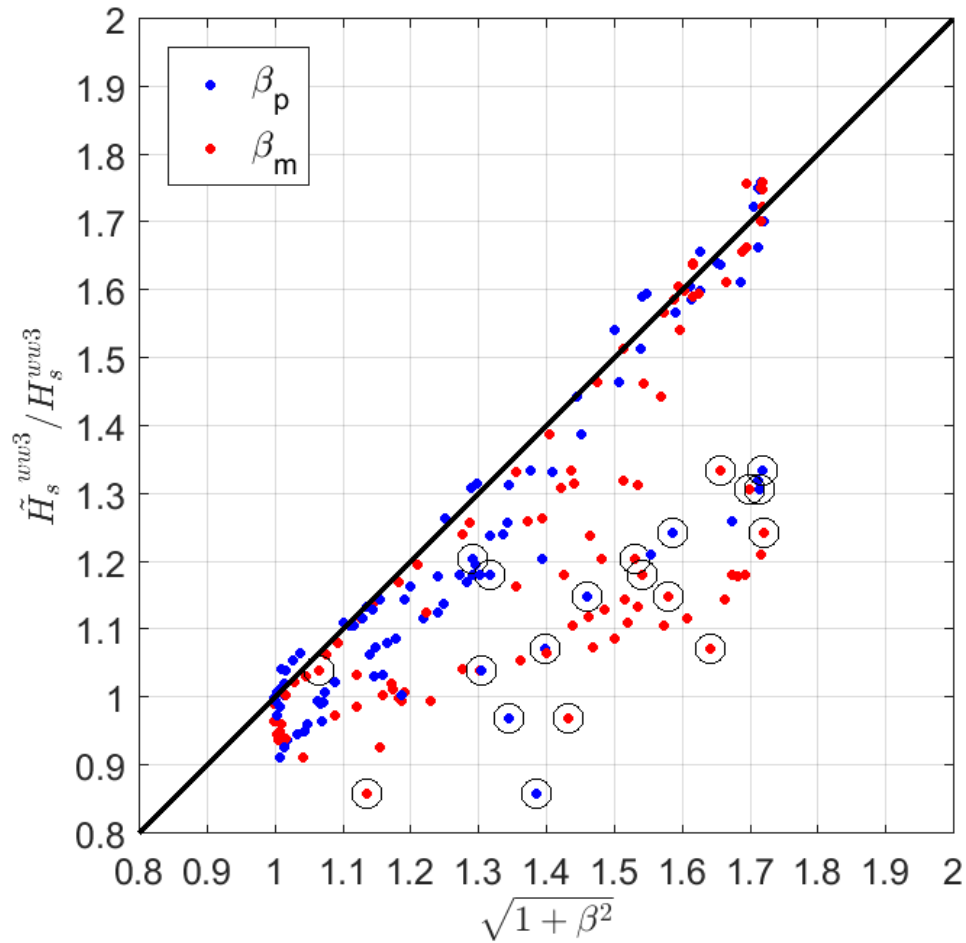


Fig. 4.13. Comparisons between the ratio of ww3 estimated \tilde{H}_s^{ww3} to actual ww3 model output of H_s^{ww3} and $\sqrt{1 + \beta^2}$. The \tilde{H}_s has already been corrected for the rotational demodulation effect α in Fig. 4.12b. The β_p and β_m are parameterized using the ww3 model outputs of surface wave direction at f_p (blue dots) and mean surface wave direction (red dots), respectively. The circles represent the \tilde{H}_s^{ww3} for poor estimates of $(\tilde{f}_p^{ww3} - f_p^{ww3})/f_p^{ww3} > 5\%$ (i.e., $>$ one standard deviation in Fig. 4.12a). See Fig. 4.12 for the definitions of \tilde{f}_p^{ww3} and f_p^{ww3} . The β_p is more suitable than β_m for correcting the uncertainties of \tilde{H}_s^{ww3} due to the geomagnetic field inclination effect.

Chapter 5. Conclusion

Nineteen EM-APEX floats deployed under five tropical cyclones (Hurricane Frances 2004, Hurricane Gustav 2008, Hurricane Ike 2008, Typhoon Fanapi 2010, and Typhoon Megi 2010) measured the profiles of ocean current velocity, temperature, salinity, and high-frequency velocity variance. The surface wind stress $\tilde{\tau}$ is estimated by integrating the tropical cyclone-induced momentum in the vertical, assuming the linear momentum budget balance. The results are assessed and corrected using the PWP3D model simulations; results are reliable before the eye passage of tropical cyclones. At wind speed $|\mathbf{U}_{10}| = 25 - 40 \text{ m s}^{-1}$, the downwind drag coefficient C_{\parallel} is $1.1 - 3.1 \times 10^{-3}$ in the front-right sector of tropical cyclones, and $0.8 - 1.7 \times 10^{-3}$ in the front-left sector. At wind speed $|\mathbf{U}_{10}| > 40 \text{ m s}^{-1}$, the C_{\parallel} is $\sim 1.6 \times 10^{-3}$. Most estimates of $\tilde{\tau}$ are clockwise from \mathbf{U}_{10} in the front-right sector of storms. The scattering of drag angle ϕ to the \mathbf{U}_{10} decreases with increasing $|\mathbf{U}_{10}|$.

A new data-based parameterization of drag coefficients is presented as a function of non-dimensional effective wind duration ζ^* , associated with wind forcing, storm translation speed, and fetch length. The $C_{\parallel}(\zeta^*)$ in the front-right sector of tropical cyclones decreases with increasing ζ^* , because stronger wave breaking may be forced by the wind of storms with faster translation speed. The $C_{\parallel}(\zeta^*)$ in the front-left sector of storms is lower than that in the front-right sector, presumably due to the larger angle between wind and waves, i.e., less efficient wind energy input to induce wave breaking.

Surface wave peak frequency f_p and significant wave height H_s are estimated under Typhoon Fanapi by a nonlinear least-squared fit to the profiles of high-frequency velocity variance measured by the floats and assuming the empirical JONSWAP spectrum. The f_p is $0.08 - 0.10 \text{ Hz}$, with the maximum f_p of 0.10 Hz in the rear-left quadrant of Fanapi, which is ~ 0.02

Hz higher than in the rear-right quadrant. The H_s is 6 – 12 m with the maximum in the rear sector of Fanapi. The assumption of a broadband JONSWAP spectrum, and the corrections for the effects of float rotation and Earth's geomagnetic field inclination, are all important to the surface wave estimates. The estimates of surface waves are compared to WAVEWATCH III (ww3) simulations. The differences between f_p and H_s at the rear-left quadrant of Fanapi are more than 20% and 5 m, respectively, suggesting the need to improve ww3 model simulations under tropical cyclones.

This work presents reliable methods for estimating surface wind stress and surface waves under tropical cyclones using subsurface EM-APEX float measurements. Estimates of drag coefficients and surface waves will be useful to parameterize the wind forcing to upper ocean motions and surface wave field under tropical cyclones in the future model simulations. The new parameterization of drag coefficients under tropical cyclones represents successfully the complicated wind–wave interactions in the open ocean. Future studies on air–sea interface dynamics are encouraged to enhance our understanding of tropical cyclone–wave–ocean interactions.

Appendix A. Tropical Cyclone Wind Maps Processing

A.1. Typhoon Megi Wind Field

A.1.1. Wind speed processing

Continuous wind estimates at 10-m height above the sea surface (\mathbf{U}_{10}) at each float were computed using data from aircraft penetrations of Typhoon Megi. Data from Vaisala RS92 dropsondes deployed by two WC-130J and one Taiwanese DOTSTAR aircraft (Wu et al. 2005) and from a nadir-looking stepped frequency microwave radiometer (SFMR, Uhlhorn and Black 2003) on the WC-130Js were used. These data can be obtained at http://catalog.eol.ucar.edu/itop_2010/. The positions of all measurements are determined by GPS data with an accuracy of better than 100 m.

The dropsondes measure horizontal wind velocity, temperature, and humidity from flight level to within a few meters above the sea surface. Wind speed accuracy is $\pm 0.5 \text{ m s}^{-1}$ (UCAR 2016). The \mathbf{U}_{10} was computed directly from the RS92 dropsonde profiles.

The SFMR measures the brightness temperature, which is used to estimate surface wind speed continuously along the aircraft track with a nominal error of 4.0 m s^{-1} (Uhlhorn and Black 2003) for winds greater than 20 m s^{-1} . The SFMR data were calibrated to the dropsonde 10-m winds using all SFMR and dropsonde data collected during ITOP. The SFMR measurement with only the highest quality data ($Q_2 = 4$) was used to calibrate each nearby dropsonde measurement of \mathbf{U}_{10} . Measurement pairs separated by more than 18 s were rejected. A total of 343 pairs remained. Significant bias errors were found after comparing dropsonde and SFMR measurements at the same wind speed, and were corrected using a cubic polynomial in $\log_{10}(|\mathbf{U}_{10}|)$. Corrections are small, 2 m s^{-1} or less for $|\mathbf{U}_{10}| = 20\text{--}50 \text{ m s}^{-1}$, but rise rapidly below this. The SFMR winds below 20 m s^{-1} were discarded in this study. The corrected SFMR data

matched the dropsonde data with an RMS error of 3.5 m s^{-1} , less than the nominal SFMR error of 4.0 m s^{-1} (Uhlhorn and Black 2003) and much more than the dropsonde error of 0.5 m s^{-1} . The differences showed no trends in time, with aircraft number, with the distance between the plane and the dropsonde, or with the logged quality of the data.

The corrected SFMR winds, regardless of logged quality, and the 10-m dropsonde winds were used to create maps of the $|\mathbf{U}_{10}|$ of Megi. Data from three aircraft surveys were used. Flight 530W deployed 16 dropsondes during two passes through the storm from ~00:00 UTC – 04:00 UTC 16 October, immediately after deploying the EM-APEX floats. Flight 630W deployed 44 dropsondes during three passes through the storm from ~21:00 UTC 16 October to ~03:00 UTC 17 October. This was coordinated with a DOTSTAR flight that deployed 10 additional dropsondes around the periphery of the storm. During this survey 744 data points (13 dropsondes) were within 100 km of the storm center at six different azimuths. This survey coincided with the passage of the storm's eye through the float array and is the primary source of data for the drag coefficient calculations. Flight 830W deployed 27 dropsondes during four passes through the storm from ~11:00 UTC to 16:00 UTC 17 October.

For each survey, a continuous wind field was created in two steps. First, a radially symmetric wind field was fit to the observations. For radii $r > R_{\text{max}}$ the form $V = (V_{\text{max}} R_{\text{max}}/r)^n$ was used. For $r < R_{\text{max}}$, the form $V = V_{\text{max}} (r/R_{\text{max}})$ was used. Within the eye, $r < R_{\text{eye}}$, $V = V_{\text{eye}}$. Fig. A.1 shows this function for the 17 October survey ($n = 0.5$, $R_{\text{max}} = 12 \text{ km}$, $V_{\text{max}} = 70 \text{ m s}^{-1}$, $R_{\text{eye}} = 6 \text{ km}$, and $V_{\text{eye}} = 10 \text{ m s}^{-1}$). Although this captures much of the wind variations, azimuthal deviations of up to $\pm 10 \text{ m s}^{-1}$ are apparent. Both true azimuthal variations in the storm structure and errors in the location of the storm center used to make the radial map can cause the deviations. These deviations were then mapped (red regions in Fig. A.2 representing a higher

wind speed than the radial model, and blue regions in Fig. A.2 representing a lower wind speed) by smoothing the observations in polar coordinates using a Gaussian smoother with scales of 0.1 in $\log_{10}(r)$ and $\pi/4$ in azimuth, and added to the radially symmetric model to form a wind field for the storm at the time of the survey. The standard deviation of the maps from the data is 1.8 m s^{-1} for Typhoon Megi, well within the expected uncertainty in the SFMR data. The deviations at the peak winds are $< 1 \text{ m s}^{-1}$. Two maps of the surface wind speed between the surveys, one earlier and one later, were constructed by moving the survey fields along the storm track, e.g., the wind map of 17 October in Fig. A.3. The $|\mathbf{U}_{10}|$ on the floats is computed by linearly interpolating these two maps in time.

The float positions are computed by linearly interpolating between roughly hourly GPS fixes, when these are available. Between approximately yeardays 289.4 and 291.5, the floats stopped surfacing to avoid damage and no GPS fixes are available. During these times, float positions were estimated by integrating the depth-average velocity measured by the floats, starting from the last GPS fix and adjusting this trajectory with a linear trend to hit the next GPS fix. The error is estimated from the size of this adjustment, typically a few centimeters per second, resulting in a position error of a few kilometers. The wind speeds computed at these floats' positions are used to calculate drag coefficient in this study (Fig. A.4).

For the outer two floats, the lateral gradients are small. The uncertainty in the estimated wind speed is dominated by measurement and mapping errors. The former uncertainty is taken as the RMS SFMR error $\sim 3.5 \text{ m s}^{-1}$, and the latter is conservatively taken as the RMS deviation of the data from the map $\sim 1.8 \text{ m s}^{-1}$. Combining these yields 4.0 m s^{-1} RMS. This error is conservative because much of the estimated SFMR error is undoubtedly due to variability in the dropsonde velocity estimates due to boundary layer turbulence.

The central float, under the greatest wind speed, passed under the storm eyewall north of the eye but inside the maximum wind region – one of high spatial gradients. The resulting time series of wind at the float is highly sensitive to the exact float track and the details of the wind map. In particular, the double wind peak results from the float passing under the comma-shaped wind maximum (Fig. A.4). Neither the float track nor the wind map are sufficiently accurate to capture the details of this feature correctly. This large uncertainty only occurs for about one hour while the float was in Megi’s eyewall, with a plausible estimate of the RMS wind speed uncertainty at any given time $\pm 10 \text{ m s}^{-1}$. The uncertainty in the peak hourly average wind speed is less, because the float position is known to about 1 km from a recent GPS fix and the small advective velocities. Because the storm moved nearly westward, the float certainly went through the eyewall north of the eye in a region of 50–80 m s^{-1} winds. The average wind during this time is estimated at $71 \pm 5 \text{ m s}^{-1}$ computed by fitting a smoothing spline to the nearby data points and resampling them randomly.

A.1.2. Inflow angle of Typhoon Megi

A basic description of inflow angle of tropical cyclones is provided by the NOAA hurricane report (1979). Zhang and Uhlhorn (2012) studied the inflow angles of tropical cyclones using data taken from >1000 GPS dropsondes deployed in 18 tropical cyclones from 1998 to 2010. After removing the effect of storm motion on the cyclone wind, the Cartesian wind vector is transformed to the tangential (u_t) and radial wind (u_r) components. The storm-relative inflow angle α is defined as

$$\alpha = \tan^{-1} \left(-\frac{u_r}{u_t} \right).$$

The inflow angle α is positive when the air mass is transported inward to the eye of tropical cyclones.

Following Zhang and Uhlhorn (2012), we use data taken from GPS dropsondes deployed in Typhoon Megi between 01:00 UTC 16 October and 12:00 UTC 17 October to compute the inflow angle α . The mean of α ($\bar{\alpha}$) and standard deviation of α (σ_α) are computed within the layer between 10 and 50 m above the sea surface (blue dots and vertical lines in Fig. A.5). The distance of each GPS dropsonde profile to the eye of Typhoon Megi is normalized by the radius of the storm's maximum wind (R_{\max}) as r^* . At the front-right quadrant of the storm beyond R_{\max} , i.e., $r^* > 1$, the standard deviation σ_α is less than 5° .

We average $\bar{\alpha}$ within the front-right quadrant of the storm in three different bins of r^* corresponding to the distances of three EM-APEX floats nearest Typhoon Megi's eye. The average of $\bar{\alpha}$ is $20 \pm 5^\circ$ at $r^* = 1-1.5$, $32 \pm 8^\circ$ at $r^* = 3.4-4.4$, and $30 \pm 13^\circ$ at $r^* = 5.2-6.8$. Our results of $\bar{\alpha}$ within the front-right quadrant of Megi agree with those reported by Zhang and Uhlhorn (2012). In the present analysis, the storm-relative wind direction in Typhoon Megi is interpolated assuming α increases linearly from zero at Megi's eye to a peak value of 35° at $r^* = 2$, and decreases to 32° at $r^* = 6$. The effect of the storm motion is added to yield the interpolated vector wind field.

A.2. Tropical Cyclone Wind Fields of Frances, Gustav, Ike, and Fanapi

Wind measurements taken by dropsondes and SFMR under Frances, Gustav, Ike, and Fanapi are analyzed and used to process the tropical cyclones' wind maps, following Appendix (A.1.1). Dropsondes profiled the wind vector from flight level to a few meters above the sea surface. The $|\mathbf{U}_{10}|$ is estimated by linearly fitting profiles from 5 to 100 m above the sea surface

in a logarithmical scale. The accuracy of dropsonde wind speed measurements is within 0.5 m s^{-1} (UCAR/NCAR 1993). The SFMR mounted on the bottom of aircraft remotely sense the brightness temperature to estimate $|\mathbf{U}_{10}|$ (Uhlhorn and Black 2003). The SFMR measurements are corrected using the nearby dropsonde wind measurements. The root-mean-squared error (RMS) between corrected SFMR and dropsonde measurements at $|\mathbf{U}_{10}| > 20 \text{ m s}^{-1}$ is $2.0 - 2.9 \text{ m s}^{-1}$ at different tropical cyclones.

Every tropical cyclone was surveyed at least twice, before and after eye passage of the EM-APEX floats positions. The time interval between the two surveys in every tropical cyclone was about 1 day. The continuous wind field for each survey is constructed in two steps. First, a radially symmetric model of $|\mathbf{U}_{10}|$ under tropical cyclones is fitted to the observations. The maximum wind speed V_{\max} at the radius of R_{\max} is estimated by bin-averaging the observations in the radius intervals of 3 km. For radii $r > R_{\max}$, the form $|\mathbf{U}_{10}| = V_{\max}(r^*)^n$ is used, where $r^* = r/R_{\max}$ is the normalized distance to the eye. The parameter n is fitted in the logarithmical scale using the observations at the distance of 1 to $5 R_{\max}$. For radii $r = R_{\text{eye}} - R_{\max}$, the form $|\mathbf{U}_{10}| = V_{\max}r^*$ is used. Within the eye $r < R_{\text{eye}}$, $|\mathbf{U}_{10}| = V_{\text{eye}}$. The constant wind speed V_{eye} is estimated by minimizing the standard deviation of wind speed measurements within the radius of R_{eye} . The motion of tropical cyclone eyes during the surveys ($\sim 4 \text{ h}$) is assumed constant, and determines the distance of observations to tropical cyclone eyes in different azimuths. Assuming a symmetric wind field under tropical cyclones, tropical cyclone tracks are optimized by minimizing the RMS of $|\mathbf{U}_{10}|$ between the radial model and observations. The $|\mathbf{U}_{10}|$ of observations is then smoothed in the polar coordinates to generate the wind field, using a Gaussian smoother with scales of 0.05 in $\log_{10}(r)$ and scales of π/m in azimuth, where m is the number of the flight's penetration through the eyes in each survey. The RMS mapping errors

between the wind maps and data are all $< 1.9 \text{ m s}^{-1}$. The RMS error of $|\mathbf{U}_{10}|$ is summarized using the mapping and measurement errors, about $2.4\text{--}3.4 \text{ m s}^{-1}$ in different tropical cyclones. The $|\mathbf{U}_{10}|$ at the positions relative to the tropical cyclones' eyes is linearly interpolated in time using the maps. The motion of tropical cyclones between two surveys is implemented by the data of best tracks from the National Hurricane Center (NHC) and Joint Typhoon Warning Center (JTWC).

Zhang and Uhlhorn (2012) demonstrate that the orientation of hurricane wind is associated with the translation speed (U_h), V_{\max} , r^* , and storm-relative azimuth θ clockwise from the storm motion; they parameterize the inflow angle α_{SR} ($^\circ$, $= \tan^{-1}(u_r/u_t)$, where u_r and u_t are the radial and tangential wind components after removing storm motion, respectively) as

$$\alpha_{\text{SR}}(r^*, \theta, V_{\max}, U_h) = A_0 + A_1 \cos(\theta - P_1) \quad (\text{A.1})$$

The parameters A_0 , A_1 , and P_1 are

$$\begin{cases} A_0 = a_{A0}r^* + b_{A0}V_{\max} + c_{A0} \\ -\frac{A_1}{A_0} = a_{A1}r^* + b_{A1}U_h + c_{A1} \\ P_1 = a_{P1} + b_{P1}U_h + c_{P1} \end{cases}$$

The mean and standard deviation of the coefficients are $a_{A0} = -0.90 \pm 0.29$, $b_{A0} = -0.09 \pm 0.07$, $c_{A0} = -14.33 \pm 4.22$, $a_{A1} = -0.04 \pm 0.04$, $b_{A1} = 0.05 \pm 0.06$, $c_{A1} = 0.14 \pm 0.32$, $a_{P1} = 6.88 \pm 5.80$, $b_{P1} = -9.60 \pm 9.42$, and $c_{P1} = 85.31 \pm 56.86$. We use the tropical cyclones' properties (Table A.1) to compute α_{SR} in this study (Eq. A.1), and thereby the \mathbf{U}_{10} . The standard deviation of wind direction at all float positions at wind speed $> 25 \text{ m s}^{-1}$ is less than 10° , and is used to compute the uncertainty of drag coefficients.

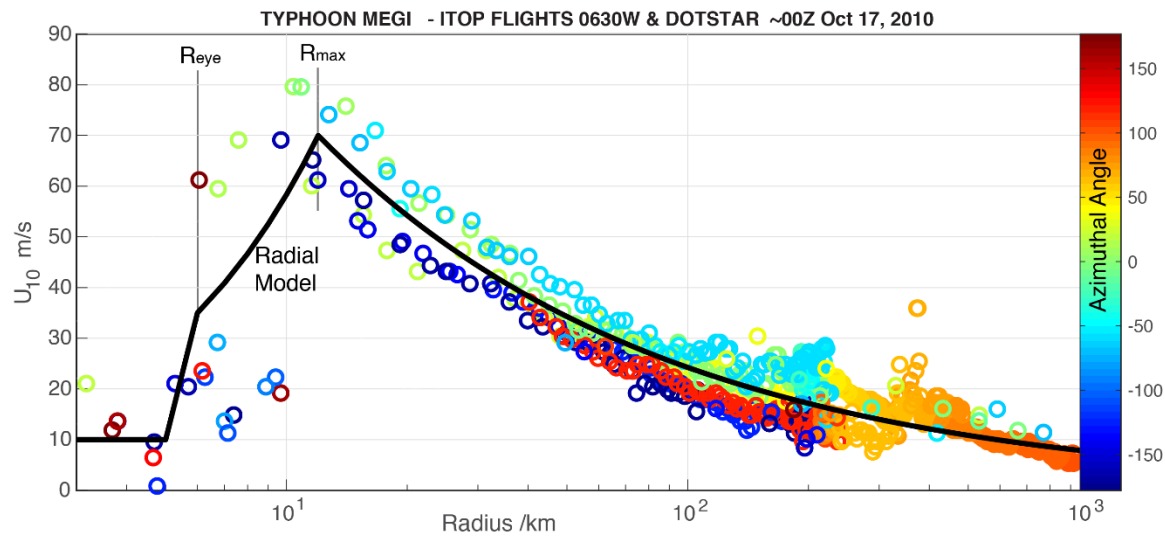


Fig. A.1. Fit of radial model (black line) to all 10-m wind speed measurements from WC-130 (630W) and DOTSTAR flights centered on 00UTC 17 October 2010. Color indicates the azimuthal angle of each measurement, clockwise from north.

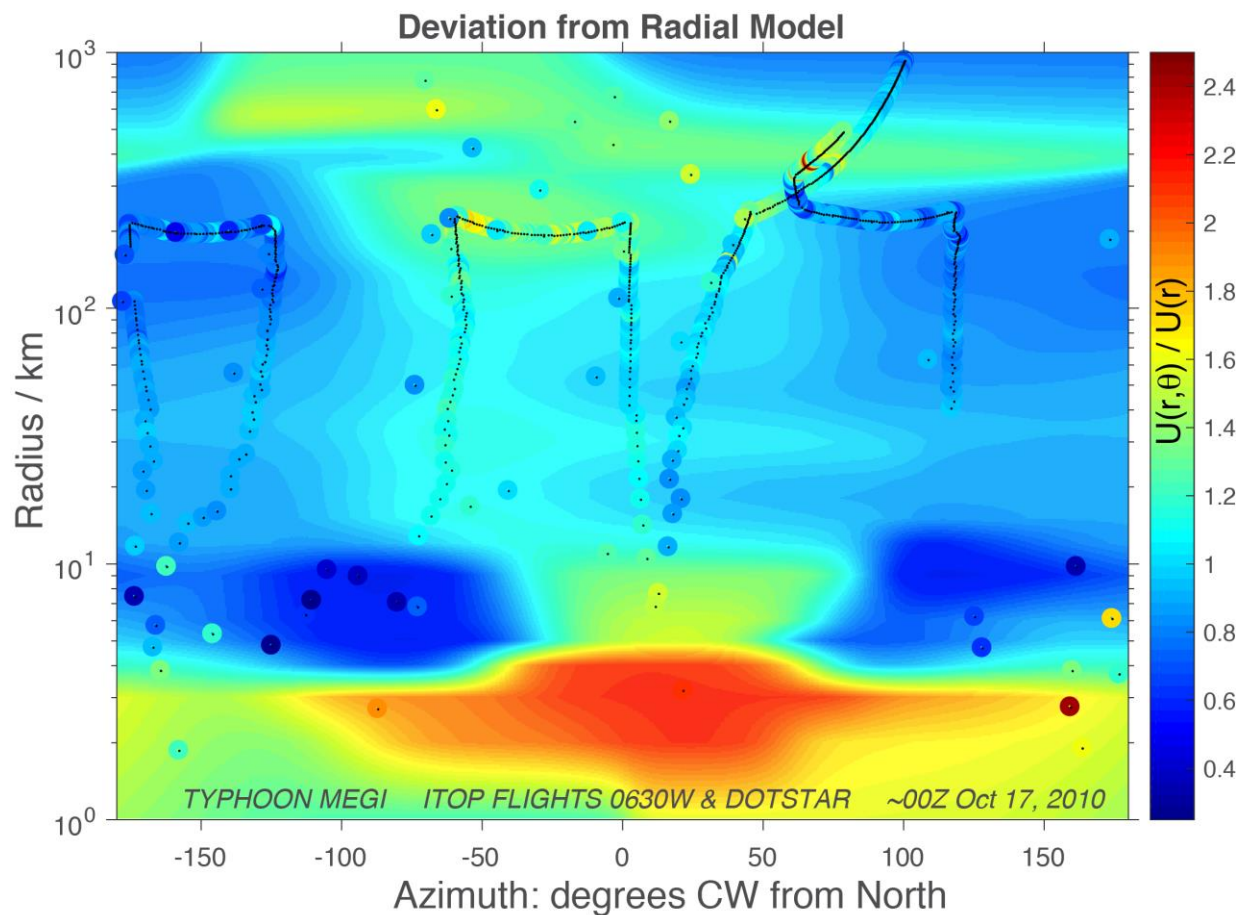


Fig. A.2. Ratio of wind speed data (colored dots) to the radial model in Fig. A.1 as a function of radius from the eye and azimuth from north. This is mapped to form a continuous function (colored).

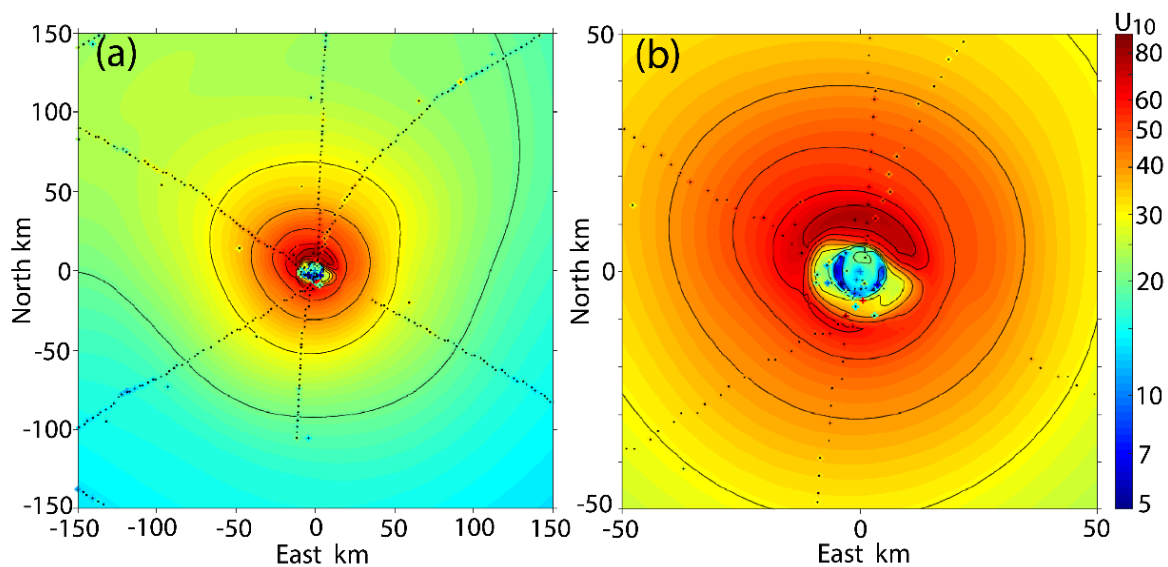


Fig. A.3. Map of wind speed at 10-m height above the sea surface $|U_{10}|$ (m s^{-1}) for 17 October 2010 aircraft surveys (630W) shown by background color with contours. Note logarithmic wind speed scale. Colored dots with black markers show measured wind speed. These are nearly invisible because they closely match the map. Map is shown at two different resolutions in the two panels.

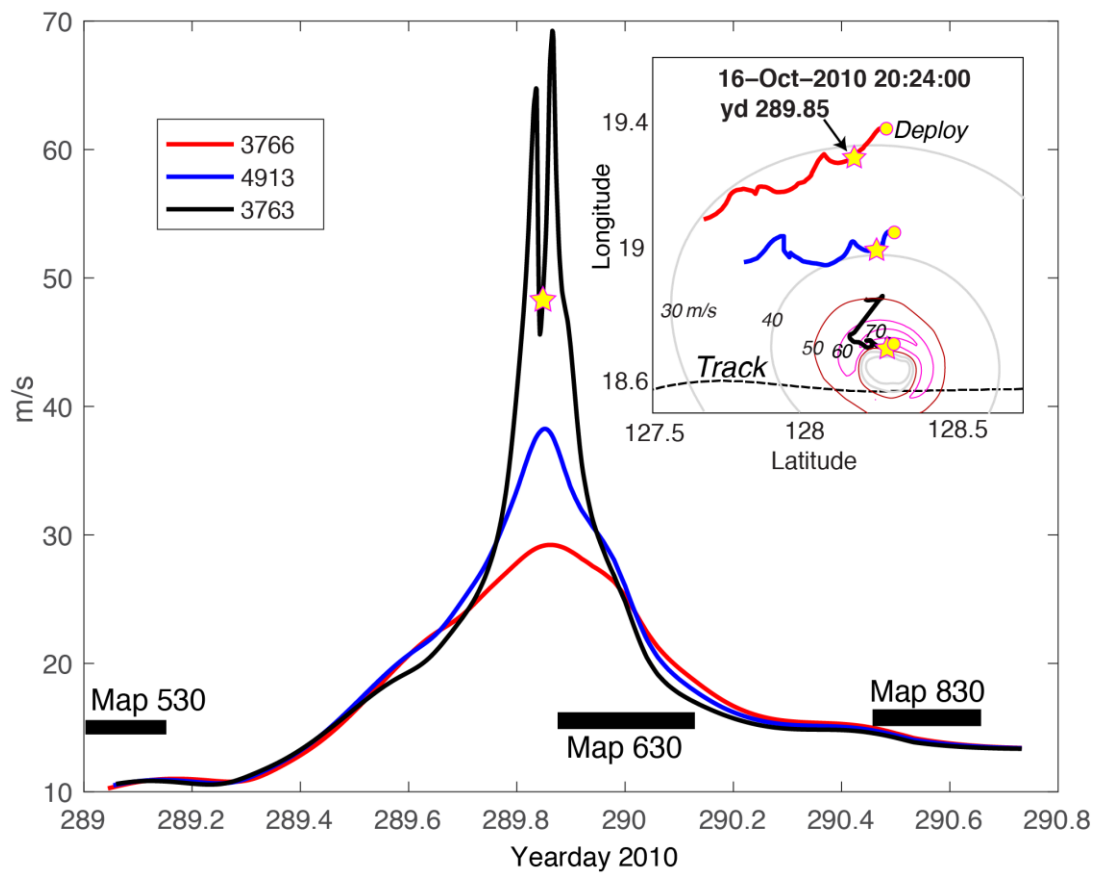


Fig. A.4. Wind speed at three EM-APEX floats. Black bars show the times of the three storm surveys interpolated to the locations of each float. The inset shows contours of the mapped wind field at the time of peak wind at the innermost float. Heavy lines show the trajectories of the three floats each starting at a yellow circle and with the position of the yellow star at the time of the inset map. Dashed line shows the storm track moving from east to west.

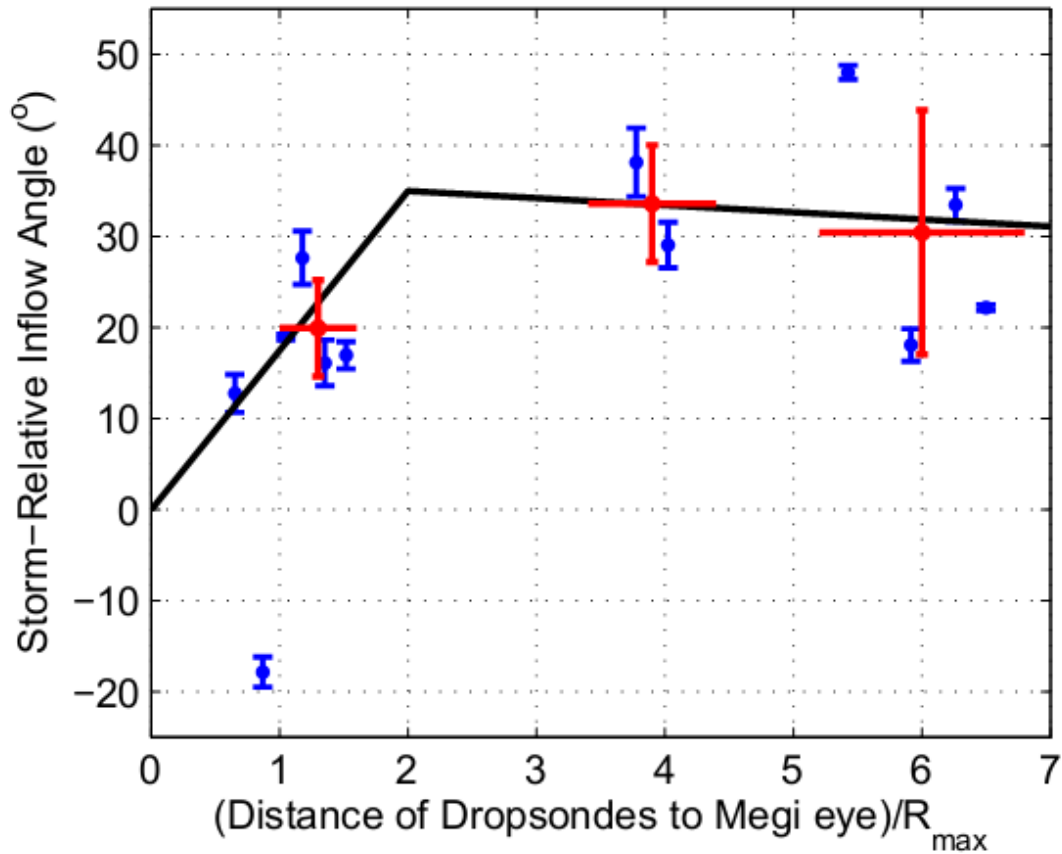


Fig. A.5. The mean and standard deviation of storm-relative inflow angle averaged between 10 and 50 m above the sea surface $\bar{\alpha}$ at the front-right quadrant of Typhoon Megi (blue dots and vertical lines) measured from dropsondes. The dependence of inflow angle on the distance to Typhoon Megi's eye is normalized by the radius of maximum wind (R_{\max}). Mean inflow angle $\bar{\alpha}$ is bin-averaged (red dots and error bars) in three bins of distance (horizontal red bars) corresponding to three EM-APEX floats' distance from Typhoon Megi's eye (em3763c, em4913a, and em3766c). The black solid line is the parameterization of storm-relative inflow angle as the function of distance to Typhoon Megi's eye used in this analysis.

Appendix B. Estimations of Wind-Driven Current Velocity on EM-APEX floats

Tides, background inertial waves, or low-frequency currents can result in the surface wind stress induced by tropical cyclones to fall out of balance with the integrated wind-driven momentum in the linear momentum budget (Eq. 2.4). The following analysis first focuses on the methods to estimate tides, background inertial waves and low-frequency currents and their corresponding uncertainties to isolate the velocity for surface wind stress estimates, and then summarizes the estimates of wind-driven current on the EM-APEX floats in all tropical cyclones.

B.1. Tides and Low-Frequency Currents in Typhoons

B.1.1. Estimation of tidal amplitude and phase

The subsurface mooring SA1, with an upward-looking 75-kHz ADCP mounted at 550-m depth, was located about 90 km west of the float array (Fig. 2.2b). The estimates of tides using the velocity measurements taken by the ADCP on the subsurface mooring SA1 are used to estimate tidal amplitude and phase at the EM-APEX floats positions in Fanapi and Megi.

We use harmonic fitting to estimate the phase and amplitude of the tides, assuming that the observed velocity is a linear superposition of mean current, inertial waves, and K1 and M2 tides. Velocity measurements on mooring SA1 show an amplitude of K1 greater than O1, and M2 greater than S2 (not shown in this study). The short time interval of velocity measurements on EM-APEX floats, ~3 days, is also not capable of separating the similar frequency signals for K1 from O1, and S2 from M2.

The harmonic analysis is applied to EM-APEX float velocity measurements between 02:00 UTC 16 October and 01:00 UTC 19 October, with an inertial period at 18–22°N of 32–38 h, and a K1 tidal period of 24 h and M2 of 12.42 h. Note that the periods of inertial waves and diurnal tides are not far apart and, therefore, estimates of diurnal tides in the linear harmonic analysis could be biased by the presence of inertial waves induced by Megi. To minimize these contamination effects on the estimates of tidal currents, we apply the harmonic analysis to the velocity data between 200 and 220-m depth, which is much deeper than the penetration depth of the storm-induced inertial waves.

Table B.1 summarizes tidal current amplitudes and phases estimated from velocity measurements taken from EM-APEX floats and on mooring SA1. The K1 on SA1 leads the K1 on the float (em4390d) at about 20.2°N by about $71 \pm 9^\circ$. Assuming the K1 tide propagates eastward from the Luzon Strait (Zhao 2014), we estimate a zonal wavelength of 310–400 km and a phase speed of 3.6–4.6 m s⁻¹. Our estimate of the phase speed agrees with the climatology K1 phase speed from AVISO satellite observations of 4–5 m s⁻¹ (Zhao 2014). Estimates of the M2 tidal phase at the float array vary greatly, presumably due to multiple M2 tide sources arriving on the experimental site, as suggested by Zhao (2014). The M2 amplitude estimates from the floats are 0.04–0.14 m s⁻¹, and are generally weaker than the K1 tide.

B.1.2. Estimation of tides assuming 1st mode baroclinic tide

We extrapolate tidal amplitude and phase estimated using EM-APEX float velocity measurements at 200–220-m depth to the layer above 200-m depth. The extrapolation depends on the vertical phase propagation and vertical structure of amplitude, which are not available from limited float measurements. The vertical structure of tidal amplitudes and vertical phase

propagation observed on mooring SA1 before the passage of typhoons (Fig. B.1) are used to guide the vertical extrapolation of tidal amplitudes and phases on EM-APEX float positions.

We divide the velocity measurements on SA1 into three layers: (A) 60–150-m depth, (B) 150–200-m depth, and (C) 200–220-m depth. The phases of diurnal and semidiurnal tides estimated on SA1 do not show significant differences between layers A and B, with a mean phase difference of ~ 0 and a standard deviation of $\sim 30^\circ$, and are independent of tidal amplitudes (Fig. B.2a and b), suggesting a vertical standing feature of diurnal and semidiurnal tides.

We extrapolate the amplitude of tides on SA1 from layer C to layer A based on the vertical structure of the 1st mode baroclinic tide. The eigen-mode structure is obtained using the density profiles taken by ARGO floats between the surface and 1600-m depth near SA1 and EM-APEX floats during 14–18 October. The difference between the tidal amplitude estimated directly from velocity in layer A and that estimated from the extrapolation from layer C is computed. Their mean values and one standard deviation of difference are computed as a function of the tidal amplitude in layer C. They vary from -0.08 to 0.05 m s^{-1} with one standard deviation about 0.03 m s^{-1} (Fig. B.2c and d). The standard deviation of amplitude within layer A is 0.02 m s^{-1} . The amplitude difference due to extrapolation (Fig. B.2c and d) is applied to the extrapolation of tidal amplitudes on EM-APEX float measurements.

B.1.3. Estimation of low-frequency currents

Because the surface geostrophic current and the barotropic adjustment velocity $\overline{\mathbf{V}^*}$ in EM-APEX float velocity measurements have longer time scales than the near-inertial current, they are assumed as depth-dependent mean current during the EM-APEX float observational period. After removing the extrapolated tides, we average float velocity vertical profiles, from the

earliest reliable and available velocity measurements to several hours (1, 2, 3, and 4 h) later, into one single profile as the mean current.

B.2. Tides, Near-Inertial waves, and Low-Frequency Currents in Hurricanes

B.2.1. Tides and inertial waves

The EM-APEX floats profiled the upper ocean for more than 12 days after the passage of Frances and Gustav. We harmonic fit tides in an every ± 2 days window, assuming a linear superposition of mean current, inertial waves (inertial period 32 h and 26.4 h in Frances and Ike, respectively), and K1 (tidal period 24 h) and M2 tides (tidal period 12.42 h). The amplitude of estimated K1 and M2 tides at $t > 4$ days (t is the time hurricane eyes passed the float positions) is mostly less than 3 cm s^{-1} between 100 and 200 m depth (not shown in this study). Tides might be negligible to the hurricane-induced current in the linear momentum budget.

We use the float measurements at $|\mathbf{U}_{10}| < 10 \text{ m s}^{-1}$ ($\sim t < -12 \text{ h}$) to harmonic fit background inertial waves, assuming a linear superposition of a background inertial wave and mean current. The profiles of a background inertial wave in Frances are fitted using the available measurements in 10, 12, or 14 h, i.e., measurements at $t = -22 - -26 \text{ h}$ to $t = -12 \text{ h}$, respectively. The earliest reliable and available measurement in Gustav is at $t = -13 \text{ h}$, which is insufficient for estimating the background inertial wave in Gustav. The profiles of background inertial waves in Ike are harmonic fitted in an every ± 1 day window using the float measurements from $t = -2.5$ day to $t = -1.5$ day. The amplitude of inertial waves within the upper 100 m in Frances and Ike are $0.12 \pm 0.04 \text{ m s}^{-1}$ and $0.10 \pm 0.04 \text{ m s}^{-1}$, respectively.

B.2.2. Low-frequency currents

The surface geostrophic current due to the sea surface height anomalies and the barotropic adjustment velocity $\overline{\mathbf{V}}^*$ in EM-APEX floats (Sanford et al. 2005) are assumed as depth-dependent mean current during the tropical cyclone forcing stage. After removing the background inertial waves in Frances and Ike, or tides in Fanapi, we average vertical profiles of current velocity from the earliest available and reliable measurements to several hours later (1, 2, 3, and 4 h), into one single profile as the mean current at each float (Hsu et al. 2017).

B.3. Estimates of Wind-Driven Current

The profiles of background inertial waves in Frances are estimated in three different fitting periods. We extrapolate the velocity of tides on the EM-APEX floats in Fanapi and Megi to the ocean surface assuming the vertical structure of the 1st mode baroclinic tide. Ten thousand realizations of normally distributed tides (K1+M2) are generated in Fanapi and Megi, using the mean and standard deviations of vertical phase propagation and amplitude difference according to the analysis of tides on mooring SA1. Ten thousand realizations of normally distributed profiles of a background inertial wave are generated in Ike, using the mean and standard deviation of estimated amplitude and phase. After removing background inertial waves or tides in each tropical cyclone except Gustav, respectively, the profiles of low-frequency current are estimated in four different selected periods.

The profiles of apparent wind-driven current \mathbf{v}_{wnd} are derived by removing the estimates of non-wind driven current velocity (12 estimates of background inertial waves plus low-frequency current in Frances; 40,000 simulations of background inertial waves plus low-frequency current in Ike; and 4 estimates of low-frequency current in Gustav; 40,000 simulations

of tides plus low-frequency current in Fanapi or Fig. B.3 in Megi) from the EM-APEX velocity profiles. The average velocity of estimated \mathbf{v}_{wnd} near the ocean surface on the right side of tropical cyclones can be more than 1.5 m s^{-1} . Most storm-induced momentum is within the upper 100 m before the passage of tropical cyclone eyes, validated by the PWP3D model simulations (Fig. 2.5 in Megi). The current velocity below 100 m depth before eye passage of Fanapi and Megi is greater than under other hurricanes (Figs. B.4 and 5), implying a more complicated background ocean current field in the western Pacific. The surface wind stress is estimated by integrating the linear momentum of \mathbf{v}_{wnd} within the upper 100 m (Chapter 3) to minimize contamination from other unknown background ocean currents.

Name	Location		K1 (Diurnal tide)				M2 (Semi-diurnal tide)			
	Lon (°E)	Lat (°N)	$A_x \left(\frac{m}{s}\right)$	$A_y \left(\frac{m}{s}\right)$	θ_x (°)	θ_y (°)	$A_x \left(\frac{m}{s}\right)$	$A_y \left(\frac{m}{s}\right)$	θ_x (°)	θ_y (°)
em3763c	128.2	18.7	0.12	0.15	137	-12.6	0.06	0.08	223.8	43.4
em4913a	128.2	19.0	0.14	0.12	195.4	39.9	0.04	0.05	170.6	-130.3
em3766c	128.1	19.3	0.11	0.12	188.2	27.6	0.07	0.12	99.5	-100.5
em4911a	128.1	19.6	0.13	0.12	165.6	0.2	0.08	0.11	109.4	-100.8
em4915a	128.1	19.8	0.11	0.10	177.9	13.0	0.05	0.07	117.5	-53.0
em4390d	128.2	20.2	0.15	0.14	169.5	3.6	0.03	0.08	193.4	10.6
Mooring	127.5	20.4	0.10	0.12	230.6	81.4	0.07	0.05	179.4	55.3
em4908a	128.2	20.8	0.12	0.12	155.8	-9.2	0.02	0.04	140.9	-74.4

Table. B.1. The estimates of amplitude and phase of K1 and M2 tides from EM-APEX float and mooring SA1 (bold) observations. The tidal function is assumed as $A \cos(\omega t + \theta)$, where A is the velocity amplitude, ω the tidal frequency, and θ the phase at $t = 0$, which is the arrival time of Typhoon Megi at the float array, about 20:30 UTC 16 October. The subscripts x and y are the zonal and meridional directions, respectively. The harmonic fitting is applied to the velocity measurements between 200 and 220 m depth from 02:00 UTC 16 October to 01:00 UTC 19 October.

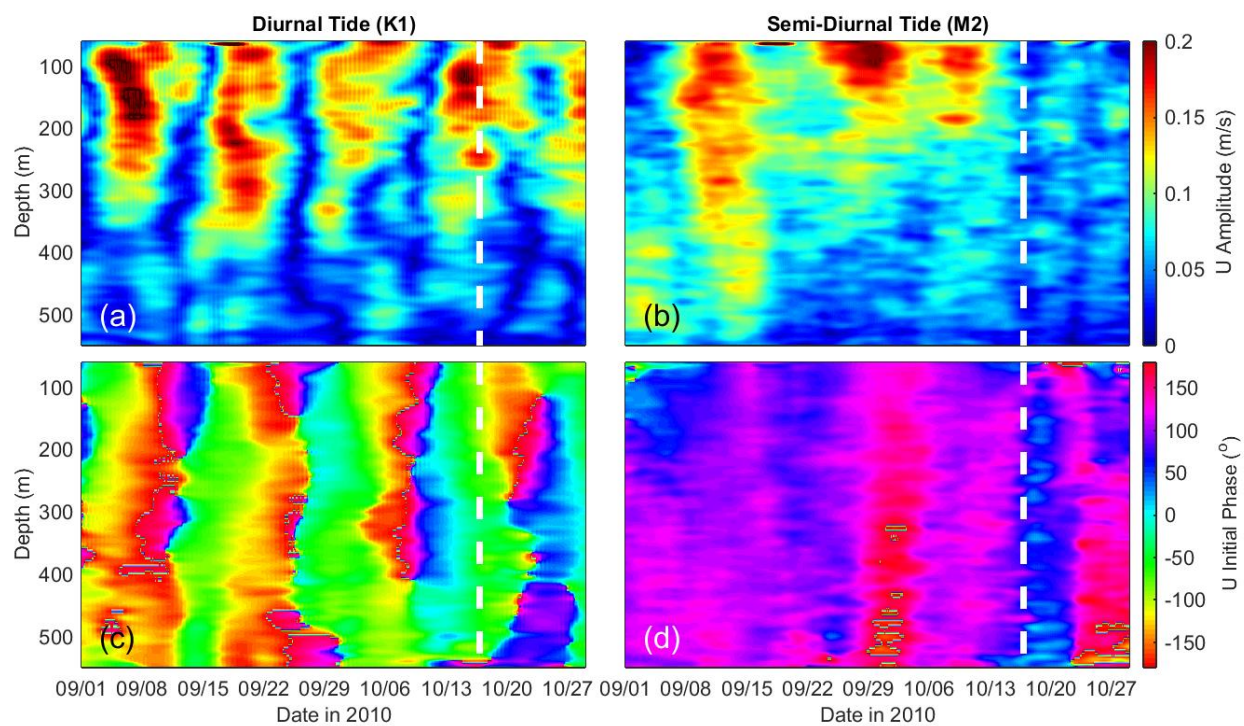


Fig. B.1. Estimates of amplitudes (top row) and phases (bottom row) of K1 (left column) and M2 (right column) tidal zonal velocity at mooring SA1. A moving window of ± 2 days is used in the harmonic analysis. The white dashed line shows the arrival time of the center of Typhoon Megi on the EM-APEX float array.

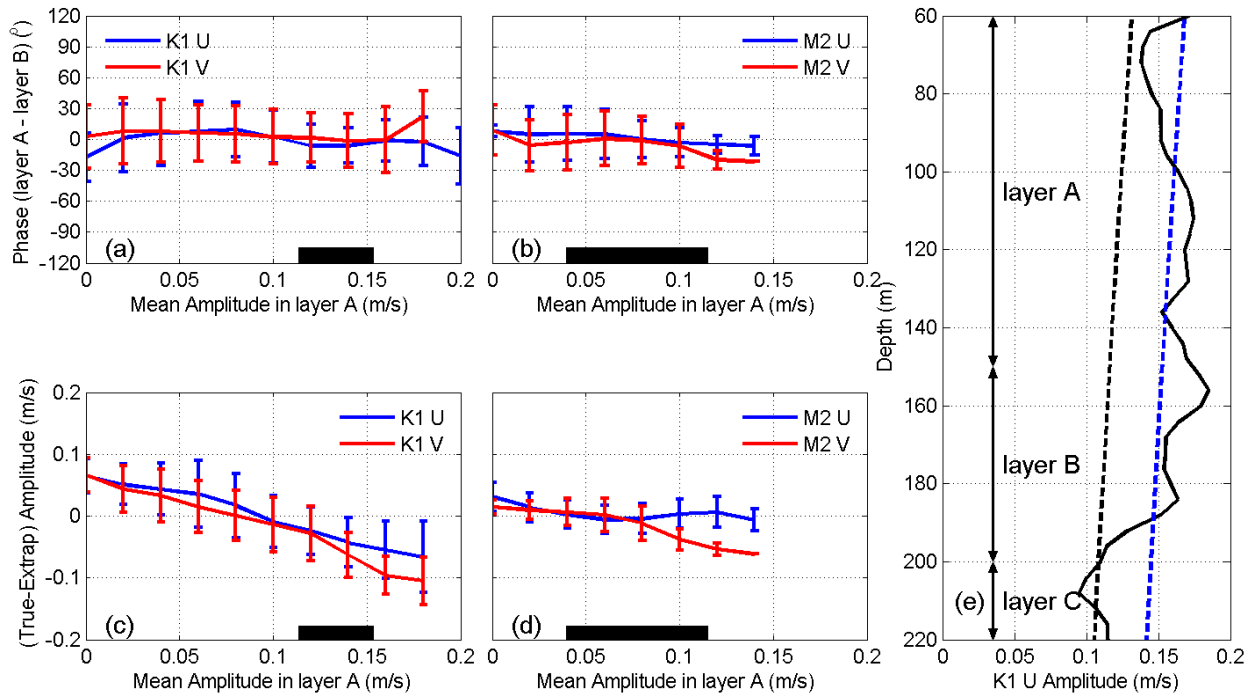


Fig. B.2. Estimates of the vertical phase propagation and the error on the extrapolation of K1 and M2 amplitude from the deeper layer (layer C) on mooring SA1 to the upper layer using ADCP velocity from April to October 2010. Panels (a) and (b) show the mean and one standard deviation of the difference of the estimated tidal phases between layers A and B, plotted as a function of tidal amplitude at 0.02 m s^{-1} interval. Panels (c) and (d) show the mean and standard deviation of the difference of the estimated tidal amplitude in layer A from that extrapolated from layer C using the 1st baroclinic modal structure. The range of tidal amplitude estimated in layer C on EM-APEX floats is indicated as the thick black horizontal bars at the bottom of (a)–(d). (e) Example of the correction of tidal amplitude extrapolation on 00:00 UTC 17 October at mooring SA1. The amplitude of the zonal velocity of the K1 tide on the mooring (black thick line) in layer C is extrapolated to layer A based on the 1st mode baroclinic tide vertical structure (black dashed line). The mean bias of amplitude between extrapolated and estimated tides within layer A is -0.03 m s^{-1} with the standard deviation 0.02 m s^{-1} .

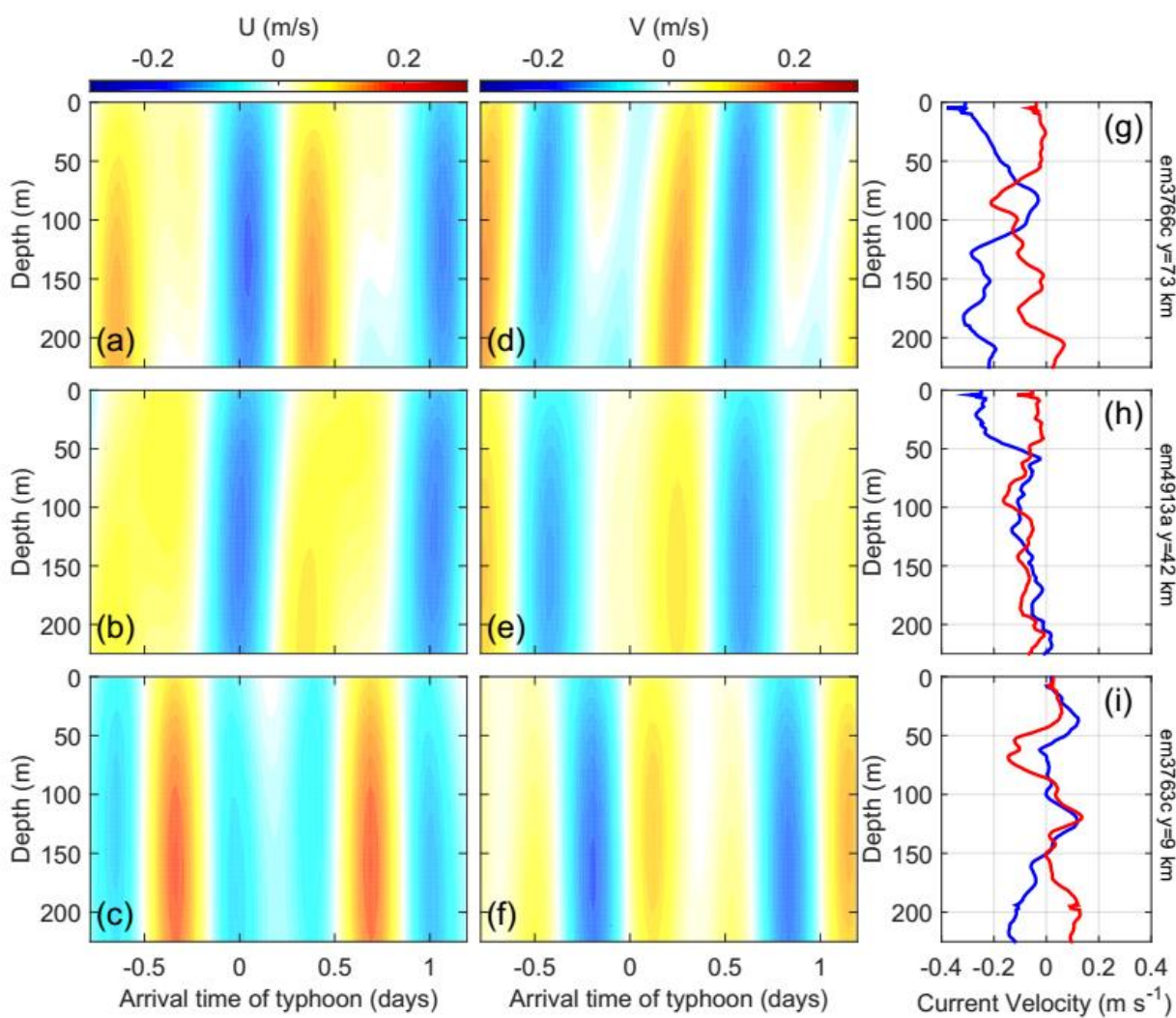


Fig. B.3. Average of tidal zonal current velocity U (left column a–c), tidal meridional current velocity V (middle column d–f), and low-frequency zonal (blue lines in right column g–i) and meridional current (red lines in right column g–i) velocity in the stochastic simulation at three float positions (rows). Distances of floats from Megi’s track are labeled to the right of the right column. Time is relative to the arrival of Typhoon Megi’s eye at the float array.

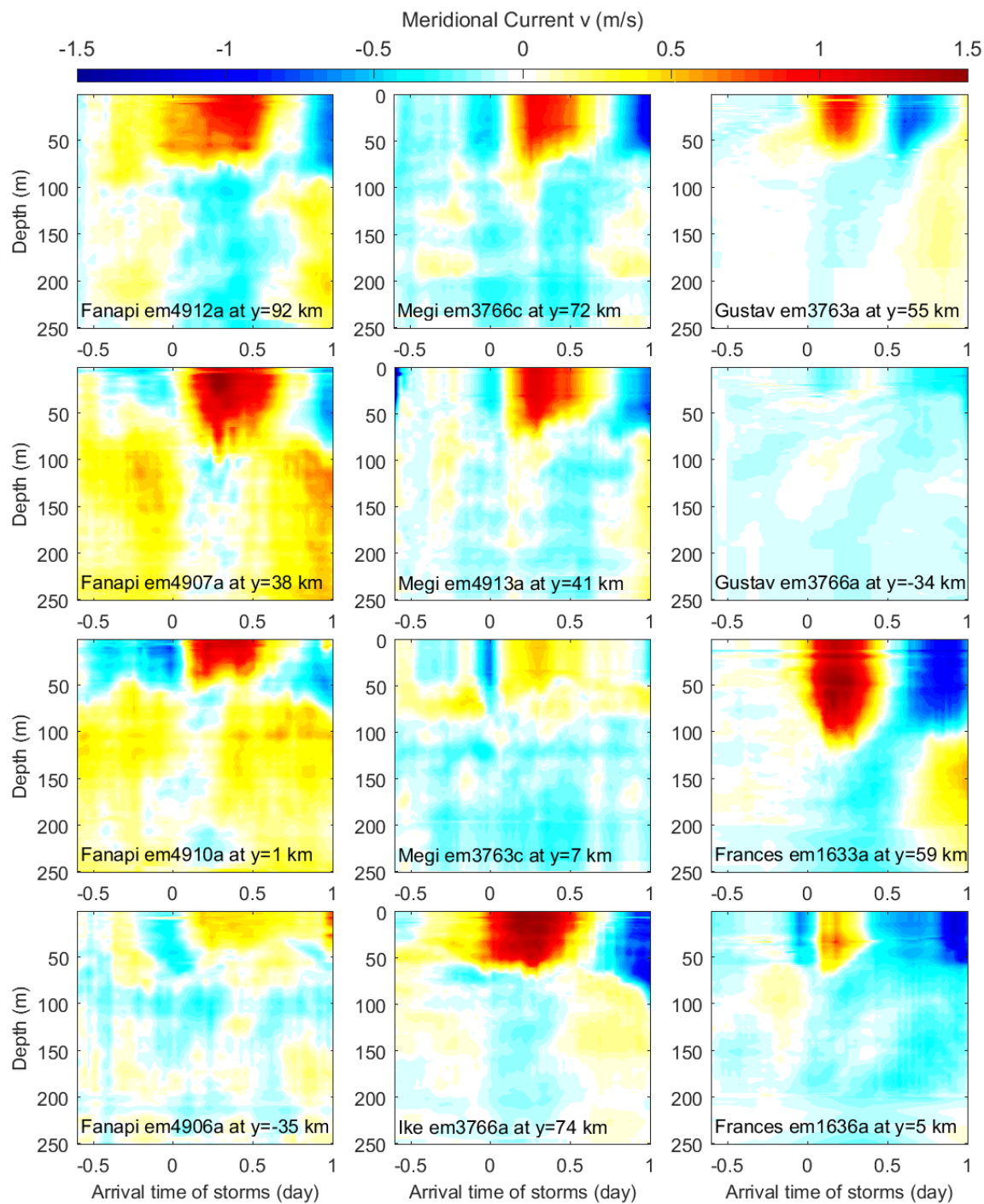


Fig. B.5. Average of estimated meridional current velocity v induced by tropical cyclone wind, as in Fig. B.4.

Appendix C. Surface Wave Velocity Variance Measured by EM-APEX Floats

C.1. Electric Current in Motional Induction in the Upper Ocean

C.1.1. Electric current induced by a moving medium in the Earth's geomagnetic field

Sanford et al. (1971) describe the electric current in a moving medium as

$$\mathbf{J} = \sigma(\mathbf{E} + \mathbf{V} \times \mathbf{B}) \quad (\text{C.1})$$

The electric current \mathbf{J} is driven by two voltage sources: $\mathbf{V} \times \mathbf{B}$ the motional induction resulting from the ocean current (Longuet-Higgins et al. 1954) and the background electric field \mathbf{E} (Table 4.1).

Based on the Maxwell–Faraday equation, the electric field \mathbf{E} in a moving medium (Eq. C.1) is the gradient of electrical potential Φ modulated by the temporal variation of the magnetic field ($\frac{\partial \mathbf{a}}{\partial t}$) in the ocean (Sanford 1971), i.e.,

$$\mathbf{E} = -\nabla\Phi - \frac{\partial \mathbf{a}}{\partial t} \quad (\text{C.2})$$

where the gradient operator $\nabla = \frac{\partial}{\partial x} \hat{\mathbf{i}} + \frac{\partial}{\partial y} \hat{\mathbf{j}} + \frac{\partial}{\partial z} \hat{\mathbf{k}}$.

Following Ampere's law (Sanford 1971; Podney et al. 1975), the magnetic potential vector \mathbf{a} is primarily associated with the electric current \mathbf{J} , assuming the aspect ratio of the ocean is $\ll O(1)$, i.e.,

$$\nabla \times (\nabla \times \mathbf{a}) \approx \mu \mathbf{J} \quad (\text{C.3})$$

We assume the ambient magnetic field \mathbf{B} in the ocean consists primarily of the Earth geomagnetic field ($\mathbf{F} = F_y \hat{\mathbf{j}} + F_z \hat{\mathbf{k}}$) and the electromagnetic field \mathbf{b} as

$$\mathbf{B} = \mathbf{F} + \mathbf{b} \quad (\text{C.4})$$

The electromagnetic field \mathbf{b} is the curl of \mathbf{a} as $\mathbf{b} = \nabla \times \mathbf{a}$.

Substituting Eqs. (C.2) to (C.4) into Eq. (C.1), the electric current modulated by the electromagnetic field is

$$\frac{\mathbf{J}}{\sigma} = -\nabla\Phi + \mathbf{V} \times (\mathbf{F} + \mathbf{b}) - \frac{\partial\mathbf{a}}{\partial t} \quad (\text{C.5})$$

Note that both \mathbf{a} and \mathbf{b} are functions of \mathbf{J} .

C.1.2. Motional induction of surface waves in a moving medium

In Eq. (C.5), the \mathbf{J} induced by surface waves is modulated by the temporal variation of magnetic vector potential $\frac{\partial\mathbf{a}}{\partial t}$ associated with the wave-induced electric current (Eq. C.3) and the motional induction of surface waves in the electromagnetic field $\mathbf{V}_{\text{sgw}} \times \mathbf{b}$, where \mathbf{V}_{sgw} is the velocity of surface waves in the deep water. The $\left(-\frac{\partial\mathbf{a}}{\partial t} + \mathbf{V}_{\text{sgw}} \times \mathbf{b}\right) \ll \left(-\nabla\Phi + \mathbf{V}_{\text{sgw}} \times \mathbf{F}\right)$ is shown in the following analysis, i.e.,

$$\frac{\mathbf{J}}{\sigma} \approx -\nabla\Phi + \mathbf{V}_{\text{sgw}} \times \mathbf{F} \quad (\text{C.6})$$

We perform the perturbation analysis of Eq. (C.5) following Sanford (1971). The electric current induced by the motional induction of surface waves is the first order term $\mathbf{J}^{(1)}$ (Longuet-Higgins et al. 1954). i.e.,

$$\frac{\mathbf{J}^{(1)}}{\sigma} = -\nabla\Phi + \mathbf{V}_{\text{sgw}} \times \mathbf{F} \quad (\text{C.7})$$

The higher order electric current $\mathbf{J}^{(n)}$ is the sum of the first order of electric current $\mathbf{J}^{(1)}$ and the correction of electric current $\Delta\mathbf{J}^{(n)}$, i.e.,

$$\mathbf{J}^{(n)} = \mathbf{J}^{(1)} + \Delta\mathbf{J}^{(n)}; \text{ for } n \geq 2$$

The correction of electric current $\Delta\mathbf{J}^{(n+1)}$ caused by the electromagnetic field's temporal variation $\frac{\partial(\mathbf{a}^{(n+1)})}{\partial t}$ and motional induction in $\mathbf{b}^{(n+1)}$ is associated with $\mathbf{J}^{(n)}$ following Ampere's law (Sanford 1971), i.e.,

$$\begin{aligned} \Delta\mathbf{J}^{(n+1)} &= \sigma \left(-\frac{\partial(\mathbf{a}^{(n+1)})}{\partial t} + \mathbf{V}_{\text{sgw}} \times \mathbf{b}^{(n+1)} \right) \\ &= \sigma \left(-\frac{\partial}{\partial t} \int \int \int (\mu\mathbf{J}^{(n)}) \, dx \, dy \, dz + \mathbf{V}_{\text{sgw}} \times \int (\mu\mathbf{J}^{(n)}) \, dl \right); \text{ for } n \geq 1 \end{aligned} \quad (\text{C.8})$$

where l is the length scale of surface waves over a surface wave period.

We assume that $\mathbf{a}^{(1)}$ and $\mathbf{b}^{(1)}$ are zero (Sanford 1971). The higher order $\mathbf{a}^{(n+1)}$ and $\mathbf{b}^{(n+1)}$ are computed using $\mathbf{J}^{(n)}$ following Eq. (C.8). The surface wave is assumed propagating in the zonal direction to simplify the following scale analysis. Based on the linear wave theory, the horizontal and vertical scale of electric current induced by surface waves should be proportional to the inverse wavenumber k^{-1} of surface waves, and the temporal scale should be inversely proportional to the surface wave frequency ω . The magnitude of the corresponding correction on the second order of electric current $\Delta\mathbf{J}^{(2)}$ is

$$\begin{aligned} |\Delta\mathbf{J}^{(2)}| &= \sigma \left| -\frac{\partial\mathbf{a}^{(2)}}{\partial t} + \mathbf{V}_{\text{sgw}} \times \mathbf{b}^{(2)} \right| \\ &= \sigma \left(-\frac{\partial}{\partial t} \left| \int \int \int (\mu\mathbf{J}^{(1)}) \, dx \, dy \, dz \right| + \left| \mathbf{V}_{\text{sgw}} \times \int \mu\mathbf{J}^{(1)} \, dl \right| \right) \approx m |\mathbf{J}^{(1)}| \end{aligned}$$

where $m = \sigma\mu \left(-\frac{\omega}{k^2} + \frac{A}{k} \right)$ and A the surface wave velocity amplitude (Table 4.1). The scale of

$|\Delta\mathbf{J}^{(n)}|$ can be expressed as

$$|\Delta \mathbf{J}^{(n)}| \approx |\mathbf{J}^{(1)}| \sum_{i=2}^n m^{(i-1)} = |\mathbf{J}^{(1)}| \frac{m^n - m}{m-1}; n \geq 2 \quad (\text{C.9})$$

The higher order correction of electric current due to the time variation of the electromagnetic field $|\Delta \mathbf{J}^{(n)}|$ (Eq. C.9) relative to the first order electric current $|\mathbf{J}^{(1)}|$ (Eq. C.7) is

$$\frac{|\Delta \mathbf{J}^{(n)}|}{|\mathbf{J}^{(1)}|} \approx \frac{|\mathbf{J}^{(1)}| \frac{m^n - m}{m-1}}{|\mathbf{J}^{(1)}|} = \frac{m^n - m}{m-1}; n \geq 2$$

The seawater's conductivity σ is $\sim 4 \text{ mho m}^{-1}$, $\mu \sim 4\pi \times 10^{-7} \text{ henry m}^{-1}$. Under tropical cyclones, the wave frequency $\omega/2\pi \sim 0.07 - 0.2 \text{ Hz}$ (e.g., Collins et al. 2014), the wave height in deep water $\eta = A/\omega$ (Young 1998) is less than 20 m, the wavelength ($\lambda=2\pi/k$) $\sim 100 - 300 \text{ m}$, i.e., $\sigma\mu \frac{\omega}{k^2} \approx O(10^{-4})$, $\sigma\mu \frac{\eta\omega}{k} \ll O(10^{-3})$, and $\frac{|\Delta \mathbf{J}^{(n)}|}{|\mathbf{J}^{(1)}|} \ll 1$. The correction of the electromagnetic field induced by surface waves on the wave-induced electric current is negligible, as suggested by Weaver (1965) and Lilley et al. (2004). That is, the electric current induced by a single surface wave (Eq. C.6) is in the same form as the electric current induced by a low-frequency current (Eq. 4.1).

C.1.3. Electric current induced by a low-frequency current

Sanford et al. (1978) describe the electric current $\mathbf{J} = J_x \hat{\mathbf{i}} + J_y \hat{\mathbf{j}}$ induced by a low-frequency ($< 0.02 \text{ Hz}$) current $\mathbf{u} = u \hat{\mathbf{i}} + v \hat{\mathbf{j}}$ (Eq. 9 in Sanford et al. 1978), assuming the aspect ratio of oceanic current $\ll O(1)$ and excluding the effect of high-frequency surface waves. i.e.,

$$\begin{cases} \frac{J_x}{\sigma} = F_z v + \overline{\left(\frac{J_x}{\sigma}\right)^*} \\ \frac{J_y}{\sigma} = -F_z u + \overline{\left(\frac{J_y}{\sigma}\right)^*} \end{cases} \quad (\text{C.10})$$

where $\overline{\left(\frac{J_x}{\sigma}\right)^*} = \overline{\left(\frac{J_x}{\sigma}\right)} - F_z \overline{v^*}$, $\overline{\left(\frac{J_y}{\sigma}\right)^*} = \overline{\left(\frac{J_y}{\sigma}\right)} + F_z \overline{u^*}$, $\overline{\mathbf{V}^*} = \overline{u^*} \hat{\mathbf{i}} + \overline{v^*} \hat{\mathbf{j}}$ is a depth-independent term, equivalent to $\nabla\Phi(-H)$ at the sea floor (Sanford et al. 1978), and $\overline{\left(\frac{\mathbf{J}}{\sigma}\right)} = \overline{\left(\frac{J_x}{\sigma}\right)} \hat{\mathbf{i}} + \overline{\left(\frac{J_y}{\sigma}\right)} \hat{\mathbf{j}}$ represents all other depth-independent terms except $\overline{\mathbf{V}^*}$ (Sanford 1971), which is often assumed negligible compared to other terms (Sanford et al. 1978).

C.1.4. Electric current induced by a surface wave

In linear wave theory, the surface wave velocity \mathbf{V}_{sgw} in the deep ocean can be expressed (Young 1999) as

$$\begin{aligned} \mathbf{V}_{\text{sgw}} &= u_{\text{sgw}} \hat{\mathbf{i}} + v_{\text{sgw}} \hat{\mathbf{j}} + w_{\text{sgw}} \hat{\mathbf{k}} \\ &= A(\sin \psi \cos \theta \hat{\mathbf{i}} + \sin \psi \sin \theta \hat{\mathbf{j}} - \cos \psi \hat{\mathbf{k}}) e^{kz} \end{aligned} \quad (\text{C.11})$$

$$\psi = k_x x + k_y y - \omega t + \phi_0; \quad \theta = \tan^{-1} \frac{k_y}{k_x} \quad \text{and} \quad k = (k_x^2 + k_y^2)^{\frac{1}{2}}$$

where $A = \sigma_{u0}^2/2$ is the horizontal velocity amplitude of the surface wave at the ocean surface, σ_{u0}^2 the horizontal velocity variance of surface wave at the ocean surface, ψ the phase of the surface wave, ω the angular frequency, θ the propagation direction counterclockwise rotation from the east, ϕ_0 the initial surface wave phase (at $x = 0$, $y = 0$ and $t = 0$), z the depth, and k the wavenumber magnitude.

To derive the solution of electrical potential Φ induced by a surface wave, we first assume that the conductivity σ in the upper ocean is locally uniform, $\nabla(1/\sigma) = 0$, and the conservation of electric current \mathbf{J} , $\nabla \cdot \mathbf{J} = 0$ (Longuet-Higgins et al. 1954). The curl of Earth's geomagnetic field is $\nabla \times \mathbf{F} = 0$ in the upper ocean according to Maxwell's equations, because \mathbf{F}

originates at the core of the Earth. Because the surface wave is irrotational ($\nabla \times \mathbf{V}_{\text{sgw}} = 0$), the gradient of Eq. (4.1) in the upper ocean becomes

$$\nabla^2 \Phi = \nabla \cdot \left(\mathbf{V}_{\text{sgw}} \times \mathbf{F} - \frac{\mathbf{J}}{\sigma} \right) = (\nabla \times \mathbf{V}_{\text{sgw}}) \cdot \mathbf{F} - \mathbf{V}_{\text{sgw}} \cdot (\nabla \times \mathbf{F}) - \nabla \cdot \left(\frac{\mathbf{J}}{\sigma} \right) = 0 \quad (\text{C.12})$$

where the gradient operator $\nabla = \frac{\partial}{\partial x} \hat{\mathbf{i}} + \frac{\partial}{\partial y} \hat{\mathbf{j}} + \frac{\partial}{\partial z} \hat{\mathbf{k}}$. Surface waves decay exponentially with depth, so that Φ generated by surface waves at $z = -\infty$ is assumed negligible. The general solution of Φ has the exponential form e^{kz} .

At the ocean surface, the component of electric current normal to the ocean surface is zero (Longuet-Higgins et al. 1954). i.e.,

$$\mathbf{J} \cdot \hat{\mathbf{n}} = 0 \text{ at } z = \eta$$

where $\hat{\mathbf{n}}$ is the unit vector normal to the ocean surface, and $z = \eta$ the ocean surface. The ratio of the wave height to wavelength is typically less than $O(0.1)$ (e.g., Wright et al. 2001; Hu et al. 2011), or wave breaking will occur (Donelan et al. 2004). We assume $\hat{\mathbf{n}} \approx \hat{\mathbf{k}}$ and

$$J_z \approx 0 \text{ at } z = 0$$

The boundary condition at the sea surface can be assumed using the vertical components of Eq. (4.1) as

$$\frac{\partial \Phi}{\partial z} \approx F_y u_{\text{sgw}} \text{ at } z = 0 \quad (\text{C.13})$$

Because a surface wave decays exponentially in depth, the induced Φ at $z = -\infty$ is assumed negligible, i.e.,

$$\Phi(z = -\infty) \approx 0 \quad (\text{C.14})$$

Using Eqs. (C.11–14), the Φ induced by a surface wave is

$$\Phi = \frac{1}{k} F_y (A \sin \psi \cos \theta e^{kz}) \quad (\text{C.15})$$

Substituting Eqs. (C.11) and (C.15) into Eq. (4.1), the components of electric current induced by a surface wave become

$$\begin{cases} \frac{J_x}{\sigma} = F_z v_{sgw} - F_y w_{sgw} - \frac{\partial \Phi}{\partial x} = A \sin \theta (F_z \sin \psi + F_y \cos \psi \sin \theta) e^{kz} & \text{(a)} \\ \frac{J_y}{\sigma} = -F_z u_{sgw} - \frac{\partial \Phi}{\partial y} = -A \cos \theta (F_z \sin \psi + F_y \cos \psi \sin \theta) e^{kz} & \text{(b)} \\ \frac{J_z}{\sigma} = F_y u_{sgw} - \frac{\partial \Phi}{\partial z} = 0 & \text{(c)} \end{cases} \quad (\text{C.16})$$

The vertical electric current induced by the surface wave is zero. The above equations can be simplified as

$$\mathbf{J}/\sigma = \sqrt{2} \sigma_{u0} F_z \sqrt{1 + \beta^2} \sin \psi_\omega (\sin \theta \hat{\mathbf{i}} - \cos \theta \hat{\mathbf{j}}) e^{kz} \quad (\text{C.17})$$

where $\psi_\omega = \psi + \tan^{-1}(\beta)$ and $\beta = \frac{F_y}{F_z} \sin \theta$.

C.2. Voltage Measurements and Data Processing on EM-APEX floats

C.2.1. Voltage measurements on autonomous drifting floats

EM-APEX floats are designed to drift freely with the seawater horizontally. If the float velocity \mathbf{V}_{EM} is the same as seawater \mathbf{V} , the electric field around the float ($-\nabla \Phi_{EM}$) is (Sanford et al. 1978)

$$\nabla \Phi_{EM} = (\mathbf{V}_{EM} - \mathbf{V}) \times \mathbf{F} - \frac{\tilde{\mathbf{J}}}{\sigma} \approx -\frac{\tilde{\mathbf{J}}}{\sigma} \quad (\text{C.18})$$

$$\tilde{\mathbf{J}} = (1 + C_1) \mathbf{J} \quad (\text{C.19})$$

where \mathbf{J} is the electric current induced by the motion of seawater, and $\tilde{\mathbf{J}}$ is the electric current measured on the float, modified by the floats' physical presence. The float's insulated outer surface stretches the path of electric current and its shape enhances the electrical potential density lead to a head factor C_1 (Sanford et al. 1978). The C_1 is ~ 0.5 for EM-APEX floats, as determined in the laboratory by comparing the voltage measurements in a water tank taken by

EM-APEX floats and a T bar, which is a simple pair of electrodes. We assume its physical presence does not affect the electric current \mathbf{J} , i.e., $C_1 = 0$ for T bar.

EM-APEX floats profile vertically at a vertical component of velocity w_{EM} relative to the surrounding water by adjusting the floats' buoyancy. The vertical motion generates a zonal component of electrical current as $F_y(1 + C_2)w_{EM}\hat{\mathbf{i}}$, where the head factor C_2 is -0.2 (Sanford et al. 1978). Therefore, the electric field around the EM-APEX float is expressed as

$$\nabla\Phi_{EM} \approx \left(F_y(1 + C_2)w_{EM} - (1 + C_1)\frac{J_x}{\sigma} \right) \hat{\mathbf{i}} - (1 + C_1)\frac{J_y}{\sigma} \hat{\mathbf{j}} \quad (\text{C.20})$$

C.2.2. Voltage measurements on the rotating electrodes

Two orthogonal pairs of Ag-AgCl electrodes, termed E_1 and E_2 pairs, are equipped on the EM-APEX floats to take voltage measurements (Fig. 4.2). Float voltage measurements $\Delta\Phi_i$ ($i = 1$ for E_1 pair and $i = 2$ for E_2 pair) consist primarily of the projections of the electric field on the electrodes ($-\nabla\Phi_{EM}$, expressed in Eq. C.20), a trend $\Delta\Phi_{i\text{trend}}$ due to the vertical variations of salinity and temperature, an unknown constant offset $\Delta\Phi_{i\text{offset}}$, and instrumental noise $\Delta\Phi_{i\text{noise}}$ (Sanford et al. 1978). i.e.,

$$\begin{aligned} \frac{\Delta\Phi_i}{L} = & \left(F_y(1 + C_2)w_{EM} - (1 + C_1)\left(\frac{J'_x}{\sigma} + \frac{\bar{J}_x}{\sigma}\right) \right) \cos \theta_\Omega - (1 + C_1)\left(\frac{J'_y}{\sigma} + \frac{\bar{J}_y}{\sigma}\right) \sin \theta_\Omega \\ & + \frac{\Delta\Phi_{i\text{trend}}}{L}t + \frac{\Delta\Phi_{i\text{offset}}}{L} + \frac{\Delta\Phi_{i\text{noise}}}{L} \end{aligned} \quad (\text{C.21})$$

where L is the distance between electrodes, the angle of electrode pair from the geomagnetic east is $\theta_\Omega = \Omega t + \phi_i$, Ω is the angular rotation frequency of EM sensors, t is the time, and ϕ_i the orientation of the pair of electrodes at $t = 0$. \bar{J}_x and \bar{J}_y are electrical currents induced by the low-

frequency current (< 0.02 Hz), and J'_x and J'_y are electrical currents induced by surface gravity waves (> 0.02 Hz).

C.2.3. Voltage measurements associated with low-frequency electric currents

Low-frequency electric currents $\bar{\mathbf{J}}$ taken by the EM-APEX floats are obtained by least-squared fitting $\Delta\Phi_i$ (Eq. C.21) in 50-s data windows, where the direction of EM sensors $\theta_\Omega (= \Omega t + \phi_i)$ is determined using the float's magnetometer measurements (e.g., Sanford et al. 1978; Sanford et al. 2005), i.e.,

$$\frac{\Delta\Phi_i}{L} = a_1^i \cos \theta_\Omega + a_2^i \sin \theta_\Omega + a_3^i t + a_4^i + \epsilon^i ; \text{ for } i = 1, 2 \quad (\text{C.22})$$

$$\begin{cases} a_1^i = -\frac{\bar{J}_x}{\sigma} (1 + C_1) + F_y (1 + C_2) w_{EM} \\ a_2^i = -\frac{\bar{J}_y}{\sigma} (1 + C_1) \\ a_3^i = \frac{\Delta\Phi_{i,trend}}{L} \\ a_4^i \approx -(1 + C_1) \langle \chi_i \rangle + \frac{\Delta\Phi_{i,offset}}{L} \\ \epsilon^i = -(1 + C_1) (\chi_i - \langle \chi_i \rangle) + \frac{\Delta\Phi_{i,noise}}{L} \end{cases}$$

where $a_1^i - a_4^i$ are the fitting coefficients on each pair of electrodes E_i , ϵ^i the residuals, $\chi_i = \frac{J'_x}{\sigma} \cos \theta_\Omega + \frac{J'_y}{\sigma} \sin \theta_\Omega$, $\mathbf{J}' = J'_x \hat{\mathbf{i}} + J'_y \hat{\mathbf{j}}$ the electric current induced by surface waves (Table 4.1), and $\langle \rangle$ represents the average over a 50-s fitting window. Note that because the surface wave period is typically much shorter than 50 s, only the electrical currents \bar{J}_x and \bar{J}_y induced by low-frequency oceanic currents are fitted in the 50-s data windows. The constant offset a_4^i may include effects of surface waves if $\langle \chi_i \rangle$ is not negligible (Appendix C.2.4). Because the sampling rate of voltage measurements is 1 Hz (Chapter 4), the residuals ϵ^i contain all signals of voltage

with frequency from 0.02 to 1 Hz, often used to compute the Verr in the float measurements (Appendix C.2.4).

Most voltage measurements are from the constant offset $\Delta\Phi_{i\text{offset}}$ (blue line in Fig. C.1). The rotation of pairs of the electrodes on EM-APEX floats in Eq. (C.21) is required to separate the voltage measurements induced by the seawater motion from the trend and offset (green line in Fig. C.1). The residuals ϵ^i are the discrepancy between the voltage measurements and least-squared fitted results (difference between the black and red lines in Fig. C.1).

C.2.4. Subsurface float measurements of velocity variance

The residuals ϵ^i (Eq. C.22) are often used to compute the output of Verr in the float measurements as $\text{Verr} = \sqrt{\langle \epsilon^{i^2} \rangle / (1 + C_1)^2 F_z^2 / N}$, where $N = 50$ is the number of voltage measurements in each 50-s harmonic fitting window. The measured velocity variance $\widetilde{\sigma}_u^2$ on each pair of electrodes is computed using the Verr as

$$\widetilde{\sigma}_u^2 = N(\text{Verr})^2 = \frac{\langle \epsilon^{i^2} \rangle}{(1+C_1)^2 F_z^2} \approx \frac{\langle \chi_i^2 \rangle - \langle \chi_i \rangle^2}{F_z^2} + \delta_i^2; \text{ for } i=1 \text{ or } 2 \quad (\text{C.23})$$

where $\langle \quad \rangle$ represents the average over a 50-s fitting window, the instrumental noise on the

electrodes $\delta_i^2 = \frac{(\frac{\Delta\Phi_{i\text{noise}}}{L})^2}{F_z^2(1+C_1)^2}$ and $\chi_i = \frac{J'_x}{\sigma} \cos \theta_\Omega + \frac{J'_y}{\sigma} \sin \theta_\Omega$. The term $\chi_i = \frac{J'_x}{\sigma} \cos \theta_\Omega + \frac{J'_y}{\sigma} \sin \theta_\Omega$ can

be rewritten using Eq. (4.3) as

$$\chi_i = \sqrt{2}\sigma_{u0}\sqrt{1 + \beta^2 F_z} e^{kz} \sin \psi_\omega \sin \psi_\Omega \quad (\text{C.24})$$

where $\theta_\Omega = \Omega t + \phi_i$ is the orientation of electrodes, and $\psi_\Omega = \theta - \theta_\Omega$ the angle difference between surface wave propagation direction and electrodes. Because the surface wave period

under tropical cyclones is usually < 50 s (e.g., Collins III et al. 2014), the averages of $\cos \psi_\omega$ and $\cos(\psi_\omega + \psi_\Omega)$ in the 50-s data window are

$$\langle \cos \psi_\omega \rangle = \langle \cos(\psi_\omega + \psi_\Omega) \rangle \approx 0 \quad (\text{C.25})$$

Substituting Eqs. (C.24) and (C.25) into the $\langle \chi_i^2 \rangle$ and $\langle \chi_i \rangle^2$ in Eq. (C.23),

$$\begin{aligned} \frac{\langle \chi_i^2 \rangle}{F_z^2(1+\beta^2)\sigma_{u0}^2 e^{2kz}} &= 2\langle \sin^2 \psi_\omega \sin^2 \psi_\Omega \rangle = \frac{1}{2}\langle (1 - \cos 2\psi_\omega)(1 - \cos 2\psi_\Omega) \rangle \\ &\approx \frac{1}{2}\left(\frac{1}{2} + \langle \cos^2(\psi_\omega - \psi_\Omega) \rangle - \langle \cos 2\psi_\Omega \rangle\right) \end{aligned}$$

$$\begin{aligned} \frac{\langle \chi_i \rangle^2}{F_z^2(1+\beta^2)\sigma_{u0}^2 e^{2kz}} &= 2\langle \sin \psi_\omega \sin \psi_\Omega \rangle^2 = \frac{1}{2}\langle \cos(\psi_\omega - \psi_\Omega) - \cos(\psi_\omega + \psi_\Omega) \rangle^2 \\ &\approx \frac{1}{2}\langle \cos(\psi_\omega - \psi_\Omega) \rangle^2 \end{aligned}$$

the $\widetilde{\sigma}_u^2$ becomes

$$\widetilde{\sigma}_u^2 \approx \frac{\sigma_{u0}^2}{2} \left(\frac{1}{2} + \langle \cos^2(\psi_\omega - \psi_\Omega) \rangle - \langle \cos(\psi_\omega - \psi_\Omega) \rangle^2 - \langle \cos 2\psi_\Omega \rangle \right) (1 + \beta^2) e^{2kz} + \delta_i^2 \quad (\text{C.26})$$

The estimated velocity variance $\widetilde{\sigma}_u^2$ on each pair of electrodes in Eq. (C.26) can be rewritten as

$$\widetilde{\sigma}_u^2 \approx \frac{(1+\alpha)}{4} (1 + \beta^2) \sigma_{u0}^2 e^{2kz} + \delta_i^2 \quad (\text{C.27})$$

where $\alpha = 2\langle \cos^2 \widetilde{\psi} \rangle - 2\langle \cos \widetilde{\psi} \rangle^2 - 2\langle \cos 2\psi_\Omega \rangle$ is termed the rotational demodulation effect in this study, $\widetilde{\psi} = -(\omega - \Omega)t + \widetilde{\Phi}_0$ the difference between the surface wave angular frequency ω and the float angular rotation frequency Ω , and $\widetilde{\Phi}_0 = k_x x + k_y y + \phi_0 + \phi_i + \tan^{-1}(\beta) - \theta$.

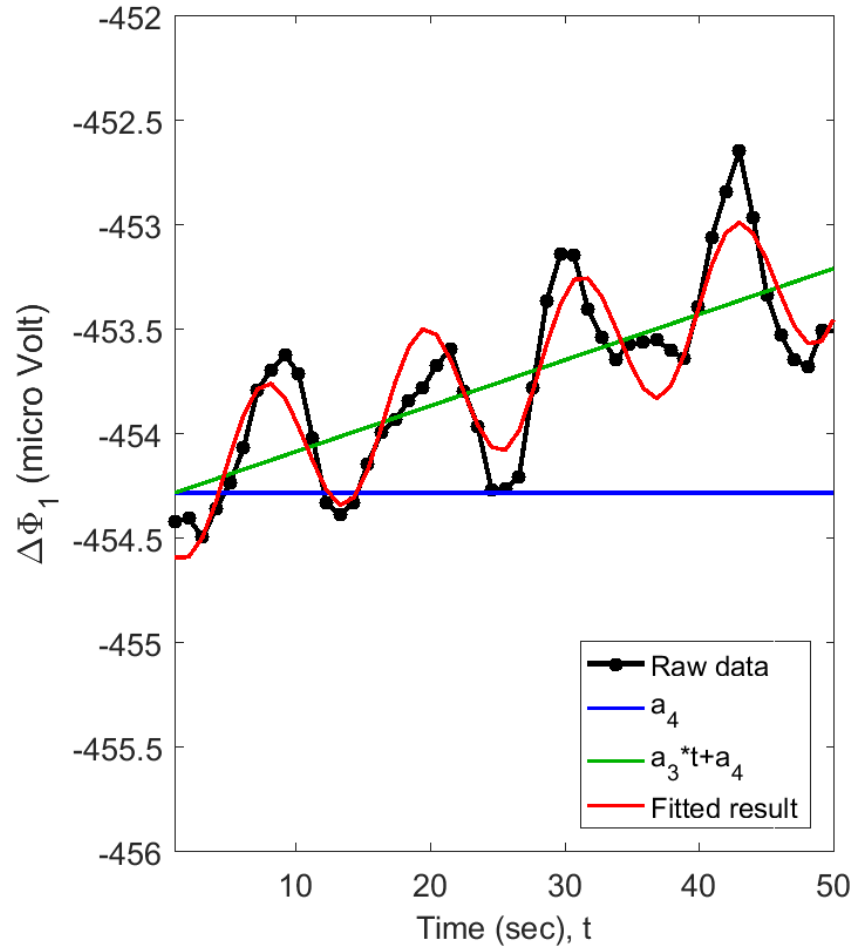


Fig. C.1. An illustration of data processing on the voltage measurements $\Delta\Phi_1$ (black line with dots) taken by the pair of electrodes E_1 on the EM-APEX floats, showing the fitted coefficient a_4 containing the component of the voltage measurement offset $\Delta\Phi_{\text{offset}}$ (blue line), the sum of voltage measurement trend a_3*t and a_4 (green line), and the result (red line) using the least-squared fitted coefficients (Eq. C.22). The residuals ϵ^i in Eq. (C.22) are the discrepancy between the voltage measurements (black line) and least-squared fitted results (red line), which are used to compute the profiles of high-frequency (> 0.02 Hz) velocity variance $\widetilde{\sigma}_u^2$ measured by the floats (Eq. C.23).

Appendix D. Surface Wave Velocity Variance Modeled by Wave Spectrum

D.1. Profiles of Surface Wave Horizontal Velocity Variance σ_u^2

According to the linear wave theory of surface waves in the deep ocean (Young 1999), the velocity of surface waves decays exponentially at the rate of k^{-1} in depth (Table 4.1), and the ratio of surface wave horizontal velocity to ocean surface displacement η equals the angular frequency ω ($=2\pi f$, where f is the surface wave frequency). We can relate the horizontal velocity spectrum S_u and the ocean surface displacement spectrum S_η as (Young 1999)

$$S_u(f, z) = \omega^2 S_\eta(f) e^{2kz} \quad (\text{D.1})$$

The dispersion relationship of surface waves in the deep ocean is $\omega^2 = gk$, where g is the gravity. Integrating the surface wave velocity spectrum S_u (Eq. D.1) at different depths, the profiles of surface wave horizontal velocity variance σ_u^2 can be computed as

$$\sigma_u^2(S_\eta, z) = \int S_u(f, z) df = \int \left(\omega^2 S_\eta(f) e^{\frac{2\omega^2 z}{g}} \right) df \quad (\text{D.2})$$

The σ_u^2 in the deep ocean can be computed using the $S_\eta(f)$, which will be implemented by the empirical surface wave spectrum reported in previous studies (Appendix D.2). Note that the variance of ocean surface displacement σ_η^2 ($= \int S_\eta df$) resulting from surface waves is proportional to the surface wave horizontal velocity variance σ_u^2 ($= \int S_u df$).

D.2. Empirical Surface Wave Model Spectrum

D.2.1. JONSWAP spectrum

The Joint North Sea Wave Project (JONSWAP) conducted a series of experiments in the 1960s to study the surface wave field in the North Atlantic Ocean (Hasselmann et al. 1973). An empirical surface wave spectrum, often termed the JONSWAP spectrum, is expressed as

$$S_{\eta} = S_p \left(\frac{f}{f_p}\right)^{-5} \exp\left(-\frac{5}{4}\left(\left(\frac{f}{f_p}\right)^{-4} - 1\right)\right) \gamma^{\exp\left(-\frac{(f-f_p)^2}{2\sigma_a^2 f_p^2}\right)-1} \quad (\text{D.3})$$

$$\begin{cases} \sigma = \sigma_a & \text{at } f \leq f_p \\ \sigma = \sigma_b & \text{at } f > f_p \end{cases}$$

where S_{η} is the one-dimensional spectrum of sea surface displacement η , f the wave frequency, S_p the peak spectrum level of S_{η} at frequency f_p (often termed peak frequency), and γ the peak enhancement factor, equal to 1 when surface waves reach their full development (Pierson and Moskowitz 1964). The parameters σ_a and σ_b define the width of the spectral peak region (Young 1999). Note that the JONSWAP spectrum is a mono-modal frequency spectrum, which concentrates energy within a narrow frequency band. The mean values of σ_a , σ_b , and γ reported by Hasselmann et al. (1973) are 0.07, 0.09, and 3.3, respectively.

D.2.2. Surface wave spectrum in Donelan et al. (1985)

Donelan et al. (1985) studied the surface wave spectra in Lake Ontario in different sea states $v=f_p|U_{10}|/g$, where g is gravity. The empirical surface wave spectrum form is expressed as

$$S_{\eta} = S_p \left(\frac{f}{f_p}\right)^{-4} \exp\left(-\left(\left(\frac{f}{f_p}\right)^{-4} - 1\right)\right) \gamma_d^{\exp\left(-\frac{(f-f_p)^2}{2\sigma_d^2 f_p^2}\right)-1} \quad (\text{D.4})$$

$$\gamma_d = \begin{cases} 6.489 + 6 \log(v) & ; \text{if } v \geq 0.159 \\ 1.7 & ; \text{if } v < 0.159 \end{cases}$$

$$\sigma_d = 0.08 + 1.29 \times 10^{-3} v^{-3}$$

where S_η is the one-dimensional spectrum of sea surface displacement η , f the wave frequency, S_p the peak spectrum level of S_η at frequency f_p (often termed peak frequency), γ_d the peak enhancement factor in the Donelan spectrum, $|\mathbf{U}_{10}|$ the wind speed at 10-m height above the sea surface, and the parameter σ_d defines the width of the spectral peak region. The high-frequency portion of the Donelan spectrum decays in f^{-4} , unlike that of the JONSWAP spectrum decaying in f^{-5} (Eq. D.3).

Appendix E. Correlation Between Parameter T and Surface Wave Estimates

The surface waves under Fanapi, Gustav, and Ike are estimated using the float profiles of high-frequency velocity variance in the upper 100 m (Chapter 4). The missing measurements in the upper 30 m under Frances and Megi may not be reliable for surface wave estimates. Within 0.3 day before the passage of tropical cyclone eyes over the floats, the f_p under the slow-moving storm Fanapi is slightly higher than that under the fast-moving storms Gustav and Ike (Table 3.1), in good agreement with Young and Vinoth (2013). The ratio of motion-forced frequency f_r (section 3.7) to peak frequency f_p is about 1.3, 2, and 2.5 under Gustav, Ike, and Fanapi (Fig. E.1), respectively. Faster storms, such as Gustav, have the value of f_r/f_p closer to 1 than slower storms, such as Fanapi (Table 3.1). The T is computed using the parametric model of fetch $\chi(r, \theta)$ in Hwang et al. (2016) as $T = \chi/U_h$ (section 3.6). The correlation coefficient between the T and f_r/f_p (Fig. E.2) is ~ 0.6 at $|\mathbf{U}_{10}| = 25\text{--}40 \text{ m s}^{-1}$. That is, about 36% of the variance of f_r/f_p can be explained by the T, and the rest of the variance may be associated with different tropical cyclone properties. Several previous studies (e.g., Young 1988; Young and Vinoth 2013) propose modeling equivalent fetch in terms of tropical cyclone properties to predict the maximum significant wave height, which cannot be used to discuss the variation of χ in each storm. Future studies are encouraged to improve the parametric model of χ by including tropical cyclone properties.

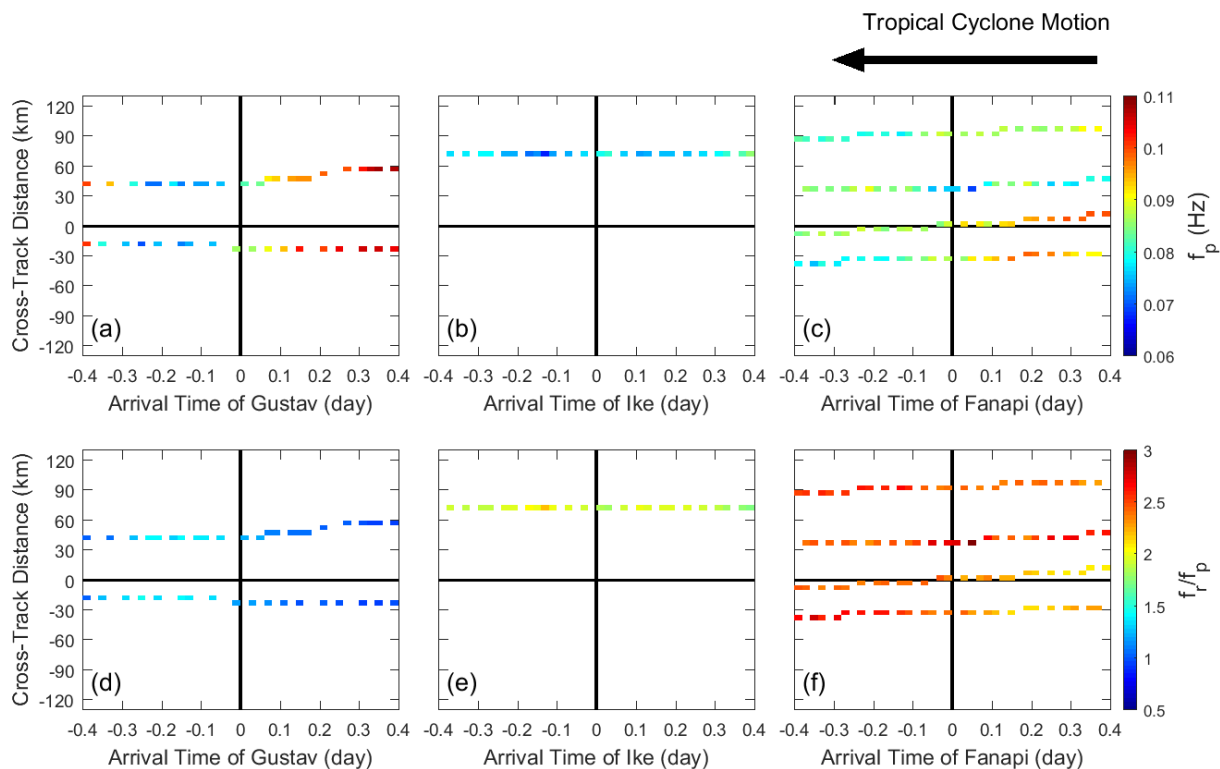


Fig. E.1. Estimates of peak frequency f_p (a–c) at the positions of EM-APEX floats (color shading), and the ratio of motion-forced frequency f_r to f_p (d–f), under Gustav (a and d), Ike (b and e), and Fanapi (c and f). The x axis is the time relative to the time tropical cyclone eyes passed the float positions. The y axis is the distance between float positions and tropical cyclone tracks.

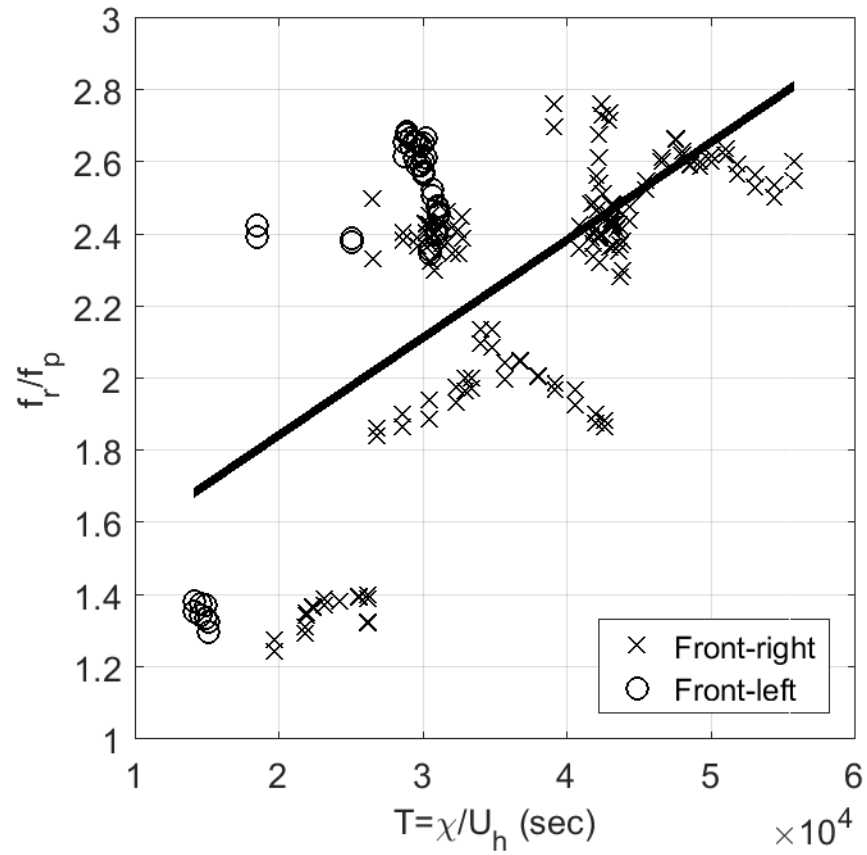


Fig. E.2. Comparison between the T parameterized by the $\chi(r,\theta)$ in Hwang et al. (2016), and the ratio of motion-forced frequency f_r to estimated peak frequency f_p in the front-right (triangles) and front-left (circles) sectors of Gustav, Ike, and Fanapi. The black line is the linear regression line between T and f_r/f_p .

Bibliography

- Anderson, R. J., 1993: A study of wind stress and heat flux over the open ocean by the inertial-dissipation method. *J. Phys. Oceanogr.*, **23**, 2153-2161.
- Balaguru, K., G. R., Foltz, L. R., Leung, E. A., D'Asaro, K. A., Emanuel, H., Liu, and S. E. Zedler, 2015: Dynamic Potential Intensity: An Improved Representation of the Ocean's Impact on Tropical Cyclones. *Geophys. Res. Lett.*, **42**, 6739-6746.
- Bell, M. M., M. T., Montgomery, and K. A. Emanuel, 2012: Air-sea enthalpy and momentum exchange at major hurricane wind speeds observed during CBLAST. *J. Atmos. Sci.*, **69**, 3197-3222.
- Black, P. G., E. A., D'Asaro, T. B., Sanford, W. M., Drennan, J. A., Zhang, J. R., French, P., Niiler, E., Terrill, and E. J. Walsh, 2007: Air-sea Exchange in hurricanes: synthesis of observations from the coupled boundary layer air-sea transfer experiment. *Bull. Amer. Meteor. Soc.*, **88**, 357-374.
- Byrne, H. M., 1983: The variation of the drag coefficient in the marine surface layer due to temporal and spatial variations of the surface wind and sea state: U.S. Dept. of Commerce, National Oceanic and Atmospheric Administration, Environmental Research Laboratories.
- Charnock, H., 1955: Wind stress on a water surface. *Q. J. Roy. Meteor. Soc.*, **81**, 639-640.
- Chen, S. S., W., Zhao, M. A., Donelan, and H. L. Tolman, 2013: Directional wind-wave coupling in fully coupled atmosphere-wave-ocean models: results from CBLAST-Hurricane. *J. Atmos. Sci.*, **70**, 3198-3215.
- Collins, C. O., III, 2014: Typhoon Generated Surface Gravity Waves Measured by NOMAD-type Buoys. Open Access Dissertations. 1286.

- Collins, C. O., III, B., Lund, R. J., Ramos, W. M., Drennan, and H. C. Graber, 2014: Wave measurement intercomparison and platform evaluation during the ITOP (2010) Experiment. *J. Atmos. Oceanic Tech.*, **31**, 2309-2329.
- Cox, C., N., Kroll, P., Pistek, and K. Watson, 1978: Electromagnetic fluctuations induced by wind waves on the deep-sea floor. *J. Geophys. Res.-Oceans*, **83**, 431-442.
- D'Asaro, E. A., P. G., Black, L. R. Centurioni, Y. T., Chang, S. S., Chen, R. C., Foster, H. C., Graber, P., Harr, V., Hormann, R. C., Lien, I. I., Lin, T. B., Sanford, T. Y., Tang, and C. C. Wu, 2014: Impact of typhoons on the ocean in the pacific. *Bull. Amer. Meteor. Soc.*, **95**, 1405-1418.
- Dietrich, J. C., J. J., Westerink, A. B., Kennedy, J. M., Smith, R. E., Jensen, M., Zijlema, L. H., Holthuijsen, C., Dawson, R. A., Luettich Jr., M. D., Powell, V. J., Cardone, A. T., Cox, G. W., Stone, H., Pourtaheri, M. E., Hope, S., Tanaka, L. G., Westerink, H. J., Westerink, and Z. Cobell, 2011: Hurricane Gustav (2008) waves and storm Surge: hindcast, synoptic analysis, and validation in Southern Louisiana. *Mon. Weather Rev.*, **139**, 2488-2522.
- Dobson, F. W., S. D., Smith, and R. J. Anderson, 1994: Measuring the relationship between wind stress and sea state in the open ocean in the presence of swell. *Atmosphere-Ocean*, **32**, 237-256.
- Donelan, M. A., J., Hamilton, and W. H. Hui, 1985: Directional spectra of wind-generated waves. *Philos. Trans. R. Soc. Lond.*, A 315, 509-562
- Donelan, M. A., A. V., Babanin, I. R., Young, and M. L. Banner, 2006: Wave-Follower Field Measurements of the Wind-Input Spectral Function. Part II: Parameterization of the Wind Input. *J. Phys. Oceanogr.*, **36**, 1672-1689.

- Donelan, M. A., M., Curcic, S. S., Chen, and A. K. Magnusson, 2012: Modeling Waves and Wind Stress. *J. Geophys. Res.-Oceans*, **117**
- Donelan, M. A., F. W., Dobson, S. D., Smith, and R. J. Anderson, 1993: On the dependence of sea surface roughness on wave development. *J. Phys. Oceanogr.*, *23*, 2143-2149.
- Donelan, M. A., W. M., Drennan, and K. B. Katsaros, 1997: The Air–Sea Momentum Flux in Conditions of Wind Sea and Swell. *J. Phys. Oceanogr.*, **27**, 2087-2099.
- Donelan, M. A., B. K., Haus, N., Reul, W. J., Plant, M., Stiassnie, H. C., Graber, O. B., Brown, and E. S. Saltzman, 2004: On the limiting aerodynamic roughness of the ocean in very strong winds. *Geophys. Res. Lett.*, **31**, doi: 10.1029/2004GL019460
- Drennan, W., and Shay, L., 2006: On the variability of the fluxes of momentum and sensible heat. *Bound.-Lay. Meteorol.*, **119**, 81-107.
- Drennan, W. M., H. C., Graber, and M. A. Donelan, 1999: Evidence for the effects of swell and unsteady winds on marine wind stress. *J. Phys. Oceanogr.*, **29**, 1853-1864.
- Drennan, W. M., H. C., Graber, D., Hauser, and C. Quentin, 2003: On the wave age dependence of wind stress over pure wind seas. *J. Geophys. Res.-Oceans*, **108**, 8062. doi: 10.1029/2000JC000715
- Dyer, A. J., 1974: A review of flux-profile relationships. *Bound.-Lay. Meteorol.*, **7**, 363-372. doi: 10.1007/BF00240838
- Edson, J. B., V., Jampana, R. A., Weller, S. P., Bigorre, A. J., Plueddemann, C. W., Fairall, S. D., Miller, L., Mahrt, D., Vickers, and H. Hersbach, 2013: On the exchange of momentum over the open ocean. *J. Phys. Oceanogr.*, **43**, 1589-1610.
- Emanuel, K. A., 1986. An air-sea interaction theory for tropical cyclones. part I: steady-state maintenance. *J. Atmos. Sci.*, **43**, 585-605.

- Emanuel, K. A., 1995: Sensitivity of tropical cyclones to surface exchange coefficients and a revised steady-state model incorporating eye dynamics. *J. Atmos. Sci.*, **52**, 3969-3976.
- Fan, Y., I., Ginis, T., Hara, C. W., Wright, and E. J. Walsh, 2009: Numerical simulations and observations of surface wave fields under an extreme tropical cyclone. *J. Phys. Oceanogr.*, **39**, 2097-2116.
- Fan, Y., and Rogers, W. E., 2016: Drag coefficient comparisons between observed and model simulated directional wave spectra under hurricane conditions. *Ocean Model.*, **102**, 1-13.
doi: <https://doi.org/10.1016/j.ocemod.2016.04.004>
- Fontaine, E., 2013: A Theoretical Explanation of the Fetch- and Duration-Limited Laws. *J. Phys. Oceanogr.*, **43**, 233-47.
- García-Nava, H., Ocampo-Torres, F. J., Osuna, P., and Donelan, M. A., 2009: Wind stress in the presence of swell under moderate to strong wind conditions. *J. Geophys. Res.-Oceans*, **114**.
doi: 10.1029/2009JC005389
- Geernaert, G. L., 1988: Measurements of the angle between the wind vector and wind stress vector in the surface layer over the North Sea. *J. Geophys. Res.-Oceans*, **93**, 8215-8220.
- Geernaert, G. L., F., Hansen, M., Courtney, and T. Herbers, 1993: Directional attributes of the ocean surface wind stress vector. *J. Geophys. Res.-Oceans*, **98**, 16571-16582.
- Geernaert, G. L., K. B., Katsaros, and K. Richter, 1986: Variation of the drag coefficient and its dependence on sea state. *J. Geophys. Res.-Oceans*, **91**, 7667-7679.
- Gill, A. E., 1984: On the behavior of internal waves in the wakes of storms. *J. Phys. Oceanogr.*, **14**, 1129-1151.

- Graber, H. C., E. A., Terray, M. A., Donelan, W. M., Drennan, J. C. V., Leer, and D. B. Peters, 2000: ASIS—a new air–sea interaction spar buoy: design and performance at sea. *J. Atmos. Oceanic Tech.*, **17**, 708-720. doi: 10.1175/1520-0426(2000)017<0708:aanasi>2.0.co;2
- Grachev, A. A., and Fairall, C. W., 2001: Upward momentum transfer in the marine boundary layer. *J. Phys. Oceanogr.*, **31**, 1698-1711.
- Grachev, A. A., C. W., Fairall, J. E., Hare, J. B., Edson, and S. D. Miller, 2003: Wind stress vector over ocean waves. *J. Phys. Oceanogr.*, **33**, 2408-2429.
- Grare, L., L., Lenain, and W. K. Melville, 2013: Wave-Coherent Airflow and Critical Layers over Ocean Waves. *J. Phys. Oceanogr.*, **43**, 2156-2172
- Hasselmann, K., T. P., Barnett, E., Bouws, H., Carlson, D. E., Cartwright, K., Enke, J.A., Ewing, H., Gienapp, D. E., Hasselmann, P., Kruseman, A., Meerburg, P., Miller, D. J., Olbers, K., Richter, W., Sell, and H. Walden, 1973: Measurements of wind-wave growth and swell decay during the Joint North Sea Wave Project (JONSWAP). In: *Ergänzungsheft zur Deutschen Hydrographischen Zeitschrift Reihe*, Deutsches Hydrographisches Institute, Hamburg, Germany, p. 95
- Hasselmann, K., W., Sell, D. B., Ross, and P. Müller, 1976: A parametric wave prediction model. *J. Phys. Oceanogr.*, **6**, 200-228.
- Hasselmann, S., K., Hasselmann, J. H., Allender, and T. P. Barnett, 1985: Computations and parameterizations of the nonlinear energy transfer in a gravity-wave spectrum. Part II: parameterizations of the nonlinear energy transfer for application in wave models. *J. Phys. Oceanogr.*, **15**, 1378-1391.

- Herbers, T. H. C., P. F., Jessen, T. T., Janssen, D. B., Colbert, and J. H. MacMahan, 2012: Observing ocean surface waves with GPS-tracked buoys. *J. Atmos. Oceanic Tech.*, **29**, 944-959. doi: 10.1175/JTECH-D-11-00128.1
- Holthuijsen, L. H., M. D., Powell, and J. D. Pietrzak, 2012: Wind and waves in extreme hurricanes. *J. Geophys. Res.-Oceans*, **117**, C09003. doi: 10.1029/2012JC007983
- Hsu, J.-Y., R.-C., Lien, E., D'Asaro, and T. B. Sanford, 2017: Estimates of surface wind stress and drag coefficients in Typhoon Megi 2010. *J. Phys. Oceanogr.*
- Hu, K., and Chen, Q., 2011: Directional spectra of hurricane-generated waves in the Gulf of Mexico. *Geophys. Res. Lett.*, **38**. doi: 10.1029/2011GL049145
- Hwang, P. A., D. W., Wang, E. J., Walsh, W. B., Krabill, and R. N. Swift, 2000: Airborne measurements of the wavenumber spectra of ocean surface waves. part I: spectral slope and dimensionless spectral coefficient. *J. Phys. Oceanogr.*, **30**, 2753-2767. doi: 10.1175/1520-0485(2001)031<2753:amotws>2.0.co;2
- Hwang, P. A., X., Li, B., Zhang, and E. Walsh, 2016: Fetch-limited surface wave growth inside tropical cyclones and hurricane wind speed retrieval. Geoscience and Remote Sensing Symposium (IGARSS). IEEE International
- Hwang, P. A., Y. Fan, F. J. Ocampo-Torres, and H. García-Nava, 2017: Ocean Surface Wave Spectra inside Tropical Cyclones. *J. Phys. Oceanogr.*, **47**, 2393-417.
- Jan, S., Y. J., Yang, H.-I. Chang, M.-H. Chang, and C.-L. Wei, 2017: New data buoys watch typhoons from within the storm, *EOS*, **98**, <https://doi.org/10.1029/2017EO069821>.
- Janssen, J. A. M., 1997: Does wind stress depend on sea-state or not? a statistical error analysis of Hexmax Data. *Bound.-Lay. Meteorol.*, **83**, 479-503.

- Jarosz, E., D. A., Mitchell, D. W., Wang, and W. J. Teague, 2007: Bottom-up determination of air-sea momentum exchange under a major tropical cyclone. *Science*, **315**, 1707-1709.
- Johnson, H. K., J., Højstrup, H. J., Vested, and S. E. Larsen, 1998: On the dependence of sea surface roughness on wind waves. *J. Phys. Oceanogr.*, **28**, 1702-1716.
- Jones, I. S. F. and Toba, Y., 2012: Wind stress over the ocean. *Cambridge University Press*
- Ko, D. S., S.-Y., Chao, C.-C., Wu, and I. I. Lin, 2014: Impacts of Typhoon Megi (2010) on the South China Sea. *J. Geophys. Res.-Oceans*, **119**, 4474-4489.
- Kuik, A. J., G. P. V., Vledder, and L. H. Holthuijsen, 1988: A method for the routine analysis of pitch-and-roll buoy wave data. *J. Phys. Oceanogr.*, **18**, 1020-1034. doi: 10.1175/1520-0485(1988)018<1020:amftra>2.0.co;2
- Large, W. G., and Pond, S., 1981: Open ocean momentum flux measurements in moderate to strong winds. *J. Phys. Oceanogr.*, **11**, 324-336.
- Lin, W., L. P., Sanford, and S. E. Suttles, 2002: Wave measurement and modeling in Chesapeake Bay. *Cont. Shelf Res.*, **22**, 2673-2686. doi: [http://dx.doi.org/10.1016/S0278-4343\(02\)00120-6](http://dx.doi.org/10.1016/S0278-4343(02)00120-6)
- Lin, I. I., P., Black, J. F., Price, C.-Y., Yang, S. S., Chen, C.-C., Lien, P., Harr, N.-H., Chi, C.-C., Wu, and E. A. D'Asaro, 2013: An ocean coupling potential intensity index for tropical cyclones. *Geophys. Res. Lett.*, **40**, 1878-1882.
- Lewis, A. W., and R. N. Allos, 1990: JONSWAP's parameters: sorting out the inconsistencies. *Ocean Eng.*, **17**, 409-415.
- Lilley, F. E. M., A. P., Hitchman, P. R., Milligan, and T. Pedersen, 2004: Sea-surface observations of the magnetic signals of ocean swells. *Geophys. J. Int.*, **159**, 565-572.

- Longuet-Higgins, M. S., M. E., Stern, and H. Stommel., 1954: The electrical field induced by ocean currents and waves, With applications to the method of towed electrode. Papers in Physical Oceanography and Meteorology, **13**, 1-37.
- Magnusson, A. K., and Donelan, M. A., 2013: The Andrea wave characteristics of a measured North Sea rogue wave. *J. Offshore Mech. and Arctic Eng.*, **135**, 031108-031108-031110. doi: 10.1115/1.4023800
- Miles, J. W., 1960: On the generation of surface waves by turbulent shear flows. *J. Fluid Mech.*, **7**, 469-478.
- Mitsuyasu, H., F., Tasai, T., Suhara, S., Mizuno, M., Ohkusu, T., Honda, and K. Rikiishi, 1975: Observations of the directional spectrum of ocean waves using a cloverleaf buoy. *J. Phys. Oceanogr.*, **5**, 750-760. doi: 10.1175/1520-0485(1975)005<0750:oootdso>2.0.co;2
- Mitsuyasu, H., F., Tasai, T., Suhara, S., Mizuno, M., Ohkusu, T., Honda, and K. Rikiishi, 1980: Observation of the power spectrum of ocean waves using a cloverleaf Buoy. *J. Phys. Oceanogr.*, **10**, 286-296.
- Moon, I.-J., I., Ginis, and T. Hara, 2004: Effect of surface waves on air–sea momentum exchange. part II: behavior of drag coefficient under tropical cyclones. *J. Atmos. Sci.*, **61**, 2334-2348.
- Mrvaljevic, R. K., P. G., Black, L. R., Centurioni, Y.-T., Chang, E. A., D'Asaro, S. R., Jayne, C. M., Lee, R.-C., Lien, I. I., Lin, M. Jan, P. P., Niiler, L., Rainville, and T. B., Sanford, 2013: Observations of the Cold Wake of Typhoon Fanapi (2010). *Geophys. Res. Lett.*, **40**, 316-21.
- NOAA NWS, 1979: Meteorological criteria for standard project hurricane and probable maximum hurricane wind fields, Gulf of Mexico and east coast of the United States. NOAA Tech. Rep. **NWS 23**, U.S. Department of Commerce, Washington D.C., 320 pp.

- Ochi, M. K., 2003: Hurricane-generated seas. *Elsevier*, **8**.
- Ochi, M. K., and Chiu, M.-H., 1982: Nearshore wave spectra measured during Hurricane David. *Coast. Eng. Proc.* doi: 10.9753
- Phillips, O. M., 1957: On the generation of waves by turbulent wind. *J. Fluid Mech.*, **2**, 417-445.
- Pierson, W. J., and Moskowitz L., 1964: A proposed spectral form for fully developed wind seas based on the similarity theory of S. A. Kitaigorodskii. *J. Geophys. Res.*, **69**, 5181-5190. doi: 10.1029/JZ069i024p05181
- Pinkel, R., and Smith, J. A., 1987: Open ocean surface wave measurement using Doppler sonar. *J. Geophys. Res.-Oceans*, **92**, 12967-12973. doi: 10.1029/JC092iC12p12967
- Podney, W., 1975: Electromagnetic fields generated by ocean waves. *J. Geophys. Res.*, **80**, 2977-2990.
- Potter, H., C. O., Collins, W. M., Drennan, and H. C. Graber, 2015: Observations of wind stress direction during Typhoon Chaba (2010). *Geophys. Res. Lett.*, doi: 10.1002/2015GL065173
- Powell, M. D., P. J., Vickery, and T. A. Reinhold, 2003: Reduced drag coefficient for high wind speeds in tropical cyclones. *Nature*, **422**, 279-283. doi: Doi 10.1038/Nature01481
- Price, J. F., T. B., Sanford, and G. Z. Forristall, 1994: Forced stage response to a moving hurricane. *J. Phys. Oceanogr.*, **24**, 233-260.
- Price, J. F., R. A., Weller, and R. Pinkel, 1986: Diurnal cycling: Observations and models of the upper ocean response to diurnal heating, cooling, and wind mixing. *J. Geophys. Res.-Oceans*, **91**, 8411-8427.
- Rabe, T. J., T., Kukulka, I., Ginis, T., Hara, B. G., Reichl, E. A., D'Asaro, R. H., Ramsey, and P. P. Sullivan, 2015: Langmuir Turbulence under Hurricane Gustav (2008). *J. Phys. Oceanogr.*, **45**, 657-677.

- Reichert, K., K., Hessner, J. C., Nieto Borge, and J. Dittmer, 1999: WaMoS II: A Radar Based Wave And Current Monitoring System. *International Offshore and Polar Engineering Conference*.
- Reichl, B. G., T., Hara, and I. Ginis, 2014: Sea state dependence of the wind stress over the ocean under hurricane winds. *J. Geophys. Res.-Oceans*, **119**, 30-51.
- Rieder, K. F., Smith, J. A., and Weller, R. A., 1994: Observed directional characteristics of the wind, wind stress, and surface waves on the open ocean. *J. Geophys. Res.-Oceans*, **99**, 22589-22596.
- Roy, T., 1994: Bootstrap accuracy for non-linear regression models. *J. Chemometrics*, **8**, 37-44.
doi: 10.1002/cem.1180080105
- Sanford, T. B., 1971: Motionally induced electric and magnetic fields in the sea. *J. Geophys. Res.*, **76**, 3476-3492.
- Sanford, T. B., R. G., Drever, and J. H. Dunlap, 1978: A velocity profiler based on the principles of geomagnetic induction. *Deep-Sea Res.*, **25**, 183-210.
- Sanford, T. B., J. H., Dunlap, J. A., Carlson, D. C., Webb, and J. B. Girton, 2005, 28-29 June 2005: Autonomous velocity and density profiler: EM-APEX. Paper presented at the Current Measurement Technology, 2005. Proceedings of the IEEE/OES Eighth Working Conference on.
- Sanford, T. B., J. F., Price, and J. B. Girton, 2011: Upper-ocean response to Hurricane Frances (2004) observed by profiling EM-APEX floats*. *J. Phys. Oceanogr.*, **41**, 1041-1056.
- Smith, S. D., 1980: Wind stress and heat flux over the ocean in gale force winds. *J. Phys. Oceanogr.*, **10**, 709-726.

- Smith, S., R., Anderson, W., Oost, C., Kraan, N., Maat, J., De Cosmo, K. B., Katsaros, K. L., Davidson, K., Bumke, and H. M. Chadwick, 1992: Sea surface wind stress and drag coefficients: The hexos results. *Bound.-Lay. Meteorol.*, **60**, 109-142.
- Sullivan, P. P., L., Romero, J. C., McWilliams, and W. K. Melville, 2012: Transient evolution of Langmuir turbulence in ocean boundary layers driven by hurricane winds and waves. *J. Phys. Oceanogr.*, **42**, 1959-80.
- Takagaki, N., S. Komori, N. Suzuki, K. Iwano, T. Kuramoto, S. Shimada, R. Kurose, and K. Takahashi, 2012: Strong correlation between the drag coefficient and the shape of the wind sea spectrum over a broad range of wind speeds. *Geophys. Res. Lett.*, 39, doi: 10.1029/2012GL053988
- Taylor, P. K., and Yelland, M. J., 2001: The dependence of sea surface roughness on the height and steepness of the waves. *J. Phys. Oceanogr.*, **31**, 572-590.
- Thébaud, E., C. C., Finlay, C. D., Beggan, P., Alken, J., Aubert, O., Barrois, F., Bertrand, T., Bondar, A., Boness, L., Brocco, E., Canet, A., Chambodut, A., Chulliat, P., Coïsson, F., Civet, A., Du, A., Fournier, I., Fratter, N., Gillet, B., Hamilton, M., Hamoudi, G., Hulot, T., Jager, M., Korte, W., Kuang, X., Lalanne, B., Langlais, J.-M., Léger, V., Lesur, F., and J. Lowes, 2015: International geomagnetic reference field: the 12th generation. *Earth Planets Space*, 67:79
- Tolman, H. L., and D. Chalikov, 1996: Source Terms in a Third-Generation Wind Wave Model. *J. Phys. Oceanogr.*, **26**, 2497-2518. doi: doi:10.1175/1520-0485(1996)026<2497:STIATG>2.0.CO;2

- UCAR/NCAR, 2016: Earth Observing Laboratory, 1993-present. NCAR Airborne Vertical Atmospheric Profiling System (AVAPS). <http://dx.doi.org/10.5065/D66W9848>, https://www.eol.ucar.edu/observing_facilities/avaps-dropsonde-system
- Uhlhorn, E. W., and Black, P. G., 2003: Verification of remotely sensed sea surface winds in Hurricanes. *J. Atmos. Ocean Tech.*, **20**, 99-116.
- Walsh, E. J., C. W., Wright, D., Vandemark, W. B., Krabill, A. W., Garcia, S. H., Houston, S. T., Murillo, M. D., Powell, P., Black., and F. D. Marks Jr., 2002: Hurricane Directional Wave Spectrum Spatial Variation at Landfall. *J. Phys. Oceanogr.*, **32**, 1667-1684.
- Wang, H., and Wang, Y., 2014: A numerical study of Typhoon Megi (2010: Part I: Rapid Intensification. *Mon. Weather Rev.*, **142**, 29-48.
- Watermann, J., and Magunia, A., 1997: Propagation Parameters of Sea Surface Waves Inferred from Observations from Two Closely Spaced Vector Magnetometers. *J. Geomagn. and Geoelectr.*, **49**, 709-720.
- The WAVEWATCH III Development Group, 2016: User manual and system documentation of WAVEWATCH III version 5.16. Tech. Note 329, NOAA/NWS/NCEP/MMAB, College Park, MD, USA, 326 pp.+ Appendices.
- Weaver, J. T., 1965: Magnetic variations associated with ocean waves and swell. *J. Geophys. Res.*, **70**, 1921-1929.
- Wright, C. W., E. J., Walsh, D., Vandemark, W. B., Krabill, A. W., Garcia, S. H., Houston, M. D., Powell, P. G., Black, and F. D. Marks, 2001: Hurricane directional wave spectrum spatial variation in the open ocean. *J. Phys. Oceanogr.*, **31**, 2472-2488.
- Wu, C.-C., P.-H., Lin, S., Abernethy, T.-C., Yeh, W.-P., Huang, K.-H., Chou, J.-S., Hong, G.-C., Lu, C.-T., Fong, K.-C., Hsu, I. I., Lin, P.-L., Lin, and C.-H. Liu, 2005: Dropwindsonde

- observations for typhoon surveillance near the Taiwan region (DOTSTAR): An Overview. *Bull. Amer. Meteor. Soc.*, **86**, 787-790.
- Yelland, M., and Taylor, P. K., 1996: Wind stress measurements from the open ocean. *J. Phys. Oceanogr.*, **26**, 541-558.
- Young I. R., 1988: A shallow water spectral wave model. *J. Geophys. Res.* **93**. 5113–29
- Young, I. R. and Burchell, G. P., 1996: Hurricane Generated Waves as Observed by Satellite, *Ocean Eng.*, **23**, 8, 761-776.
- Young, I. R., 1998: Observations of the spectra of hurricane generated waves. *Ocean Eng.*, **25**, 261-276.
- Young, I. R., 1999: Wind generated ocean waves. *Elsevier*, **2**, 12-160
- Young, I. R., 2003: A review of the sea state generated by hurricanes. *Marine Structures*, **16**, 201-218.
- Young, I. R., 2006: Directional spectra of hurricane wind waves. *J. Geophys. Res.-Oceans*, **111**.
doi: 10.1029/2006JC003540
- Young, I.R. and Vinoth, J., 2013: An 'extended fetch' model for the spatial distribution of tropical cyclone wind-waves as observed by altimeter, *Ocean Eng.*, **70**, 14-24, doi: 10.1016/j.oceaneng.2013.05.015.
- Zhang, F. W., W. M., Drennan, B. K., Haus, and H. C. Graber, 2009: On wind-wave-current interactions during the Shoaling Waves Experiment. *J. Geophys. Res.-Oceans*, **114**, C01018. doi: 10.1029/2008JC004998
- Zhang, J. A., and Uhlhorn, E. W., 2012: Hurricane sea surface inflow angle and an observation-based parametric model. *Mon. Weather Rev.*, **140**, 3587-3605.

Zhao, Z., 2014: Internal tide radiation from the Luzon Strait. *J. Geophys. Res.-Oceans*. doi:

10.1002/2014JC010014

Curriculum Vitae

Je-Yuan, Hsu

Email: jyhsu@uw.edu

Education/Training:

2011.09~2017.12: *Master and Ph.D., University of Washington, Seattle, USA*

- The graduate school of Oceanography
- Advised by Dr. Ren-Chieh Lien and Dr. Eric D'Asaro
- Work on Impact of Typhoons on the Ocean in the Pacific (ITOP) project
- Studies on tropical cyclone-wave-ocean interactions
- Estimate drag coefficients and surface waves using EM-APEX float measurements
- Use ocean response model PWP3D and wave model WAVEWATCH III for research

2006.09~2010.06: *Bachelor, National Taiwan University, Taipei, Taiwan*

- The department of Atmospheric Science
- Advised by Dr. I-I Lin
- Research on the remote-sensing of typhoon-induced ocean response

Work History:

2011.09~2017.12: *Research Assistant in University of Washington*

- The research assistant in Applied Physics Laboratory (APL-UW)

2012.09~2012.12: *Teaching Assistant in University of Washington (UW)*

- Help Prof. Quay in UW for the course of Ocean Circulation.

2010.07~2011.08: *Research Assistant in National Taiwan University*

- The research assistant in Synergy of Multi-Advanced Remote Sensing For Atmosphere-Ocean Interaction (SMART) Laboratory

Talk, Conference and Workshop:

2017.01.22-26: *AMS 97th annual meeting, Seattle, USA*

- Poster presentation of spatial variability of drag coefficients under five tropical cyclones

2016.11.28: *Talk in Taiwan Ocean Research Institute, Kaohsiung, Taiwan*

- Oral presentation of EM-APEX floats measurements under tropical cyclones

2016.02.21-26: *Ocean Science Meeting, New Orleans, USA*

- Poster presentation of surface waves under Typhon Fanapi 2010

2015.01.20: *Talk in National Sun Yat-Sen University, Kaohsiung, Taiwan*

- Oral presentation of drag coefficient under Typhon Megi 2010

2015.01.12: *Talk in National Taiwan University, Taipei, Taiwan*

- Oral presentation of drag coefficient under Typhon Megi 2010

2014.02.23~28: *Ocean Science Meeting in Honolulu, USA*

- Poster presentation of drag coefficients under Typhoon Megi in air-sea interaction section

2012.12.03~07: *AGU fall meeting in San Francisco, USA*

- Poster presentation of downwind drag coefficient under Typhoon Megi in tropical cyclone section

2012.03.26~28: *ITOP workshop in Kaohsiung, Taiwan*

- Discuss the research problems and present the scientific results in ITOP project.

Publication:

Ali, M. M., P. S. V. Jagadeesh, I. I. Lin, and J.-Y. Hsu, 2012. A Neural Network Approach to Estimate Tropical Cyclone Heat Potential in the Indian Ocean. *Geoscience and Remote Sensing Letters*, IEEE 9, 6: 1114-17.

Hsu, J.-Y., R.-C., Lien, E. A., D'Asaro, and T. B., Sanford, 2017. Estimates of Surface Wind Stress and Drag Coefficients in Typhoon Megi 2010. *J. Phys. Oceanogr.*

Hsu, J.-Y., R.-C., Lien, E. A., D'Asaro, and T. B., Sanford, 2017. Estimates of Surface Waves Using Subsurface EM-APEX Floats under Typhoon Fanapi 2010. *J. Atmos. Oceanic Tech.*